E.ON Energy Research Center

RWTH AACHEN UNIVERSITY

Advanced Harmonic Stability Monitoring and Control of Power-Electronics Dominated Grids

Sriram Karthik Gurumurthy
Institute for Automation of Complex Power Systems

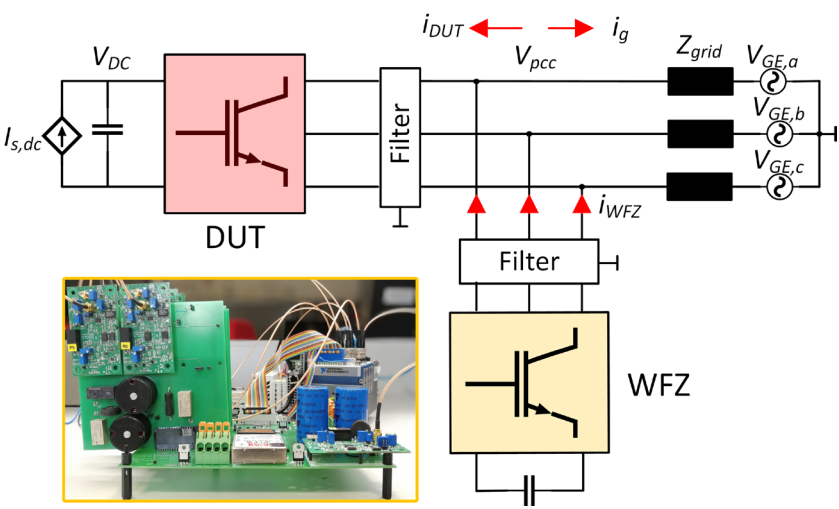

Advanced Harmonic Stability Monitoring and Control of Power-Electronics Dominated Grids

Von der Fakultät für Elektrotechnik und Informationstechnik
der Rheinisch-Westfälischen Technischen Hochschule Aachen
zur Erlangung des akademischen Grades eines Doktors
der Ingenieurwissenschaften genehmigte Dissertation

vorgelegt von

Sriram Karthik Gurumurthy, M. Sc.

aus
Thanjavur, Indien

Berichter:
Univ.-Prof. Antonello Monti, Ph. D.
Prof. Dr.-Ing. Marco Liserre, Ph. D.

Tag der mündlichen Prüfung: 2. September 2024

Bibliographische Information der Deutschen Nationalbibliothek
Die Deutsche Nationalbibliothek verzeichnet diese Publikation in der Deutschen Nationalbibliografie; detaillierte bibliografische Daten sind im Internet über https://dnb.dnb.de abrufbar.

D 82 (Diss. RWTH Aachen University, 2024)

Herausgeber:
E.ON Energy Research Center

Institute for Automation of Complex Power Systems (ACS)
E.ON Energy Research Center
Mathieustraße 10
52074 Aachen

E.ON Energy Research Center I 141. Ausgabe der Serie
ACS I Automation of Complex Power Systems

Printed in Germany

ISBN: 978-3-948234-55-3
1. Auflage 2025

Verlag:
E.ON Energy Research Center, RWTH Aachen University
Mathieustraße 10
52074 Aachen
Internet: www.eonerc.rwth-aachen.de
E-Mail: post_erc@eonerc.rwth-aachen.de

Herstellung:
Druckservice Zillekens
Rainweg 19
52224 Stolberg
Mail: info@druckservice-zillekens.de

Kurzfassung

Motivation, Ziel und Aufgabenstellung der Arbeit

Mit der zunehmenden Verbreitung erneuerbarer Energiequellen (EE), die durch die groß angelegte Integration von netzgekoppelten leistungselektronischen Umrichtern ermöglicht wird, ist ein neues Paradigma entstanden. Diese leistungselektronischen Netze (PEDGs) stellen neue Herausforderungen an die Stabilität über einen breiten Frequenzbereich dar. Die Wechselwirkung zwischen den leistungselektronischen Quellen und den nichtlinearen Lasten kann zu unerwünschten Oberschwingungen und Zwischenharmonischen führen, die die Netzspannung verzerren und die Netzqualität beeinträchtigen. Je nach den Betriebsbedingungen und der Dämpfung im Stromnetz können diese Zwischenharmonischen aufrechterhalten werden und in Resonanz treten; der Oberwellengehalt kann über einen bestimmten Zeitraum zunehmen, das Auslösen von Unterbrechern verursachen und das Netz möglicherweise vollständig destabilisieren. Dieses Phänomen wird als *harmonische Instabilität* bezeichnet.

Angesichts der zunehmenden Zahl von Fällen und Ausfällen, mit denen Netzbetreiber konfrontiert werden, ist es unerlässlich, Methoden zur Überwachung und Erkennung von Oberschwingungsstabilitätsbedingungen zu entwickeln. In den letzten zehn Jahren wurde in mehreren Forschungsstudien festgestellt, dass die harmonische Stabilität als Impedanzphänomen charakterisiert werden kann und daher die Impedanz von Umrichtern benötigt wird. Die Hersteller von Umrichtern schützen die Hardware und die Steuersysteme von Umrichtern durch geistige Eigentumsrechte (IPR), so dass Black-Box- oder nichtparametrische Modelle von Umrichtern erforderlich sind. Folglich ist die Wahl der Messmethode für die schnelle Impedanzextraktion von entscheidender Bedeutung, ebenso wie die Charakterisierung solcher Messgeräte. Die Aggregation der extrahierten Impedanzdaten auf Systemebene ist für Studien zur

harmonischen Stabilität auf Systemebene von entscheidender Bedeutung. Um Probleme mit der Oberschwingungsstabilität anzugehen, sind lokale Kompensationsverfahren erforderlich, um die Impedanz von Stromrichtern anzupassen und die gewünschte Dämpfung effektiv einzuführen. Ziel dieser Dissertation ist die Entwicklung eines eigenständigen Impedanzmessgeräts, eines Algorithmus zur Überwachung der Oberschwingungsstabilität in einem Multi-Bus-Netz und eines Verfahrens zur Minderung der harmonischen Instabilität.

Wesentliche Wissenschaftliche Beiträge der Arbeitt

In dieser Dissertation werden vier wichtige wissenschaftliche Beiträge vorgeschlagen, die eine Überwachung der harmonischen Stabilität und einen sicheren Betrieb von PEDGs ermöglichen: 1) ein eigenständiges Impedanzmessgerät, um die Netzimpedanz auf nicht-parametrische Weise zu extrahieren; 2) eine Frequenzkopplungsmatrix (FCM) Messmethode für Stromrichter; 3) eine nicht-parametrische Methode zur Überwachung der harmonischen Stabilität von Mehrbussystemen; und 4) eine fortschrittliche virtuelle Dämpfungssteuerungsstrategie für netzgekoppelte leistungselektronische Umrichter.

Der erste Teil der Arbeit befasst sich mit der Messung von nicht-parametrischen Impedanzen. Für die Messung von Netzimpedanzen wird ein eigenständiges, steckerfertiges Messgerät namens Breitband-Frequenz-Netzimpedanz-Messgerät (WFZ) entwickelt. Ein Low-Power-Prototyp des vorgeschlagenen Geräts wurde gebaut. Die lineare Impedanzmessung wird zunächst durch Simulationen und anschließend durch experimentelle Messungen verifiziert. Zur Validierung des WFZ-Geräts wird eine Charakterisierung der Messunsicherheit durchgeführt.

Der zweite Teil dieser Arbeit berücksichtigt die Nichtlinearität durch die FCM und erweitert den Messalgorithmus des WFZ-Bauelements, um FCM-Messungen zu ermöglichen. Es werden Charakterisierungsparameter für die Analyse und Interpretation der extrahierten FCM entwickelt. Es wurden simulative und experimentelle Messungen durchgeführt, um die FCM eines netzgekoppelten Umrichters zu extrahieren, gefolgt von einer Validierung der extrahierten FCM.

Im dritten Teil der Arbeit wird eine nicht-parametrische Methode zur Überwachung der harmonischen Stabilität vorgeschlagen.

Die vorgeschlagene Methode erfordert nicht-parametrische Impedanzmessungen der aktiven Komponenten im Netz. Es wird ein Bus-Admittanz-Matrix-Ansatz in Betracht gezogen, um die nichtparametrischen Impedanzen der Stromrichter innerhalb des Netzes zu aggregieren. Die vorgeschlagene Methode ermöglicht die Berechnung der minimalen Phasenspanne und der kritischen Frequenz, bei der eine Dämpfung erforderlich ist. Die Wirksamkeit der Methode wird empirisch durch Validierung an sternförmigen und vermaschten Stromnetzen demonstriert, wodurch ihre breite Anwendbarkeit in verschiedenen Netzkonfigurationen deutlich wird.

Im letzten Teil der Arbeit wird ein nicht-parametrischer Ansatz zur Minderung der harmonischen Instabilität vorgeschlagen. Die vorgeschlagene Methode besteht aus einem zentralen nicht-parametrischen Stabilitätsüberwachungswerkzeug, das die kritische Frequenz und Bandbreite identifiziert, die dann an die lokalen Wandler weitergegeben werden. Die Wandler implementieren die Dämpfung durch den vorgeschlagenen adaptiven virtuellen Dämpfungsregler, der als digitaler Filter mit unendlicher Impulsantwort (IIR) mit adaptiven Parametern wie der kritischen Frequenz und Bandbreite implementiert ist; darüber hinaus wird ein auf einer Nachschlagetabelle basierender Ansatz vorgeschlagen, um die optimale Verstärkung des VDC auf der Grundlage der kritischen Frequenz und Bandbreite auszuwählen. Der vorgeschlagene VDC-Regler benötigt nur eine Netzstrommessung, wodurch eine Regelungsstruktur mit zwei Freiheitsgraden (2-DoF) entsteht. Die Wirksamkeit des vorgeschlagenen Ansatzes wurde durch experimentelle Validierungen nachgewiesen.

Diese Arbeit leistet einen wichtigen Beitrag auf dem Gebiet der Impedanzmessgeräte, der Überwachung der Oberschwingungsstabilität auf Systemebene und der Entwicklung eines fortschrittlichen VDC, was zu Fortschritten auf diesen Gebieten führt.

Abstract

Motivation, Goal and Task of the Dissertation

A new paradigm has emerged with the increased proliferation of renewable energy sources (RES), which is enabled by the large-scale integration of grid-connected power electronic converters. These power electronic-dominated grids (PEDGs) pose new challenges to stability over a wide range of frequencies. Interaction among the power electronic-interfaced sources and non-linear loads may lead to the presence of undesirable harmonics and inter-harmonics, which distort the grid voltage and affect power quality. Depending on the operating conditions and damping in the power system, these inter-harmonics could remain sustained and resonate; the harmonic content may increase over a period, cause tripping of breakers, and potentially fully destabilize the grid. This phenomenon is known as *harmonic instability*.

Due to the growing number of instances and failures experienced by grid operators, it is essential to develop methods to monitor and detect harmonic stability conditions. Over the last decade, several research studies have identified that harmonic stability can be characterized as an impedance phenomenon, and thus the impedance of converters would be required. Converter manufacturers protect the hardware and control systems of converters through Intellectual Property Rights (IPR), and thus black-box or non-parametric models of converters are required. Consequently, the choice of measurement method for rapid impedance extraction becomes vital, as does the characterization of such measurement devices. Aggregation of the extracted impedance data on a system level is crucial for system-level harmonic stability studies. To address harmonic stability issues, local compensation schemes are necessary to adjust the impedance of power converters and effectively introduce the desired damping. This dissertation aims to develop a standalone impedance measurement device, a harmonic stability

monitoring algorithm for a multi-bus network, and a harmonic instability mitigation method.

Major Scientific Contributions

This dissertation proposes four major scientific contributions which enable harmonic stability monitoring and a safe operation of PEDGs: 1) a standalone impedance measurement device to extract the grid impedance in a non-parametric manner; 2) a Frequency Coupling Matrix (FCM) measurement method for power converters; 3) a non-parametric harmonic stability monitoring method for multi-bus power systems; and 4) an advanced virtual damping control strategy for grid-connected power electronic converters.

The initial part of the thesis deals with the measurement of non-parametric impedances. A standalone plug-play measurement device called Wideband-frequency Grid Impedance (WFZ) measurement device is developed for the measurement of grid impedances. A low-power prototype of the proposed device is constructed. Linear impedance measurement is verified formerly by simulations followed by experimental measurements. Uncertainty characterization of the WFZ device is performed to validate the device.

The second part of this thesis considers non-linearity through the FCM and extends the measurement algorithm of the WFZ device to accommodate FCM measurements. Characterization parameters are developed for the analysis and interpretation of the extracted FCM. Simulative and experimental measurements were carried out to extract the FCM of a grid-connected converter, followed by validation of the extracted FCM.

The third part of the thesis proposes a non-parametric harmonic stability monitoring method. The proposed method requires non-parametric impedance measurements of active components in the network. A bus admittance matrix approach is considered to aggregate the non-parametric impedances of the power converters within the network. The proposed method enables the calculation of the minimum phase margin and the critical frequency where damping is required. The effectiveness of the method is demonstrated empirically through validation on both star and meshed power networks, showcasing its broad applicability across different network configurations.

In the last part of the thesis, a non-parametric approach to harmonic instability mitigation is proposed. The proposed method consists of a centralized non-parametric stability monitoring tool that identifies the critical frequency and bandwidth, which are then published to the local converters. The converters implement the damping through the proposed adaptive Virtual Damping Controller, which is implemented as a digital Infinite Impulse Response (IIR) filter with adaptive parameters such as the critical frequency and bandwidth; furthermore, a look-up table-based approach is proposed to select the optimal gain of the VDC based on the critical frequency and bandwidth. The proposed VDC controller only requires grid current measurement, establishing a two-degree-of-freedom (2-DoF) control structure. Experimental validations were conducted to show the efficacy of the proposed approach.

This thesis makes significant contributions in the areas of impedance measurement devices, system-level monitoring of harmonic stability, and the development of an advanced VDC, resulting in advancements in these fields.

Acknowledgments

Well, here we are. The end of a long, winding road paved with ambition, perseverance, hard work, a bit of procrastination, existential dread, and an alarming number of snacks. This dissertation exists primarily because I refused to give up not because it was easy, or fun, or remotely sane to attempt. First and foremost, I must thank myself for doing the actual work, for surviving on minimal sleep and maximum coffee, and for pushing through despite the overwhelming temptation to quit and become a monk in the Himalayas.

I extend my heartfelt gratitude to Prof. Antonello Monti, whose steady guidance, sharp insight, and generous mentorship have shaped this work in profound ways. A special thanks to Prof. Ferdinanda Ponci for her excellent guidance in the technical aspects of this work and for her thorough and constructive reviews of my publications. Her commitment and attention to detail significantly improved the quality of my research output. I am also thankful to Prof. Marco Liserre for his review and support of this dissertation. To my colleagues and peers at the Institute ACS, RWTH Aachen University, thank you for the stimulating conversations, collaboration, and camaraderie that made the challenges of this process bearable and sometimes even enjoyable. Special thanks to Manuel Pitz for his extensive support in the design and build of the WFZ device and special thanks to Yoga Kannan for his extensive support in the FCM topic and his support during the final hardware experiments.

To my parents - your love was the foundation long before this journey began. Every word written here rests upon years of your sacrifice and belief.

To my dear wife, Niranjana, thank you for holding the world together while I chased down thoughts and theories. Your calm, your patience, and your quiet strength were the truest support.

And now, the true catalyst behind this dissertations sudden acceleration: the impending birth of my daughter. Dhriti - you arrived like a sunrise on the horizon of my life. Even before your first breath, you

became my reason to finish, my reminder of what lies beyond deadlines and defense. This work is yours in spirit - born in the shadow of your light.

To my family and friends, thank you for pretending to understand my topic and for not asking, Are you done yet? too many times. And to the universe: thank you for not throwing in one last plot twist.

Contents

List of Publications

Journal Articles

[12] S. K. Gurumurthy, T. Heins, P. A. Ganeshamurthy, F. Ponci, and A. Monti. "Load Bus Frequency Estimation in Converter-Driven Grids-A Dynamic Phasor Approach". In: *IEEE Transactions on Power Systems* (2023). DOI: 10.1109/TPWRS.2023.3334194.

[25] S. K. Gurumurthy, M. Mirz, B. S. Amevor, F. Ponci, and A. Monti. "Hybrid dynamic phasor modeling approaches for accurate closed-loop simulation of power converters". In: *IEEE Access* 10 (2022), pp. 101643–101655. DOI: 10.1109/ACCESS.2022.3208963.

[29] T. T. Tran, S. K. Gurumurthy, M.-Q. Tran, T.-A. Nguyen-Huu, T. Heins, F. Ponci, A. Monti, and P. H. Nguyen. "Enhancing Performance of Andronov-Hopf Oscillator-Based Grid-Forming Converters in Microgrids With Non-Invasive Online Impedance Estimation". In: *IEEE Transactions on Smart Grid* 14.6 (2023), pp. 4479–4493. DOI: 10.1109/TSG.2023.3260721.

[53] M. Cupelli, S. K. Gurumurthy, S. K. Bhanderi, Z. Yang, P. Joebges, A. Monti, and R. W. De Doncker. "Port controlled Hamiltonian modeling and IDA-PBC control of dual active bridge converters for DC microgrids". In: *IEEE Transactions on Industrial Electronics* 66.11 (2019), pp. 9065–9075. DOI: 10.1109/TIE.2019.2901645.

Book Chapters

[17] S. K. Gurumurthy and A. Monti. "Converter-Based Dynamics and Control of Modern Power Systems". In: Academic Press, 2020. Chap. 11 - Dynamic Voltage Stability, p. 305. DOI: https://doi.org/10.1016/C2018-0-02717-6.

Conference Articles

[33] S. K. Gurumurthy, R. Uhl, M. Pitz, F. Ponci, and A. Monti. "Non-Invasive Wideband-frequency Grid Impedance Measurement Device". In: *2019 IEEE 10th International Workshop on Applied Measurements for Power Systems (AMPS)*. IEEE. 2019, pp. 1–6. DOI: 10.1109/AMPS.2019.8897787.

[51] S. K. Gurumurthy, M. Cupelli, and A. Monti. "A generalized framework for synthesizing virtual output impedance control of grid integrated power electronic converters". In: *2018 IEEE International Conference on Power Electronics, Drives and Energy Systems (PEDES)*. IEEE. 2018, pp. 1–6. DOI: 10.1109/PEDES.2018.8707895.

[52] S. K. Gurumurthy and A. Monti. "A Non-Parametric Approach to Harmonic Instability Mitigation for Renewable-Based Power Plants". In: *2024 IEEE 15th International Symposium on Power Electronics for Distributed Generation Systems (PEDG)*. IEEE. 2024, pp. 1–6. DOI: 10.1109/PEDG61800.2024.10667385.

Patents

[11] A. Monti, R. Uhl, and S. K. Gurumurthy. "Vorrichtung zur Emulation eines Versorgungsnetzes zur Validierung von Komponenten eines Stromversorgungssystems". DE102019217291A1. May 2021. URL: https://worldwide.espacenet.com/patent/search/family/073198313/publication/DE102019217291A1?q=pn%3DDE102019217291A1.

[32] A. Monti, S. K. Gurumurthy, R. Uhl, and M. Pitz. "Vorrichtung zur Bestimmung der Impedanz in Abhängigkeit der Frequenz eines zu messenden Versorgungsnetzes". DE102019214533A1. Mar. 2021. URL: https://worldwide.espacenet.com/patent/search/family/072665242/publication/DE102019214533A1?q=pn%3DDE102019214533A1.

1

Introduction

This chapter discusses the background and current trends in the energy sector and presents the motivation of this work. A brief overview of the new types of instability issues that arise due to the high penetration of renewables is discussed, and existing research gaps are identified. The research objectives of this dissertation are presented, followed by the contributions. Finally, the outline of the dissertation is presented.

1.1 Motivation and Focus

Over the past decade, there has been a significant increase in the penetration of Renewable Energy Sources (RES) in a wide range of countries. In Germany, renewable energy represented around 260 TWh, which is 60% of the total electrical energy generated for the year 2023, where wind energy is the largest contributor, followed by the contribution from Photovoltaic (PV) energy sources [1]. Owing to the ongoing climate crisis, desperate efforts are required to cut greenhouse gas emissions such as CO_2. Energy production companies, which were formerly relying on fossil fuels or nuclear power, have already begun to undertake large-scale projects to install PV and wind in an effort to phase out fossil fuel-based energy. For example, the German energy producer RWE aims to reduce its CO_2 emissions by 50% by 2030 and plans to further reduce its emissions to become climate neutral by 2040 [2].

Currently, there are several large PV installation, onshore, and offshore wind farm installation projects underway, which are fueled by the reformed Renewable Energy Sources Act (EEG 2017) [3]. This energy transition to renewables is not only taking place at the High Voltage (HV) transmission level but also at the Medium Voltage (MV) and Low Voltage (LV) levels

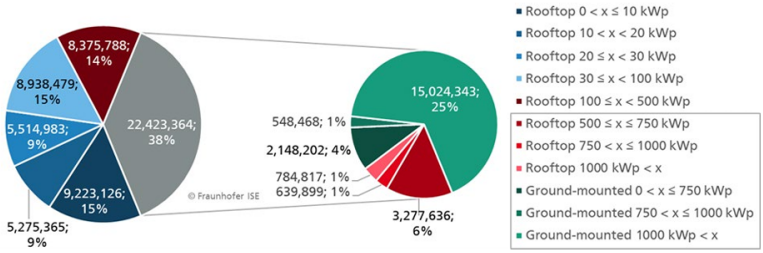

Figure 1.1: Distribution of PV according to size (year 2021) [4]

[4, 5]. Thus, there is a growing number of Distributed Energy Resources (DER) at the MV and LV levels. In Germany, the highest installation of PV is at the LV level, followed by the MV level. Fig. 1.1 shows the percentage of installed PV according to size, and it can be observed that around 62% of those installed PV have a capacity lower than 500 kW peak (kWp), and as they are roof top systems, they are typically installed in the LV grid [4, 5]. Typically, the installed PV is close to the loads, resulting in local production and consumption. However, on sunny days, a significant amount of power is generated and this power flows from the LV to the MV grid. This could potentially overload the transformers and stress the MV grid. Such power-flow problems have a direct correlation with both frequency and voltage stability issues.

An increase in renewable contribution leads to a reduction in inertia, which makes the grid weak, and furthermore, due to reversed power flows, which are volatile and fluctuating, the equivalent impedance of grids is also constantly changing. Owing to the reduction in inertia, rate-of-change of frequency (ROCOF) is increasing, which leads to significant sub-synchronous oscillations. The ENTSO-E guidance on high penetration of power electronics-based power sources presents the current overall inertia estimate for EU countries and also estimates the inertia when the percentage of RES tends towards 80% [6]. In [6], the total system inertia is defined and the role of novel strategies such as Virtual Synchronous Machine (VSM) which provide synthetic inertia, and the grid requirements of Grid-forming converter (GFM)s are discussed. Over the

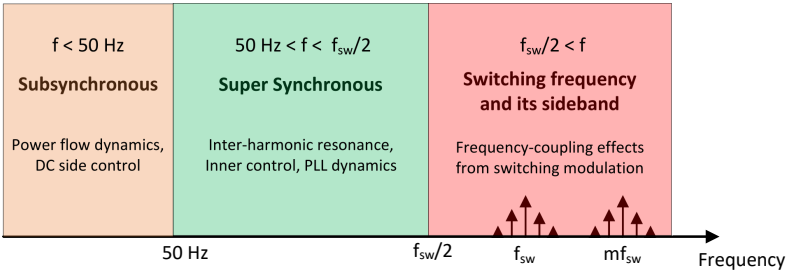

Figure 1.2: Classification of converter-driven stability based on frequency

last decade, several public projects were funded by the EU commission under the Horizon 2020 scheme. As the renewable penetration increases, the GFMs need to take up some of the roles of SGs, such as feeding fault current, inertia provision, black-start capability, sink for harmonics, etc., which ensures stable operation of the grid [7]. At the same time, this does not mean a complete eradication of Grid-following converter (GFL)s as GFMs are also prone to various instability issues that need to be addressed. GFLs would continue to play a key role in LV and MV grid. Along with the increase in RES, a ramp-up of battery storage technology is also required to support the transition. It is estimated that Germany requires around 950 GWh to 1500 GWh in storage, which is around 20 to 40 times the current installed capacity to reach 80% a renewable-dependent operation [8]. Apart from new roles of converters such as grid-forming, power system automation and monitoring tools should also go through a drastic change. New voltage monitoring techniques that consider both steady-state and transient conditions are required to monitor instabilities that arise due to converter interactions [9, 10]. To test converter-driven stability in the laboratory, grid emulators with advanced functions such as emulation of a wideband grid impedance, as proposed in [11], would be required. Additionally, frequency estimation techniques for fully converter-driven grids such as [12] are required as conventional approaches such as the frequency divider [13] are not suitable.

Owing to the increase in power-electronic converters, numerous types of instabilities have emerged across various frequency ranges. In

conventional power systems, the harmonics that occur are typically integral multiples of the fundamental frequency since these harmonics result from the presence of thyristor-based high-power rectifiers. For example, a thyristor-based rectifier-fed DC machine introduces odd harmonics such as 5th, 7th, and 11th harmonics [14–17]. To connect such large rectification units to the AC grid, solutions comprising phase shifting transformers were used to cancel and eliminate higher-order odd harmonics [16, 17]. Thus, it is necessary to classify the power system instabilities occurring in Power-Electronics Dominated Grid (PEDG)s based on frequency, as shown in Fig. 1.2.

- *Sub-synchronous*: refers to those phenomenon where the frequency of oscillation (f) is less than the fundamental frequency ($f < 50$ Hz). It occurs due to lack of damping in active and reactive power control loop or the DC link voltage control. Typically, this leads to sub-synchronous power swings, which could cause significant damage to assets such as Wind Turbine (WT) mechanical parts [18–20]

- *Super-synchronous*: typically refers to the inter-harmonic resonance that occurs in the range ($50 \text{ Hz} < f < \frac{f_{sw}}{2}$). It occurs due to Phase Locked Loop (PLL) or inner current control and the grid impedance. A negative feedback loop is formed through the ratio of converter and grid impedance and thus, if the phase difference between the converter and grid impedance is greater than or equal to 180 degrees at the frequency where the converter impedance magnitude equals the grid impedance magnitude, a net positive-feedback is formed at that frequency. Typically, this leads to medium-frequency resonance at inter-harmonic frequency and could cause potential tripping and depending on system-wide interaction, could lead to a partial blackout scenario [20–24]

- *Switching and sideband harmonics*: refers to the inter-harmonic resonance that occurs in the range ($\frac{f_{sw}}{2} < f$). It occurs due to frequency coupling mechanism of switching harmonics or the sideband harmonics with the sampling process. Low-frequency components of the sideband could excite LC resonance or could destabilize the inner current control loop [20, 21, 25]

There have been a growing number of instances where grid operators have noticed medium-frequency resonances that have affected the power

quality, have activated over-voltage tripping mechanisms, or, in the worst-case conditions, have the potential to cause irreversible damage to the semiconductors or to the magnetic components of the power converter. When the harmonic resonance propagates to different nodes and excites further resonance frequencies, it could threaten potential blackout scenarios.

BorWin1 is a Voltage Source Converter (VSC)-High Voltage Direct Current (HVDC) system in the North Sea that connects an offshore Wind Farm (WF) with the onshore main grid managed by the German Transmission System Operator (TSO) Tennet [26]. Due to the isolated nature of the grid and the presence of significant capacitance in lines, the impedance of the grid has several medium-frequency resonance points. This has led to harmonic instabilities. Analyzing the grid and converter impedance shows that under normal operation, the phase margin is around 41 degrees at 435 Hz and a small change in grid impedance is sufficient to excite harmonic resonance [26]. Another example is the Dutch Nieuwland project near Amersfoort, The Netherlands, which is an LV system. The system consists of nearly 500 PV-equipped homes capable of generating up to 1 GWh energy per year. It is observed from measurements that several inverters have tripped due to low power quality as the increased harmonic content causes violations of voltage limits [27].

It is important to note that a large number of converter-interfaced RES can lead to both sub-synchronous and super-synchronous situations [23]. The harmonic stability condition, as already explained, is due to the fast inner control bandwidth of converters, PLL-related instabilities, and parallel resonance among interconnected converters. Whereas sub-synchronous conditions arise owing to a mixed inertia situation due to improper damping in active or reactive power control, the Synchronous Generator (SG)s and power converters could potentially start swinging against each other uncontrollably. Frequency estimation in such grids is also quite critical. It is well known that under a classical setting with SGs, the frequency divider formula can be used to estimate the frequency of non-generation buses using the rotor speed information of generators [13]. However, this method is not suitable when loads and sources are distributed in the network, wherein the load currents are no longer insignificant compared to generator currents. Currently, for such new cases, novel modeling and estimation approaches based on state-space models are emerging [12].

This dissertation focuses on the harmonic stability (inter-harmonic) phenomenon, which is highlighted in green as illustrated in Fig. 1.2. Particularly, this dissertation addresses the measurement tools that are required for grids, data-driven stability monitoring of harmonic stability conditions in power grids, and the development of virtual damping solutions to mitigate harmonic instability.

1.2 Current Challenges

1.2.1 Converter and Grid Impedance Modelling Aspects

As harmonic stability is understood as an impedance-related phenomenon, it is necessary to obtain the impedance of the converter and the grid to perform the analysis. Modelling the converter as a transfer function, i.e., a parametric impedance, may not be sufficient since the impedance changes with different operating modes of the converter [28–31]. Parametric models of grid impedance are unreliable since the grid is often complex and a definite pole-zero description is error-prone. Thus, fitting measurement of impedance data to transfer function would not be practical since the numerator and denominator order of the grid impedance cannot be known with certainty. Furthermore, converter manufacturers or vendors protect their hardware and control algorithms with Intellectual Property Rights (IPR). Grid operators often require these details for modelling and stability analysis purposes. Thus, a standalone measurement device to measure the converter impedance in real-time is required. Furthermore, this measurement setup should not only be applicable to laboratory use but also directly to field measurements. Regarding grid impedance measurement, off-line computation of the grid impedance is insufficient since this impedance is influenced by numerous time-varying elements, including topologies, loads, and in-feeds [32, 33]. Hence, a standalone wideband grid impedance measurement device is required.

Power converters have several non-linearities introduced by the control system, PLL, influence of DC side dynamics, etc. Theoretical time and frequency domain models such as Linear Time Periodic (LTP) and Harmonic State-Space (HSS) models can describe these frequency coupling effects [34–37]. These approaches also require converter parameters and as mentioned previously, these details are protected by IPR. Grid operators would benefit from data-driven models. Instead

of theoretical modelling, empirically obtaining the model based on measurements would be advantageous. In this vein, several Frequency Coupling Matrix (FCM) measurement methods were introduced over the last decade [38–41]. A measurement setup that is suitable for laboratory and field application would benefit the FCM measurement process for real-world applications.

1.2.2 Stability Monitoring and Control Aspects

As mentioned above, grid operators require non-parametric impedance models of power converters to perform stability analysis [42, 43]. The conventional impedance-based stability criterion is applicable only for very simple systems involving two subsystems [42, 44]. However, this idea is not valid for a multi-terminal network since there are multiple interconnected subsystems. To overcome this problem, numerous approaches such as Component Connection Method (CCM), node admittance matrix-based aggregation, etc., were developed which aggregate the impedance at the system level [24, 44–46]. The above-mentioned methods do not consider non-parametric impedance models. It is essential to investigate and develop suitable impedance aggregation methods, considering non-parametric impedance.

The stability of interconnected system depends on both the grid impedance and converter impedance and grid voltage distortions can significantly impact the current harmonics that the converters inject [37, 47, 48]. As such, classical Active Damping (AD) methods, which do not consider grid impedance variation, are not suitable for mitigating harmonic instability. The converter impedance needs to be adapted based on the measured grid impedance so that the interconnected system is stable. Furthermore, parametric models of grid impedance are unreliable since the grid is often complex and a definite pole-zero description is error-prone. Methods that require parametric impedance models are not suitable for practical field application [47, 49–52]. Another set of approaches that use principles of passivity and Port-Controlled Hamiltonian (PCH) framework are emerging [53, 54]. However, the influence of grid impedance on such systems is not clear, and furthermore, how to adapt such controllers based on measured grid impedance needs to be studied.

1.3 Research Questions

Based on the understanding of what is currently lacking, the following research questions (**RQ**s) are formulated:

1. **RQ1**: How to measure non-parametric impedance from a standalone device and how to characterize such a wideband impedance measurement device ?

2. **RQ2**: For capturing non-linearity, FCM is proposed in literature. How accurate is this method ? How to extract the FCM of a converter from a standalone device and how to characterize the measurements ?

3. **RQ3**: Can locally measured converter impedances be aggregated on a system level to make predictions of system level stability ? How to evaluate stability margins for a multi-bus system using non-parametric impedance data ?

4. **RQ4**: Assuming the availability of stability monitoring, how to shape the impedance of the converter to achieve damping for a wide frequency range ?

1.4 Research Proposal and Contributions

Based on the postulated research questions, this dissertation has developed the following research proposals and contributions: Each of the research questions has led to a dedicated research contribution.

This work proposes a power-electronics-based Wideband-frequency Impedance (WFZ) measurement device. Upon triggering the device, the device injects wideband perturbation currents into the Point of Common Coupling (PCC). By measuring the PCC voltage and injected grid current, the impedance data is extracted for various frequency points. Various possible operational sequences of the device are explained and the operational sequences are compared. An empirical method to characterize the accuracy of such a wideband impedance measurement device is explained.

To empirically extract the FCM of the converter, this work extends the wideband excitation-based measurements. In the proposed method,

numerous repetitions of wideband perturbation currents are applied at the PCC, and both the PCC voltage and current are recorded. Through a least-square formulation, the FCM of the converter is extracted. To assess the correctness of the extracted FCM and to interpret it, this work proposes characterization parameters for the FCM. By calculating the diagonal dominance of the extracted FCM, the degree of non-linearity can be assessed.

This work proposes an impedance-based stability criterion for multi-bus power network. The proposed method is suitable for any arbitrary topology such as star, radial and meshed topologies. Using bus admittance matrix, a Multiple Input Multiple Output (MIMO) transfer function is proposed where the converters in the grid act as inputs and the node voltages are the outputs. Converter impedances are obtained experimentally as explained earlier. The critical resonance frequency and stability margins are identified from the stability criterion.

To mitigate harmonic resonance, the non-parametric harmonic stability monitoring tool is required. This tool identifies the critical frequency where resonance could occur and identifies two corner frequencies between which the phase margin of the system should be above a predefined threshold. The non-parametric stability monitoring tool identifies both the critical frequency and bandwidth and passes this information to individual converters. The converters implement damping through the proposed adaptive Virtual Damping Controller (VDC), which is implemented as a digital Infinite Impulse Response (IIR) filter with adaptive parameters such as the critical frequency and bandwidth. Upon receiving the adaptive parameters from the monitoring tool, the controller swiftly adjusts the impedance within a brief interval of 1.5 times the sampling period. Additionally, the VDC operates effectively with only grid current measurements, establishing a 2-Degrees-of-Freedom (DoF) control structure.

The research contributions (**RC**s) of this dissertation are summarized as follows:

1. **RC1**: A standalone WFZ device and its uncertainty characterization
2. **RC2**: A WFZ device based FCM extraction method and its uncertainty characterization

3. **RC3**: A non-parametric harmonic stability monitoring method for multi-bus power system

4. **RC4**: Advanced VDC strategy for grid-connected power electronic converters

To address the harmonic stability problem in PEDGs, this dissertation has undertaken a non-parametric impedance based approach. Thus, the core of the dissertation is the WFZ device which is developed to measure the non-parametric impedance. Building upon the above foundation, this dissertation has two aspects: 1) *non-parametric modelling and measurement* aspect and 2) *stability analysis and control* aspect. In the *non-parametric modelling and measurement* aspect, the FCM measurement method is proposed which overcomes the limitation of linear impedance models and in the *stability analysis and control* aspect, an impedance data based harmonic stability monitoring and an advanced virtual damping control strategy is developed. Fig. 1.3 shows the structure of the dissertation along with the contributions.

1.5 Dissertation Outline

The remainder of the dissertation is organized as follows:

Chapter 2 introduces the WFZ device. The hardware and software components of the device are explained, followed by the operational sequence of the device. For direct-quadrature (dq) impedance measurement, two operational sequences are proposed: sequential and parallel method. Detailed switched model-based simulations are carried out to validate the impedance measurement and the impact of perturbation amplitudes and control bandwidth on the accuracy and Total Harmonic Distortion (THD) are analyzed. Experimental validation of the proposed device is achieved by firstly constructing a low-power prototype of the device and validating its impedance measurement capabilities. Through extensive experimental trials, the device is characterized by determining its accuracy. Two types of uncertainty characterization are carried out: wideband and per-frequency characterization.

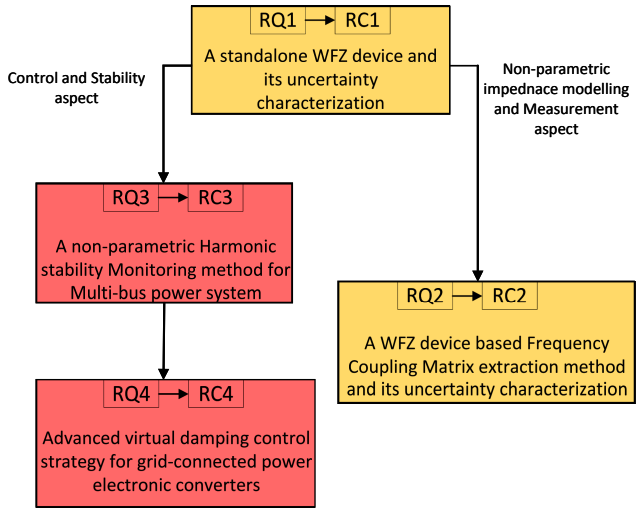

Figure 1.3: Dissertation structure and contributions

Chapter 3 explains the FCM concept and proposes a WFZ device-based FCM extraction method. An empirical approach to extract FCM is proposed based on a least-squares formulation. Following the measurement method, the characterization parameters of the FCM which enable the interpretation of the extracted FCM and help adjudge the accuracy are covered. The non-linear index allows adjudging the diagonal dominance of the FCM and the mean absolute error calculation allows both wideband and per-frequency characterization of the FCM. Simulation studies are conducted for a three-phase LCL-filtered power converter, and the influence of inner control parameters is studied. Finally, this chapter provides experimental validation by measuring the FCM of a three-phase power converter and compares the efficacy of the FCM model and the linear impedance model.

Chapter 4 discusses the various approaches for performing harmonic stability analysis with a clear focus on impedance-based stability methods. A non-parametric formulation of the impedance-based stability criterion

is introduced. Extension of this approach for multi-bus power grids is explained. Simulation scenarios show the applicability of the proposed approach for various types of grids: Star connection, radial grid and meshed systems. The impact of grid impedance, converter inner control parameters and the line impedances are discussed. Finally, experimental verification is carried out using a power-electronic rapid prototyping system.

Chapter 5 proposes an advanced virtual damping control strategy. Firstly, based on the stability analysis concept introduced in 4, this chapter proposes a stability monitoring algorithm which detects the critical resonance frequency and identifies the frequency range (bandwidth) where damping is required. Secondly, this chapter proposes a virtual damping control strategy, which is a decentralized solution implemented at each converter station locally. Selection of the gain parameter through a look-up table is explained. Experimental verification is carried out to empirically validate the proposed method, and the impact of control parameters on the damping performance is thoroughly analyzed.

Chapter 6 summarizes the dissertation and provides the conclusions obtained from this work. The outlook for future work is also provided.

2

Linear Wideband Impedance Measurement

2.1 Introduction

2.1.1 Motivation

A rising number of harmonic instability and power quality problems have been observed recently due to the wide bandwidth behavior of power-electronic converters [22, 23]. High control bandwidths, PLL-induced non-linearity, and parallel resonance phenomena have been shown to potentially increase the susceptibility to harmonic instability [55, 56]. Weak grids often have low inertia and high grid impedance [56]. Harmonic stability is widely characterized as an impedance phenomenon [21] and thus there is a growing need to develop closed-loop impedance models of power converters and to develop impedance based stability analysis tools. Hence, the extraction of impedance is vital for the stability monitoring and harmonic mitigation of PEDGs.

To avoid instability, grid-connected converters must support and enable grid operation. GFL provide frequency and voltage support in LV and MV power grids through active frequency controlled through active and reactive power based de-rating logic [57]. This helps in the stabilization of the fundamental 50 Hz component. However, knowing some attributes of the grid, such as grid impedance at different locations, allows the analysis of the grid stability and could potentially enhance its operation for a wide range of frequencies. An off-line computation of the grid impedance is insufficient since this impedance is influenced by numerous time-varying elements, including topologies, loads, and in-feeds together with their characteristics. Furthermore, adequate simulation models for frequencies higher than the fundamental are rarely accessible [58]. Consequently, it

is necessary to extract the grid impedance at any node in the grid. A wide frequency range must also be used for this type of measurement to capture interesting effects such as resonance peaks.

2.1.2 Review of Impedance Extraction Methods

In the last decade, wideband impedance measurement has been gaining widespread attention since the method is fast and allows the possibility of non-invasive signal injection by making use of the embedded environment of a power-electronic converter. The term *non-invasive* in the context of impedance measurement has been used in a number of ways:

1. Standpoint of additional hardware requirements: Grid-connected converters may require knowledge of grid impedance to enhance their damping capability and for enhanced control of active and reactive power. In this context, non-invasive methods are those that do not require additional measurement apparatus apart from the converter itself for the measurement of impedance [28, 29, 32, 33]

2. Standpoint of PCC voltage distortion: Impedance measurement devices typically need to inject or draw perturbation currents to disturb the PCC voltage. Non-invasive methods are those which do not significantly distort the PCC voltage and with such methods the THD is within limits [28, 29, 32, 33]

By linear impedance, it is assumed that the current harmonic at some arbitrary frequency point h induces a voltage drop at the same frequency point h. The cross-coupling among frequencies are negligible under this assumption. Consider that the terminal voltage and current across the Device Under Test (DUT) is v and i respectively. In the Laplace or s-domain, the voltage drop across the DUT depends on the impedance (Z) of the DUT and it is expressed as in (2.1). In (2.1), the impedance of the DUT which is basically a transfer function is called *parametric impedance* model since only the numerator and denominator polynomial coefficients are required to describe the wideband frequency behavior.

$$v(s) = Z(s)i(s) \tag{2.1}$$

Re-writing (2.1) in the matrix form by considering discrete set of injected frequency points ω_1, ω_2, ..., ω_h as shown in (2.2), enables a

data-based formulation of impedance, which is called as *non-parametric* impedance. From (2.2), it is clear that the off-diagonal interactions are ignored and the model is linear under this assumption. Due to the one-one mapping between frequency components v and i, the frequency components of $i(j\omega)$ can be excited simultaneously and the response v can be measured which enables the determination of the impedance at all the discrete frequency points of interest.

$$\begin{bmatrix} v(j\omega_1) \\ v(j\omega_2) \\ \vdots \\ v(j\omega_h) \end{bmatrix} = \begin{bmatrix} z_{11} & 0 & \dots & 0 \\ 0 & z_{22} & \dots & \vdots \\ \vdots & \vdots & \ddots & \vdots \\ 0 & \dots & \dots & z_{hh} \end{bmatrix} \begin{bmatrix} i(j\omega_1) \\ i(j\omega_2) \\ \vdots \\ i(j\omega_h) \end{bmatrix} \tag{2.2}$$

This section reviews the existing impedance extraction methods and classifies them mainly into two categories i.e. large signal and small signal methods.

Large signal methods are those where the injected disturbance could significantly perturb the grid voltage waveform at the PCC [58–60]. A typical use-case for the large signal method is based on a load switching approach [58, 59]. The device consists of a three phase full bridge rectifier and the DC side of the device consists of a series connected IGBT and a load resistor. As the IGBT is switched, pulsed DC load current flow through the resistor and thus the PCC is disturbed. Two techniques are typically employed for the switching: wave packaging technique and inter-harmonic technique [58, 59]. In wave packaging technique, a medium frequency square wave switching is performed and in the inter-harmonic method, a sequential square wave load switching is performed. Both methods offer identical accuracy and frequency resolution. The voltage perturbation observed at the PCC and the applied load current are used to estimate the grid impedance. Alternatively, a current pulse of a short duration can be applied to the power system to extract the impedance at the PCC [60].

Large signal methods are undesirable as the disturbance is significant. Power quality of the grid is severely impacted by the measurement process. The system states are moved significantly from their steady state operating point and may potentially destabilize the system; particularly if the system is operating in marginally stable conditions. Furthermore, since the Region of Attraction (ROA) of complex interconnected power

systems is hard to estimate, the design of the large signal perturbation amplitude is complicated and currently there is no literature on this topic. These reasons motivate towards the usage and research of advanced small-signal methods.

Small signal methods only inject a minor perturbation from which the impedance of the grid is extracted. A basic impedance measurement setup consists of a network analyzer capable of signal generation and perform impedance calculation, a power amplifier capable of interfacing the network analyzer and the power circuit and a medium frequency isolation transformer [61–64]. The network analyzer performs a sinusoidal sweep from a specified minimum to maximum frequency and this signal is amplified by the power amplifier and the voltages are injected into the power circuit through the medium frequency transformer. The voltages and currents recorded at the PCC are used to calculate the impedance. Commercial products such as IOZ/VLA2500 from Venables provide the possibility of impedance measurement kits which includes a power amplifier and medium frequency transformer [61, 62]. Sinusoidal sweep methods typically result in large measurement time whereas broadband measurement techniques can achieve significant reduction in duration. Broadband methods use control loops to inject small-signal perturbations and these techniques can be integrated into already existing power electronic converters [28–30]. These are typically achieved in methods that use Psuedo Random Binary Sequence (PRBS) to extract the grid impedance [28–31, 65]. Measurement errors caused due to non-linearity can be reduced by using ternary sequence [31]. While these techniques are capable of extracting the grid impedance from existing power electronic converters, a standalone and mobile impedance measurement device with high plug-play capability is required such that the grid impedance at arbitrary location can be extracted.

2.1.3 Main Contribution

This work proposes a power-electronics-based flexible, low cost, mobile wideband-frequency grid impedance (WFZ) measurement device [32, 33]. The proposed device does not require a dedicated DC power supply and the DC side contains only a DC link capacitor. The device starts by charging the DC link capacitor to a nominal voltage through a pre-charge circuit or an active / passive front end. Once the device is grid connected,

it maintains the DC link voltage to the reference value through an outer DC link voltage controller. Under this state, the device only draws a small current to compensate for losses in the switches and the leakage in the DC link. The current regulation is performed through an inner current control in *dq* domain. The proposed device generates small-signal perturbations by injecting a short white noise burst on top of the controllers output. As a result, no significant transient disturbances are introduced, but the impedance of the grid can be measured accurately over a wide frequency range up to one sixth of the switching frequency. During the measurement process, the device only injects perturbation currents. Thus, the WFZ device need not be built for carrying high power or current. The DC link capacitor can be sized based on the maximum DC side voltage fluctuation and perturbation current on the AC side.

This work proposes two operational sequences for the WFZ device to measure impedance in *dq* domain: Sequential and Parallel method. The *dq* impedance matrix Z_{DQ} contains 4 components, namely, Z_{dd}, Z_{dq}, Z_{qd} and Z_{qq}. With the sequential method, the impedance Z_{dd} and Z_{qd} is measured by perturbing the *d*-axis currents and then the impedances Z_{qq} and Z_{dq} is measured by perturbing the *q*-axis currents. Instead of sequentially measuring the *d* and *q* channel impedances, it would be advantageous to simultaneously measure the entire *dq* impedance matrix with one measurement cycle. This is possible through the parallel method. By adopting the orthogonal signal generation approach in [65], where both the *d* and *q*-axis currents can be simultaneously perturbed, simultaneous measurement of all elements of the *dq* impedance matrix is possible. Such an adaptation enables reduced measurement time for a given frequency resolution. Apart from *dq* impedance measurement, the proposed device can measure the the impedance in the stationary domain and in the sequence domain through post processing.

This work extensively analyses the sequential and parallel method in terms of measurement accuracy and THD levels for different magnitudes of PRBS levels. Furthermore, this work analyses the impact of PRBS amplitude on the accuracy and studies the influence of gird impedance magnitude on the measurement accuracy and THD levels.

Experimental validation through a low power prototype is provided in grid-connected mode. Two uncertainty characterization methods are proposed for the wideband impedance measurement device. Wideband characterization enables the accuracy evaluation for the overall frequency

range of the device. Per-frequency characterization calculates the measurement uncertainty at each frequency. Using the experimental data, the proposed characterization methods are applied for the constructed device.

2.2 Wideband-frequency Impedance (WFZ) Measurement Device

2.2.1 Operating Principle

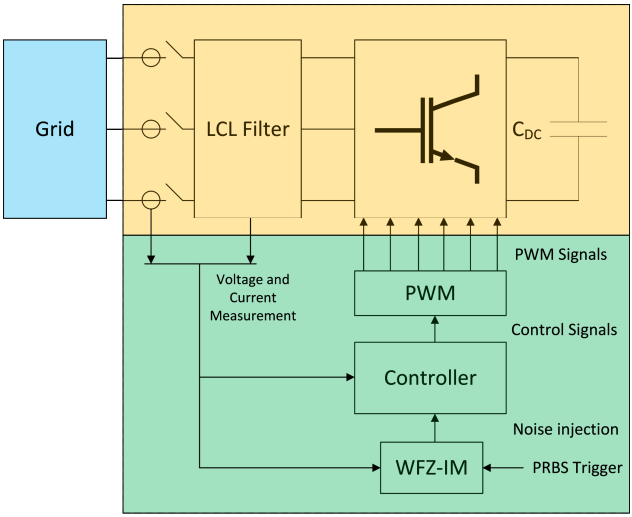

Figure 2.1: Functional block diagram of WFZ device

Fig. 2.1 shows the functional block diagram of the WFZ device. The proposed device does not require a dedicated DC power source apart from the three phase grid connection and thus the device has plug-and-play capability. The DC link capacitor is initially charged to the nominal DC voltage in order for the device to operate. The device introduces wideband perturbed currents into the grid when it is triggered to measure impedance. These disturbances propagate to the PCC, and the perturbation currents

flow through the equivalent grid impedance seen by the device which in effect determines the magnitude of voltage disturbance at the PCC. As a result, the non-parametric grid impedance can be measured. The device measures the Thevenin equivalent impedance if many branches are joined at the PCC. It should be emphasized that the device only injects band-limited perturbed currents and the fundamental component of current is nearly zero. Thus the design and sizing of the WFZ device is not based on the power but rather based on the current limits during the perturbation phase. The perturbation signal consists of a PRBS signal. The PRBS injected in the duty cycle is an input disturbance to the controller and the controller suppresses the low frequency dynamics. The PRBS is generated through an N-bit shift register wherein the first bit is updated by the XOR operation of N^{th} and $(N-1)^{th}$ bit [28, 33]. Let us consider the PRBS injection and sampling frequency as f_{inj} and let M be the number of rounds of PRBS. The total number of samples corresponding to M rounds of PRBS is given by (2.3).

$$N_{samples} = M(2^N - 1) \tag{2.3}$$

The fundamental principle in extracting the non-parametric impedance is explained here. The impedance measurement device operates in grid connected mode and the measurement device hosts its own internal synchronization unit such as a PLL to remain synchronized with the PCC voltage. The equivalent circuit diagram of the measurement setup is shown in Fig. 2.2. The measurement device acquires sampled current

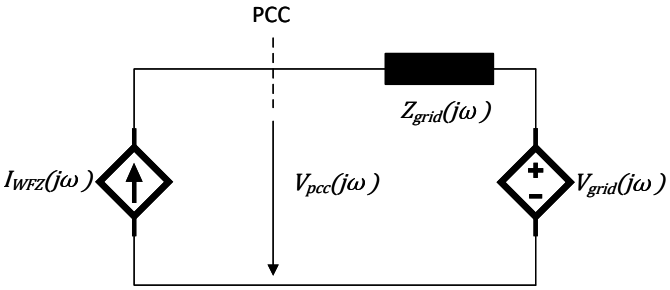

Figure 2.2: Thevenin equivalent diagram

and voltage measurements at the PCC. Impedance measurement process consists of two phases. The first phase is the scanning phase where for a fixed number of samples N_f, the device scans the background harmonics in the voltage and current. The spectrum of the voltage and current is obtained by Fast Fourier Transform (FFT). Consider that the spectrum of voltage and current during the scanning phase be $V_{no,pert}(j\omega)$ and $I_{no,pert}(j\omega)$ respectively. After the scanning phase, the perturbation phase begins. The device injects perturbed currents into the PCC; and depending on the grid impedance Z_{grid}, the voltage at the PCC gets perturbed. The perturbation currents are typically obtained by injecting a quasi white noise signal to the duty cycle of the measurement device. A very commonly used digital approximation of a white noise is a PRBS signal which are digitally generated through shift register circuits. Consider that the spectrum of voltage and current during the perturbation phase be $V_{pert}(j\omega)$ and $I_{pert}(j\omega)$ respectively. The non-parametric impedance of the grid at frequency ω_i can be computed using (2.4). Since the injected perturbation is wideband containing many frequency components, the impedance can be extracted at all frequency points between the minimum frequency (ω_{min}) and maximum frequency (ω_{max}) point i.e. within the interval $\omega_{min} \leq \omega_i \leq \omega_{max}$.

$$Z(j\omega) = \frac{V_{pert}(j\omega) - V_{no,pert}(j\omega)}{I_{pert}(j\omega) - I_{no,pert}(j\omega)} \tag{2.4}$$

In (2.4), $V_{pert}(j\omega)$ and $I_{pert}(j\omega)$ represents the FFT of the voltage and current during noise injection and $V_{no,pert}(j\omega)$ and $I_{no,pert}(j\omega)$ represents the FFT of the voltage and current before noise injection. Before performing the FFT, a hanning window is applied to the time domain samples to reduce spectral leakages due to discontinuities. The following assumptions are involved for the validity of the obtained non-parametric impedance:

1. Measured grid impedance is linear and in case of non-linearity, the non-linear effects are negligible i.e. the cross-coupling effects among different frequency components are negligible
2. Measured grid impedance does not vary during the measurement process
3. Background harmonics and floor noise in the measured grid voltage does not vary considerably during the measurement process.

2.2.2 Hardware Description

As shown in Fig. 2.1, the device consists of a three-phase full bridge converter based on the 2-level B6C topology. A LCL filter with passive damping solution is used on the AC side to eliminate switching harmonics. A split capacitor type shunt RC damper is used to reduce the resonance caused by the LCL filter. The DC side consists of a DC link capacitor and a three phase diode full bridge rectifier. The rectifier functions as a pre-charging passive front end and it is only utilized at startup. Measurement boards that are precise and modular are built to measure both the DC and AC sides of voltages and currents. The measurement boards are equipped with galvanic isolation for safety and to protect the embedded environment from high voltages. To enable experimental validation, a prototype of the WFZ device is built, as detailed in Section 2.5.1.

2.2.3 Software Description

The software components consist of a controller, Pulse Width Modulation (PWM) generator and the WFZ-Information Management (IM) functionality.

Controller

The controller is a cascaded design that consists of an inner grid side current control and an outer DC link voltage controller. The control is implemented in the *dq* domain. An Synchronous Reference Frame (SRF)-PLL is utilized to synchronize with the grid; it supplies the reference angle needed to convert between *dq* and stationary reference frames. Fig. 2.3 shows the control diagram. The gate pulses are generated by the PWM generator using a 2-level space vector PWM. The perturbation signal is superimposed on the duty cycle output of the controller by the WFZ-IM. Since the inner current control loop usually has a high pass disturbance rejection transfer function, adding a perturbation to the duty cycle will only cause low frequency information to be lost. (2.5) defines the input disturbance rejection transfer function $R(s)$, where the current controller transfer function is $K_{cc}(s)$, and the plant's transfer function is $G_{id}(s)$. Therefore, at low frequencies, an improved impedance

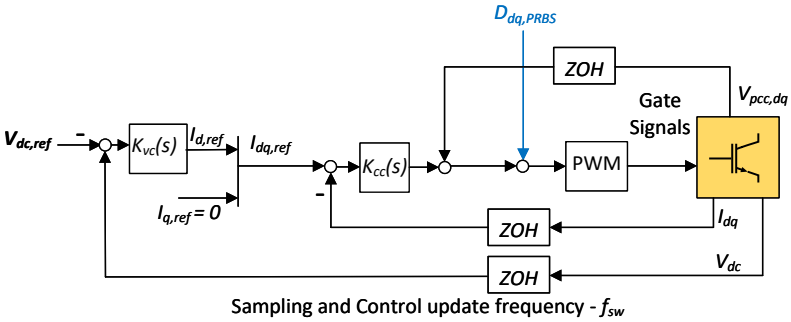

Figure 2.3: Control structure of the WFZ device

extraction would result from a low bandwidth of $K_{cc}(s)$. Section 2.4.3 discusses the effect of the controller bandwidth.

$$R(s) = \frac{1}{1 + G_{id}(s)K_{cc}(s)} \tag{2.5}$$

WFZ-IM

WFZ-IM comprises of the PRBS generator, a First-In-First-Out (FIFO) buffer and a non-parametric impedance calculation algorithm. PRBS is a well-known band-limited white noise signal that is simple to produce digitally using shift-register logic [28, 29]. The PRBS signal has a definite and known length. The sampling and PRBS injection frequency are equal and are typically set equal to the switching frequency of the WFZ device. At each sampling instant, the PCC voltage and current samples are obtained and stored in the FIFO buffer. Section 2.3 discusses the size requirements of the buffer. Either an internal or external trigger could be used to commence the measurement process. In power system automation, the impedance measurement trigger would be externally set.

The WFZ-IM initiates the scanning phase upon receiving the measurement trigger. During the scanning phase, the WFZ-IM waits for the required duration of the PRBS signal to obtain unperturbed voltage and current samples into the FIFO buffer. Subsequently, the WFZ-IM injects the PRBS perturbation of specified amplitude onto the duty

cycle of the controller. The perturbed voltage and currents are samples are stored in the FIFO buffer simultaneously. The trigger to evacuate the FIFO buffer is generated internally when the perturbation phase is over. The non-parametric impedance is computed by first performing an FFT on the voltage and current samples, subsequently carrying out the computation in (2.4).

Remarks on Perturbation Design

The minimal magnitude of impedance that needs to be measured determines the size of the PRBS amplitude. The voltage perturbation on the PCC is proportional to the impedance magnitude for as given perturbation current. Measurement of low impedance magnitudes require larger disturbance currents. However, THD increases with higher PRBS perturbation amplitudes and thus there is a trade-off between THD levels and accuracy of the measured impedance. Selection of PRBS amplitude is critical as it depends on the maximum THD levels and the minimum impedance that needs to be extracted. Section 2.4.4 performs the aforementioned analysis and provides recommendations on the selection of PRBS amplitude.

2.2.4 Wideband Grid Impedance Identification

Additionally, the non-parametric impedance data may be converted into a parametric impedance model $Z_{grid}(s)$ using the complex curve fitting approach [66, 67]. Assume that non-parametric data is obtained at frequencies $\omega_1, \omega_2, \cdots, \omega_N$, where ω_N corresponds to the Nyquist frequency. The accuracy of the measured non-parametric impedance is low close to the Nyquist frequency, particularly between the interval $\omega_N/3$ to ω_N. Therefore, it is advisable to set the maximum limit for the frequency data point as $\omega_{max} = \omega_N/3$. In the lower frequency range, the accuracy of the impedance is lowered due to active disturbance rejection by the controller.

Weighted Complex Curve Fitting - Levy method

The non-parametric impedance data ($Z_{np}(j\omega_i)$) is fitted to the transfer function in this study using the weighted complex curve fitting Levy

method [66, 67]. Consider the generic transfer function to which the data should be fitted as:

$$Z_{grid}(s) = \frac{N(s)}{D(s)} = \frac{n_0 + n_1 s + n_2 s^2 + ... + n_p s^p}{1 + d_1 s + d_2 s^2 + ... + d_q s^q} \tag{2.6}$$

In (2.6), $N(s)$ and $D(s)$ denotes the numerator and denominator polynomial, $n_0 \ldots n_p$ denotes the coefficients of $N(s)$ and $d_1 \ldots d_q$ denotes the coefficients of $D(s)$.

Consider the error ϵ as the difference between the non-parametric impedance data and the fitted transfer function data $Z_{np}(s) - N(s)/D(s)$. Since the transfer function is in a fraction form, let us define $\epsilon' = Z_{np}(s)D(s) - N(s)$ to be the modified error function which is obtained by multiplying ϵ with $D(s)$. The unknowns which are the coefficients in the numerator and denominator can be stacked as follows:

$$\boldsymbol{x} = \begin{bmatrix} n_0 & n_1 & \cdots & n_p & d_1 & d_2 & \cdots & d_q \end{bmatrix}^T \tag{2.7}$$

Considering the definition of ϵ' and $\boldsymbol{x}$, a linear equation of the form $(\boldsymbol{A}\boldsymbol{x} - \boldsymbol{b})$ can be formed wherein $\boldsymbol{A}$ is given by (2.8) and $\boldsymbol{b}$ is given by (2.9).

$$\boldsymbol{A} = \begin{bmatrix} 1 & j\omega_1 & \cdots & j\omega_1^p & -j\omega_1 Z_{np}(j\omega_1) & \cdots & -j\omega_1^q Z_{np}(j\omega_1) \\ 1 & j\omega_2 & \cdots & j\omega_2^p & -j\omega_2 Z_{np}(j\omega_2) & \cdots & -j\omega_2^q Z_{np}(j\omega_2) \\ \vdots & \vdots & \cdots & \vdots & \vdots & \cdots & \vdots \\ 1 & j\omega_M & \cdots & j\omega_M^p & -j\omega_M Z_{np}(j\omega_M) & \cdots & -j\omega_M^q Z_{np}(j\omega_M) \end{bmatrix} \tag{2.8}$$

$$\boldsymbol{b} = \begin{bmatrix} Z_{np}(j\omega_1) & Z_{np}(j\omega_2) & \cdots & Z_{np}(j\omega_M) \end{bmatrix}^T \tag{2.9}$$

The fitting corresponding to each frequency data point is represented by each row in the linear equation $(\boldsymbol{A}\boldsymbol{x} - \boldsymbol{b})$. Consider M valid frequency data points that are to be used in the complex curve fitting and considering p, q to be the order of numerator and denominator polynomial, the size of $\boldsymbol{A}$ matrix is $M \times (p + q + 1)$.

Since the accuracy of PRBS is low at lower frequencies, additional sinusoidal frequencies at arbitrarily lower frequencies, say 80Hz or 90Hz, can be superimposed over the PRBS to strengthen the perturbation at

those lower frequencies. Thus, by defining a diagonal weighting matrix $\boldsymbol{W}$, weighting or penalisation can be applied to these superimposed frequency data points and hence a Weighted Least Square (WLS) problem can be formulated. The objective function of WLS method is shown in (2.10).

$$\min_{\boldsymbol{x}} \quad ||\boldsymbol{W}(\boldsymbol{A}\boldsymbol{x} - \boldsymbol{b})||_2 \tag{2.10}$$

The solution of the WLS problem is given by (2.11).

$$\boldsymbol{x} = (\boldsymbol{A}^{\boldsymbol{T}}\boldsymbol{W}\boldsymbol{A})^{-1}\boldsymbol{A}^{\boldsymbol{T}}\boldsymbol{W}\boldsymbol{b} \tag{2.11}$$

If the desired impedance transfer function is assumed to take the form $Z(s) = R_{grid} + sL_{grid}$ and thus the generic transfer function to which the non-parametric data is fitted takes the form $Z_{grid}(s) = n_0 + n_1 s$, wherein $p = 1$, $q = 0$. Thus, the coefficient $n_o = R_{grid}$ and the coefficient $n_1 = L_{grid}$.

2.3 Operational Sequence of WFZ Device

The operational sequence of the WFZ device is covered in this section. For the stationary domain, the impedance measurement equation is defined in (2.4). The voltage-current relationship in the dq domain can be expressed as follows:

$$\begin{bmatrix} V_{pcc,d} \\ V_{pcc,q} \end{bmatrix} = \begin{bmatrix} Z_{grid,dd} & Z_{grid,dq} \\ Z_{grid,qd} & Z_{grid,qq} \end{bmatrix} \begin{bmatrix} I_{pcc,d} \\ I_{pcc,q} \end{bmatrix} \tag{2.12}$$

The entries of the dq impedance matrix are as follows: $Z_{grid,dd}$, $Z_{grid,dq}$, $Z_{grid,qd}$, and $Z_{grid,qq}$.

Depending on the excitation technique, there are two types of impedance extraction in the dq domain: sequential and parallel. The sequential method involves perturbing the d and q-axis currents one after the other, whereas the parallel method perturbs both the d and q-axis currents simultaneously [65]. Generally speaking, the impedance components $Z_{grid,dd}$ and $Z_{grid,qd}$ can be extracted by perturbing the d-axis current, and the impedance components $Z_{grid,dq}$ and $Z_{grid,qq}$ can be extracted by perturbing the q-axis current.

The operational sequence proposed in [33], which includes a discharge phase to extract the impedance, is improved in this work. It is not

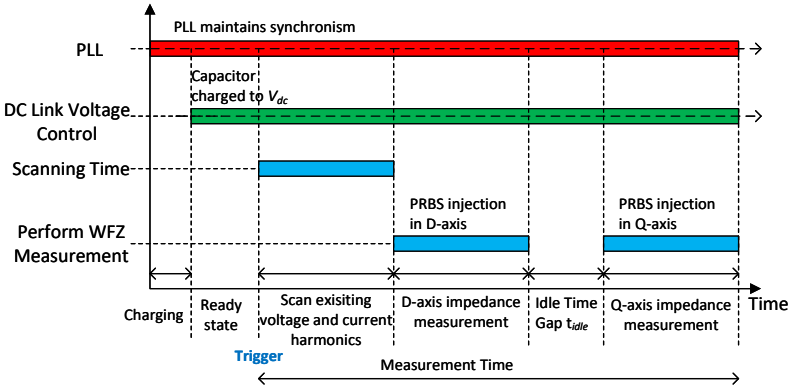

Figure 2.4: Timing diagram of sequential method

necessary to have such a discharge phase. Since the proposed WFZ device contains a DC link voltage controller, the q-axis current reference can be zero while the d-axis current reference maintains the DC link voltage. To maintain the DC link voltage and compensate for switching losses and capacitor losses, the WFZ device usually requires a small amount of current. The DC link voltage only fluctuates around its reference value during the perturbation phase, and the dq currents also fluctuate around its reference value of zero during the perturbation phase. The dq currents are nearly zero in steady state.

2.3.1 Sequential DQ Impedance Extraction

Fig. 2.4 shows the timing diagram for the sequential DQ impedance measurement.

Startup sequence

Detecting the voltage at the PCC is the first step in the startup procedure. The WFZ device uses a three phase PLL to synchronize with the PCC voltage. The converter charges the DC link voltage to the intended nominal voltage on the DC side by operating in rectifier mode. Once the DC side capacitor is charged to the reference DC voltage, the device

goes into a ready state. To maintain the DC link voltage under steady state conditions, a negligible d-axis current is drawn to compensate for switching losses and capacitor leakage. The q-axis current is zero.

Scanning phase

The device enters into scanning phase after receiving the trigger to measure impedance. The device records the voltage and currents sampled at the PCC for a predetermined number of PRBS signal rounds during this phase. The total number of samples to be recorded for each electrical phase is $M_r(2^{N_{bit}} - 1)$, where M_r is the number of rounds of PRBS and N_{bit} is the number of shift register bits used in the PRBS generation.

Perturbation phase

Following the completion of the scanning phase, the device enters the perturbation phase. The perturbation phase in sequential mode is divided into three separate sections. First, only the d-component of control signal receives a PRBS perturbation; this allows for the extraction of the impedance components $Z_{grid,dd}$ and $Z_{grid,qd}$. A brief idle time t_{idle} is provided to allow the transients to settle down. Typically, 1 to 3 cycles of the 50 Hz period is provided as idle time. The impedance components $Z_{grid,dq}$ and $Z_{grid,qq}$ are then acquired by applying the PRBS perturbation to the q-axis component of the control signal.

The total time of the measurement period excluding the post-processing step is approximated as (2.13), where f_{sw} is the switching and sampling frequency of the WFZ device.

$$t_{M,seq} = 3M_r \frac{2^{N_{bit}} - 1}{f_{sw}} + t_{idle} \tag{2.13}$$

The frequency resolution of the computed impedance is

$$f_{res,seq} = \frac{f_{sw}}{M_r(2^{N_{bit}} - 1)}. \tag{2.14}$$

As explained above, the different components of the dq impedance matrix are obtained at different times and thus it would be beneficial to acquire all dq impedance components simultaneously.

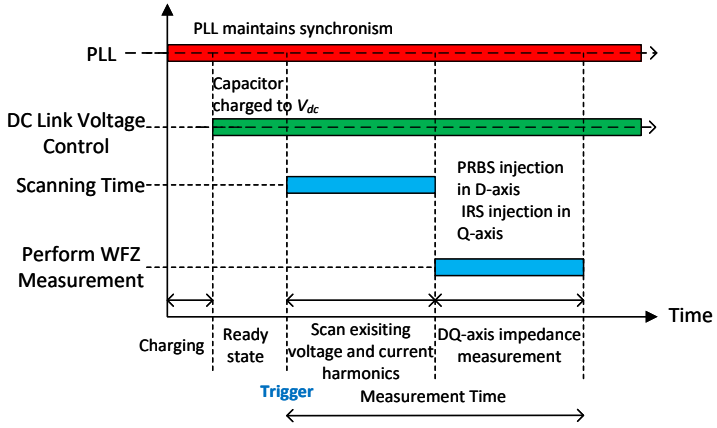

Figure 2.5: Timing diagram of parallel method

2.3.2 Parallel DQ Impedance Extraction

Fig. 2.5 shows the timing diagram for the parallel method. The startup procedure of the parallel method is same as the sequential method. The d and q-axes are simultaneously perturbed in the parallel method. To do this, a perturbation signal orthogonal to the original PRBS signal is synthesized. Consider that the length of the PRBS signal is $M_r(2^{N_{bit}}-1)$, taking into account M_r rounds and N_{bit} shift register bits. The PRBS sequence length is doubled and each alternate bit of the PRBS is flipped to produce the Inverse Repeat Sequence (IRS), which yields the orthogonal signal compared to the PRBS. The PRBS and IRS signals do not share energy at any common frequency. Hence, $2M_r(2^{N_{bit}}-1)$ is the length of the IRS and PRBS signals for the parallel method.

Scanning phase

The device goes into the scanning phase, where voltage and current samples are recorded, as soon as it is triggered to measure impedance. A total of $2M_r(2^{N_{bit}}-1)$ samples are collected during this phase.

Perturbation phase

By simultaneously perturbing the d and q-axes with PRBS and IRS, respectively, all four components of Z_{grid} are measured. (2.15) approximates the overall time required for the parallel method.

$$t_{M,par} = 4M_r \frac{2^{N_{bit}} - 1}{f_{sw}} \tag{2.15}$$

The frequency resolution of the parallel method is given by (2.16). Note that the frequency resolution in the parallel method is half that obtained in the sequential method.

$$f_{res,par} = \frac{f_{sw}}{2M_r(2^{N_{bit}} - 1)} \tag{2.16}$$

The frequency resolutions of the two approaches should be identical to ensure a fair comparison of measurement times. This is accomplished by selecting M_r in the sequential method two times M_r used in the parallel method. Thus, on the basis of frequency resolution, the additional time taken by the sequential method is

$$\Delta T = M_r \frac{2^{N_{bit}} - 1}{f_{sw}} + t_{idle}. \tag{2.17}$$

2.3.3 Sequence Impedance Extraction

Under unbalanced conditions, the impedance in the sequence domain needs to be measured. A straightforward way to determine the sequence impedance is to use symmetrical components to convert the stationary domain phasors of currents and voltages into sequence domain. Then, using (2.18) and (2.19), one can determine the positive and negative sequence impedances, where I_p, I_n, V_p, and V_n denote the positive and negative sequence phasors of currents and voltages, respectively.

$$Z_p(j\omega_i) = V_p(j\omega_i)/I_p(j\omega_i) \tag{2.18}$$

$$Z_n(j\omega_i) = V_n(j\omega_i)/I_n(j\omega_i) \tag{2.19}$$

Sequence domain impedance extraction can be performed using either the parallel or sequential method. The aforementioned mentioned approach is valid when there is no coupling between the positive and negative

sequence components, or otherwise known as Mirror Frequency Effects (MFE). When MFE are significant, the aforementioned approach is no longer suitable [68]. This work considers the definition of a modified sequence impedance in accordance with [68, 69]. This method allows the calculation of sequence impedance from *dq* impedance through a linear transformation that preserves the eigen values. This transformation is described by (2.20). As a result, in the post-processing steps, the WFZ-IM can be augmented with the computation of both *dq* impedance and modified sequence impedance.

$$Z_{pn,mod} = \begin{bmatrix} Z_{pp} & Z_{pn} \\ Z_{np} & Z_{nn} \end{bmatrix} = A_z Z_{dq} A_z^{-1} \tag{2.20}$$

where, A_z is defined by the following hermitian unitary matrix.

$$A_z = \frac{1}{\sqrt{2}} \begin{bmatrix} 1 & j \\ 1 & -j \end{bmatrix} \tag{2.21}$$

Strong coupling in the sequence domain, which could be caused by PCC dynamics or DC link voltage control dynamics, could prevent the system from being LTI. MFE is the term used to describe the strong coupling between the positive and negative sequence frequency components. The modified sequence approach can be used to extract the sequence impedance as the original sequence impedance model cannot capture MFE [68, 69]. WFZ device may therefore extract impedance in *dq* and *abc* stationary frames, and then post-process the resulting impedance to the original and modified sequence domain.

2.4 Simulation Results

2.4.1 Simulation Setup

Fig. 2.6a shows the simulation setup which consists of the grid-connected WFZ device and a passive grid impedance Z_{grid}, which represents the unknown grid impedance that needs to be measured. The parameters of the WFZ device are shown in Table 2.1. For the analysis, two types of passive impedance branches are taken into account. To test if the WFZ device can extract medium frequency resonance in the grid impedance, the impedance type 1 branch, as shown in Fig. 2.6b, which includes

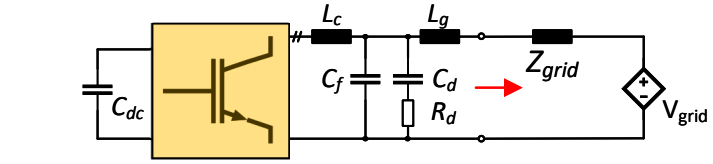

(a) WFZ Device setup

(b) Impedance type 1

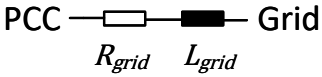

(c) Impedance type 2

Figure 2.6: Simulation setup

a parallel LC resonance is used. In Section 2.4.2, impedance type 1 is utilized. As shown in Fig. 2.6c, impedance type 2 is a series RL impedance that can be utilized for studying disturbance rejection at lower frequencies and characterizing the PRBS amplitude. Sections 2.4.3 and 2.4.4 utilize impedance type 2 branch. The switched models are developed in MATLAB/SIMULINK and simulated in with a time step of 200ns.

2.4.2 Sequential and Parallel Impedance Measurements

In this scenario, the WFZ device is configured to use the sequential method. The sampling and PRBS injection frequencies are set to the highest feasible frequency, which is the switching frequency of 20 kHz. When the device is grid connected, the DC link capacitor is charged to the nominal DC voltage and the device is in READY state. The PRBS bits utilized are $N_{bit} = 11$, and the number of rounds is $M_r = 2$. Between the d and q-axis excitation, three cycles (60 ms) of idle time (t_{idle}) is utilized. Throughout the simulation, the case 1 impedance branch, shown in Fig. 2.6b, is used. Fig. 2.7 depicts the simulation results for impedance extraction using the sequential method. The WFZ device begins the scanning phase at time $t = 0.4s$, when it is triggered to measure the impedance. The d-axis perturbation starts with PRBS amplitude $V_H = 4\%V_n$ after the scanning phase. In Section 2.4.4, the

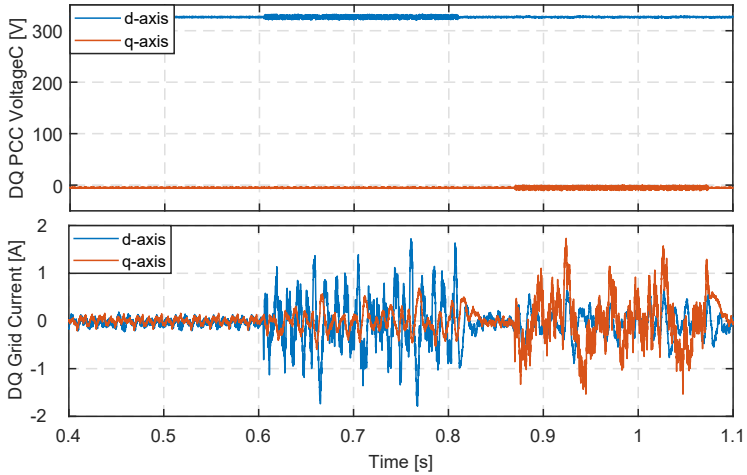

(a) dq voltage and current

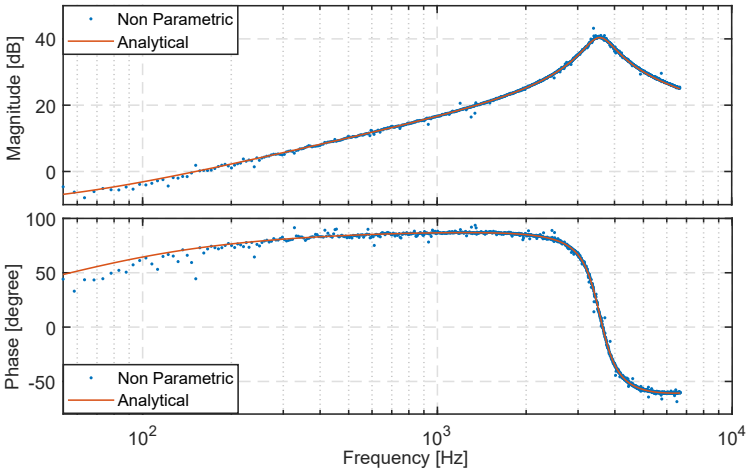

(b) Z_{dd} impedance magnitude and phase

Figure 2.7: Sequential Method: Terminal voltage and current of the WFZ device and the extracted impedance magnitude and phase

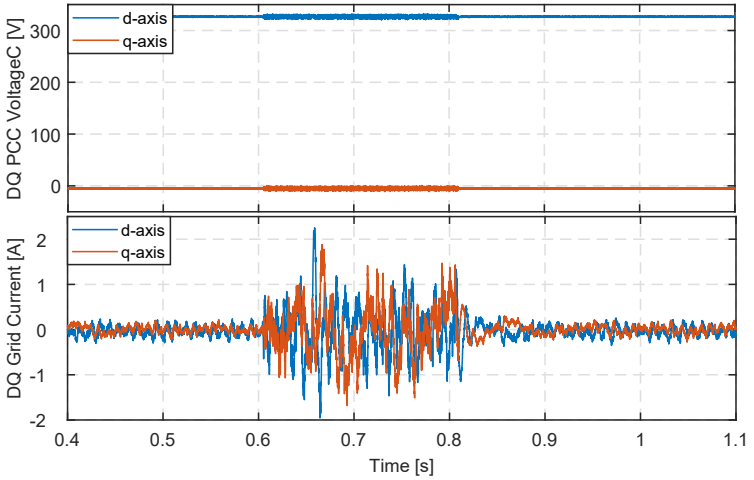

(a) dq voltage and current

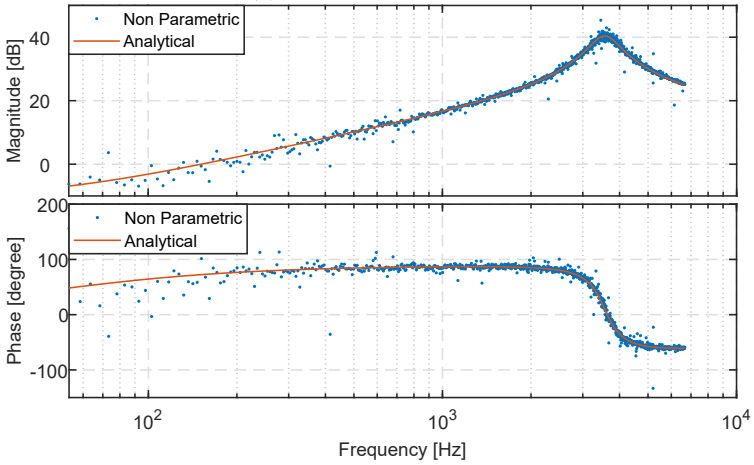

(b) Z_{dd} impedance magnitude and phase

Figure 2.8: Parallel Method: Terminal voltage and current of the WFZ device and the extracted impedance magnitude and phase

Table 2.1: WFZ device parameters

Parameters	Values
Switching frequency	20 kHz
DC link capacitor (C_{dc})	270 μF
Inverter side inductor (r_c, L_c)	0.55 Ω, 2.7 mH
Grid side inductor (r_g, L_g)	0.36 Ω, 1.8 mH
Filter capacitances (C_f, C_d)	0.5 μF, 0.5 μF
Damping resistor	300 Ω
Inner current control	$K_{p,cc}$ = 1.5e-3 , $K_{i,cc}$ = 60
Outer voltage control	$K_{p,cc}$= 0.3 , $K_{i,cc}$ = 61

selection of PRBS amplitude is explained. The *dq* current and voltage at the terminal of the WFZ device are shown in Fig. 2.7a. It is evident that the *d*-axis perturbation current only affects the *d*-axis component of PCC voltage, indicating a minimal impedance coupling between the *d* and *q*-axes. A similar observation holds when the *q*-axis is perturbed. Only Z_{dd} impedance is displayed in this work since the off-diagonal components of impedance Z_{dq} and Z_{qd} are insignificant and the diagonal components Z_{dd} and Z_{qq} are equal. The non-parametric impedance is obtained by post-processing the voltage and current samples collected throughout the course of the measurement period, which are stored in the FIFO buffer. Fig. 2.7b shows the extracted impedance magnitude and phase. It is evident that the extracted impedance agrees with the analytical model and that the resonance caused by the grid impedance is also correctly captured. With a frequency resolution of 4.88 Hz, the sequential technique takes 0.67 s in total. To decrease the estimate error due to scattering of data points, a moving average filter with a sufficient window size may be applied to the the complex data points so that a smoothed frequency response is achieved. The window size should be selected so that it only thins the data and does not cause apparent modifications to the plots.

Using the same settings as before, the measurement process is performed using the parallel technique. It should be noted that in order for the parallel technique to have the same frequency resolution as the sequential method, $M_r = 1$ is used. The simulation results from the parallel method are displayed in Fig. 2.7. The PRBS and IRS signals, respectively, simultaneously excite the *d* and *q*-axes components of the

control signal. Following the scanning phase, the injected dq currents simultaneously perturb both dq components of the voltage, as shown in Fig. 2.8a. The extracted non-parametric impedance magnitude and phase are shown in Fig. 2.8b, and the results accurately match with the analytical impedance. The parallel method has a measuring duration of 0.41 s. Comparing Figs. 2.7a and 2.8a, it can be observed that the measurement time in the parallel method is shorter than that of the sequential method, however, the accuracy of the parallel method is worse than that of the sequential method. A comparative analysis is carried out in Section 2.4.4 to further confirm the accuracy comparison between the sequential and parallel technique.

2.4.3 Impact of Control Bandwidth

Recall the control structure of the WFZ device as shown in Fig 2.3 which consists of an external DC link voltage controller that provides current references to an inner current controller (CC). Notice that the PRBS perturbation is an input disturbance to the closed loop system since it is added to the duty cycle, or the output of the CC. The extraction of grid impedance is negatively impacted at the lower frequencies because the inner CC might reject and compensate the low frequency components of the PRBS signal. In contrast to standard converter control design, which aims a high bandwidth, the control goal for the WFZ device is to keep the bandwidth low to reduce the attenuation of the low-frequency components of the PRBS.

Figure 2.9 shows how the obtained non-parametric grid impedance is impacted by the CC bandwidth. The gains corresponding to the low bandwidth of the current control is given in Table 2.1 and those of high bandwidth case are $K_{p,cc} = 1$ and $K_{i,cc} = 10$ respectively. For this investigation, impedance type-2 branch with $R_{grid} = 0.01\Omega$ and $L_{grid} = 0.3mH$ is used. As seen in Fig. 2.9, the extracted impedance at low CC bandwidth is quite accurate at all frequencies, but with large bandwidth for CC, accuracy at lower frequencies are substantially affected and the extraction is accurate only above 400 Hz. The -3dB crossover frequency of the disturbance rejection transfer function $R(s)$ must be taken into consideration when designing the current controller for the WFZ device. This crossover frequency occurs at around 8Hz in the proposed design using parameters provided in Table 2.1.

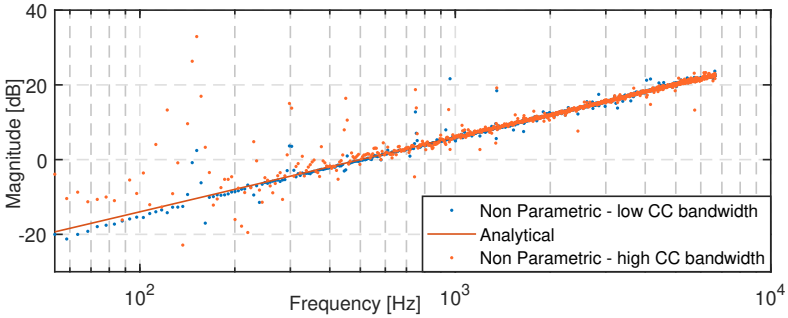

Figure 2.9: Impact of current control bandwidth on the extracted impedance magnitude

2.4.4 Impact of PRBS Amplitude

The PRBS amplitude is chosen based on the minimum impedance that must be extracted as well as the THD that occurs during the measurement time. For this analysis, a sequential method with type-2 impedance is considered. The measurements are repeated using different PRBS amplitudes. Mean absolute error (η) in the extracted impedance is computed using (2.22) where N_f is the number of frequency points, $Z_m(j\omega_i)$ is the extracted impedance and $Z_{act}(j\omega_i)$ is the analytical impedance at an arbitrary frequency ω_i.

$$\eta = \frac{1}{N_f} \sum_{i=1}^{i=N_f} \left| \frac{Z_m(j\omega_i) - Z_{act}(j\omega_i)}{Z_{act}(j\omega_i)} \right| \tag{2.22}$$

It is evident from Fig. 2.10 that, for a given impedance, the absolute error η reduces and the THD rises as the PRBS amplitude increases. Increasing PRBS amplitude over 10% of nominal grid voltage (V_n) does not result in a significant decrease in η, but increases the THD substantially. As seen in Fig. 2.10, increased accuracy (lower η) is obtained in the case of large impedance for a given PRBS amplitude. As per (2.4), the PCC voltage perturbation is directly proportional to the impedance magnitude for a given perturbation current. Thus, for a given perturbation current, a larger impedance results in a higher voltage

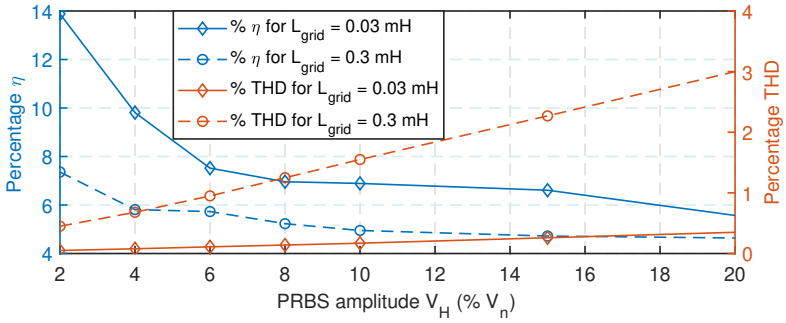

Figure 2.10: Impact of PRBS amplitude on η and THD

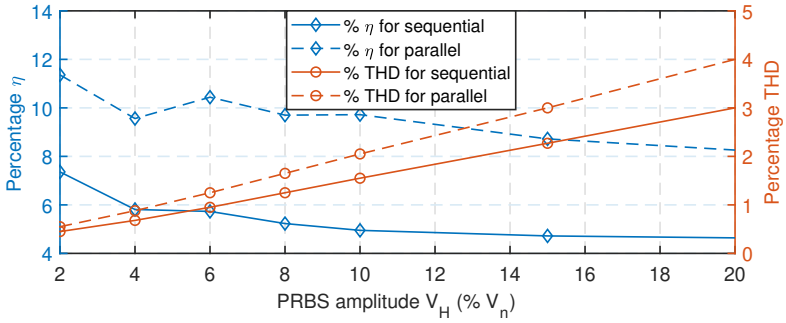

Figure 2.11: Comparison of performance of Sequential and Parallel Method

drop, which facilitates accurate measurement. The PRBS amplitude of the WFZ device needs to be fixed based on the minimum L_{grid} that needs to be measured and the mean allowable THD during measurement.

The performance comparison of the sequential and parallel methods in terms of η and mean THD is shown in Fig. 2.11. In this analysis, the grid impedance is constant ($R_{grid} = 0.01\Omega$ and $L_{grid} = 0.3$ mH), enabling only the impact of the method to be examined. In comparison to the parallel method, the sequential method has decreased η (nearly 50 % reduction) and THD for a given PRBS amplitude, as shown in Fig. 2.11. However, in terms of measurement time, the parallel method is almost 2 times faster than the sequential method for a given frequency resolution. To determine an appropriate measurement method, it is essential to consider three key factors: measurement time, mean absolute error η, and THD level. Each of these factors should be given a distinct priority.

The aforementioned simulations neither consider the uncertainties posed by the voltage/current measurement and ADCs, nor consider the potential influence of parasitic passive components that may be involved. In Section 2.5, experimental hardware evaluation is carried out to further validate the proposed method.

2.5 Experimental Results

2.5.1 Experimental Setup

A picture of the constructed and commisioned low voltage prototype of the WFZ device is shown in Fig. 2.12. Table 2.1 shows the parameters used to produce a low voltage prototype of a WFZ device. The device has a switching and sampling frequency of 20 kHz. The schematic of the simulation setup depicted in Fig. 2.6 is similar to the picture of the experimental setup displayed in Fig. 2.13. The experimental setup as shown in Fig. 2.13 consists of the WFZ device, a Chroma 618300 grid emulator and a re-configurable passive RLC load rack. The WFZ device is connected to the grid emulator though the load rack- The LCL filter boards and analog measurement voltage/current boards are designed modular to optimize the size and reliability of the WFZ device. The analog voltage and current measurement boards are calibrated to have the same frequency response, and the output stage includes an 8th order low pass filter with an adjustable cut-off filter. The software component

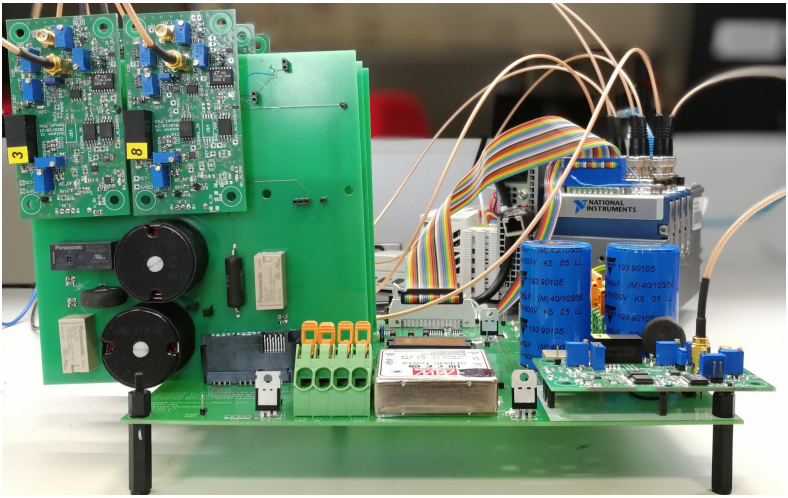

Figure 2.12: WFZ device prototype

of the device, as depicted in Fig. 2.1, is implemented using a National Instruments Compact Rio cRIO-9024 hosting a Virtex 5 FPGA. The cRIO-9024 utilizes the National Instruments NI-9215 and NI-9401 to enable high rate analog data acquisition up to 100kS/s and to enable high speed PWM respectively. A passive RLC load rack connects the WFZ device to a Chroma 61830 grid emulator, as seen in Fig. 2.13. As seen in Fig. 2.6b, the load rack is composed of a parallel RLC circuit with nominal parameters. The cRIO-9024 is directly controlled by a host PC to control the relays and other control functions such as PRBS trigger, and additionally to enable real-time monitoring of voltage and current waveforms.

2.5.2 Grid Connected Impedance Measurements

The grid emulator operates at a voltage of 40V RMS, with the DC link voltage adjusted to 130V via a DC power source. Experimental results pertaining to the parallel method is discussed in this section, and the impedance data from the parallel method is also used to evaluate the

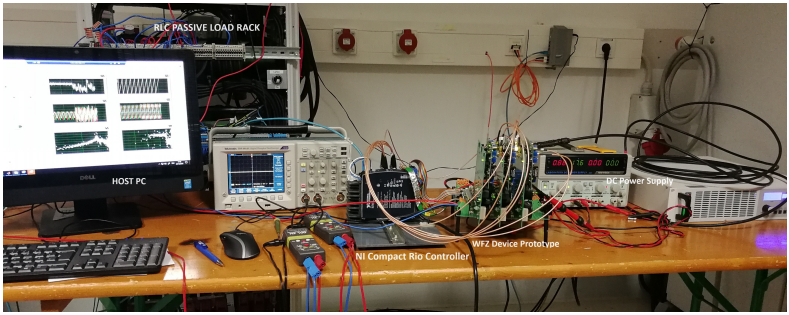

Figure 2.13: Experimental setup

uncertainty analysis proposed in Section 2.6. As previously mentioned in Section 2.4.4, the parallel method obtains shorter periods and thus it is required to experimentally measure the accuracy for the parallel method. The parallel approach with parameters $M_r = 1$ and $N_{bit} = 11$ is used, resulting in 4094 sample points in each of the scanning and perturbation phases. The total measurement duration and frequency resolution are 0.4094s and 2.4426 Hz, respectively. When the WFZ device is triggered, it moves into the scanning phase, which is followed by the above-discussed perturbation for the predetermined number of sample points. While the PRBS perturbation magnitude was adjusted throughout the experimental assessment, a PRBS perturbation of 10% of V_n is chosen for the experimental results shown in Fig. 2.14 based on the findings from Fig. 2.11. The injected perturbation current and PCC voltage are shown in Figs. 2.14a and 2.14c, respectively. Figures 2.14b and 2.14d depict the DC link voltage and PLL angle, respectively. Since the DC link is connected to a DC power source for the tests conducted in this work, the WFZ device can only be used with a current controller. In the stand-alone WFZ implementation, the external DC link voltage control is significantly slow and has no effect on the behavior at high frequencies. As previously indicated, only the inner current controller enables disturbance rejection at lower frequencies, therefore the experimental setup remains appropriate for extracting and characterizing the resultant impedance.

The non-parametric impedance in the positive sequence is retrieved by using the measured voltages and currents. Using the Venables 350c

frequency analyzer, a reference impedance is determined in order to compare the experimentally extracted impedance. The frequency analyzer is used to measure the grid impedance to generate the reference impedance. The comparison of the reference measurement and the experimentally acquired impedance magnitude and phase is presented in Fig. 2.14e. A moving average filter with a window size of 15 is applied to thin the data points because of a scattering that was observed in the experimentally derived impedance. The moving averaged impedance efficiently eliminates the scattered points without appearing to alter the magnitude or phase graphs, as seen in Fig. 2.14e. Considering both magnitude and phase, the impedance measurement device exhibits better accuracy in the 0.3 to 4.5 kHz range when compared to other frequency points, as seen in Fig. 2.14e.

Since f_{sw} is the switching and sampling frequency of the WFZ, the theoretical measurement limit is the Nyquist frequency $\frac{f_{sw}}{2}$. However, close to Nyquist frequency, the accuracy is severely impacted. As can be seen in Section 2.4, accurate measurements can be made up to approximately $\frac{f_{sw}}{3}$ from a noiseless measurement process and sampling standpoint. In practice, noise and uncertainty are introduced by the voltage and current measurements. Moreover, the LCL filter of the WFZ device has a cut-off frequency of 4.8 kHz, which filters higher components of the perturbed currents. Figure 2.14e shows how impedance measurements become less accurate around resonance frequency and beyond.

2.6 Uncertainty Characterization

This section proposes two characterization methods for wideband impedance measurement devices: Wideband characterization and per-frequency characterization

2.6.1 Wideband Characterization

The wideband grid impedance is a set of complex values specified over a frequency grid. Firstly, a known passive network impedance is measured using a highly accurate frequency analyzer. This impedance measurement represents the ground truth or actual measurement $Z_{act}(j\omega_i)$. The impedance data points from the WFZ device $Z_m(j\omega_i)$ can compared with

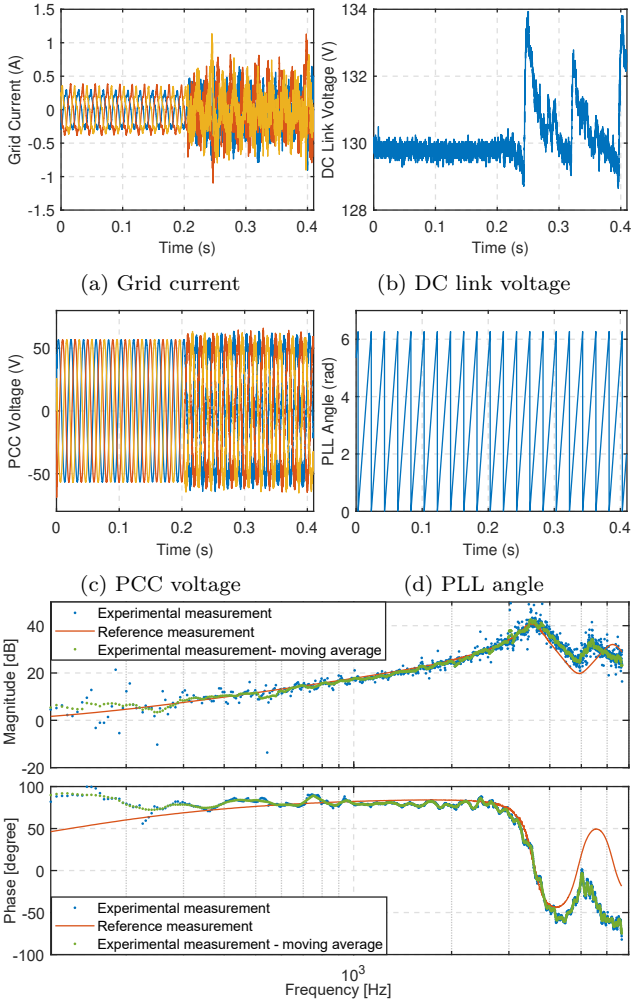

(a) Grid current (b) DC link voltage

(c) PCC voltage (d) PLL angle

(e) Impedance magnitude and phase comparison

Figure 2.14: Experimental Result

the actual impedance $Z_{act}(j\omega_i)$ to compute the mean absolute error η defined in (2.22). In (2.22), N_f denotes the number of points in the frequency grid. The parameter η measures the overall accuracy of the WFZ device, wherein $\eta = 0$ indicates an ideal measurement equipment with no errors. Using a constant PRBS amplitude $V_H = 10\%V_n$, 100 trials are performed, and the η for each case is presented in Fig. 2.15a. Figure 2.15a shows that the majority of the estimated η values are near to the mean, indicating repeatability. From the aforementioned set of experiments, the mean $E[\eta]$ and standard deviation σ are, respectively, 0.317 and 0.0261. The normalized probability distribution of η is shown along with $E[\eta]$ and 3σ standard deviation in Fig. 2.15b and only 2 experimental data points lie outside this bound. The experimental results shown in Fig. 2.14 are related to experiment number 28 of Fig. 2.15a, which represents the nominal case where η is close to the mean.

2.6.2 Per-frequency Characterization

To achieve a frequency-dependent accuracy, it would be advantageous to quantify the accuracy at each frequency point. Let us define the absolute error per frequency point as per (2.23).

$$\eta_{f,i} = \left| \frac{Z_m(j\omega_i) - Z_{act}(j\omega_i)}{Z_{act}(j\omega_i)} \right| \tag{2.23}$$

For each frequency point i, the mean value of $\eta_{f,i}$ is calculated across all experimental trials. The mean absolute error at each frequency is shown in Fig. 2.16a. The enlarged part of Fig. 2.16a shows that the device operates with a mean error less than 0.3. Around the resonance frequency of the grid impedance, the mean error increases around 2.5 kHz followed by a decrement. This study does not take into account the impact of the grid emulator. The grid emulator is not an ideal or stiff voltage source as they are band limited and they have a characteristic closed-loop output impedance at higher frequencies.

The measured impedance magnitude and phase uncertainty are shown in Fig. 2.16b. At each frequency point, taking into account all of the experimental trials, the mean and standard deviation of magnitude and phase are calculated. The mean of the impedance magnitude and phase, as shown in Fig. 2.16b, closely matches the reference measurement over the observed frequency range; nevertheless, the standard deviation rises

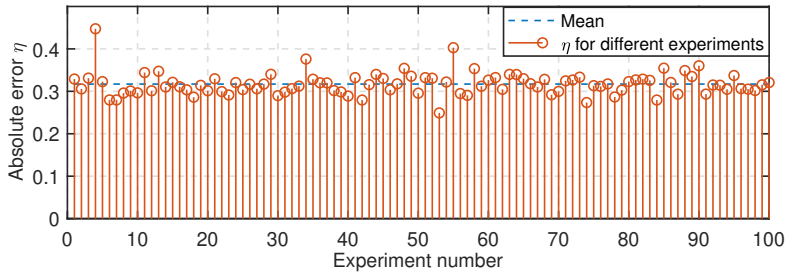

(a) Relative error η obtained for each experiment

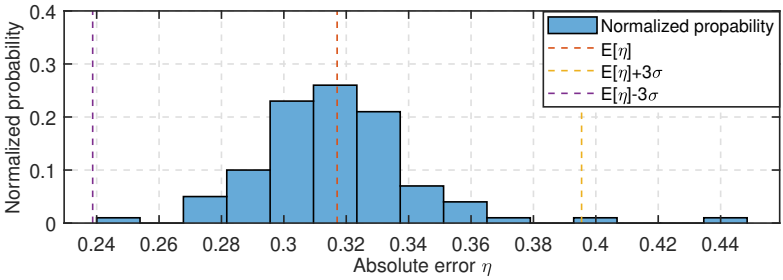

(b) Normalized probability of absolute error η

Figure 2.15: Wideband characterization of WFZ device

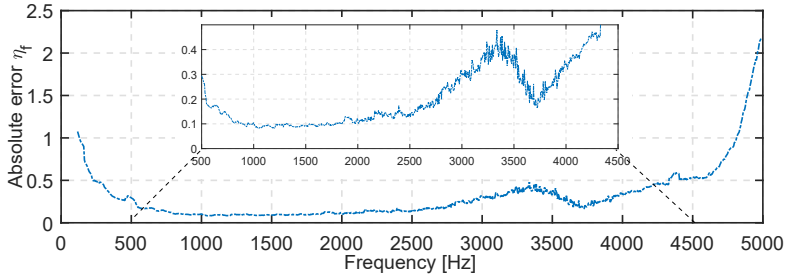

(a) Absolute error dependency on frequency

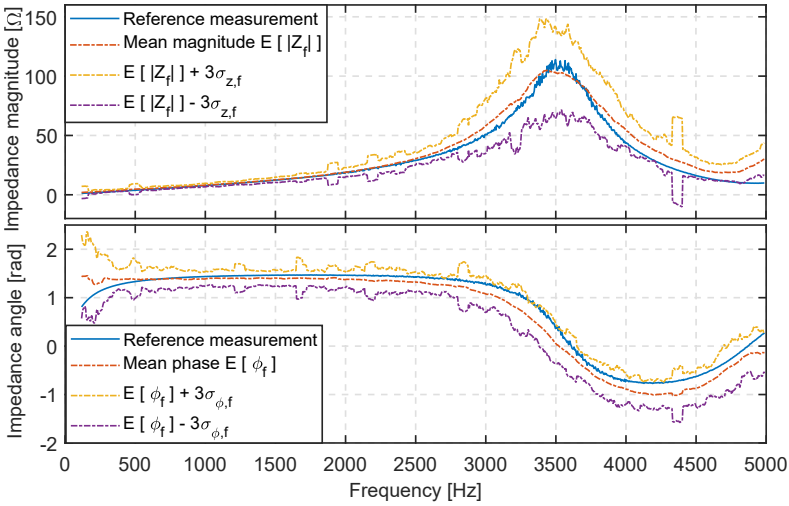

(b) Uncertainty in measured impedance magnitude and phase

Figure 2.16: Per-frequency characterization of WFZ device

around the resonance frequency of the passive impedance branch. As seen in Fig. 2.16b, per-frequency characterization makes it possible to compute the confidence interval as a function of frequency, which may find use in non-parametric impedance based monitoring. Per-frequency characterization also makes it possible to identify the frequency ranges in which the performance of the WFZ device has to be enhanced.

2.7 Summary

This work describes a standalone WFZ device that can measure non-parametric grid impedance under steady-state conditions without requiring grid interruption. Operational sequences for the WFZ device are proposed and also the uncertainty characterization methods for determining the accuracy of such wideband impedance measuring devices are discussed.

To enable the WFZ device for *dq* impedance extraction, two operational sequences are proposed: sequential and parallel. Considering the same frequency resolution, the parallel method is almost twice as fast as the sequential method. In terms of accuracy and THD, for a given amplitude of perturbation, the sequential method on an average provides around 50% reduction in the mean absolute error and lower THD levels than the parallel method, showing higher accuracy. The requirements of PRBS amplitude in relation to the minimum impedance magnitude to be measured are also studied in this research. The choice of the PRBS amplitude is a trade-off between absolute error and THD needs since larger impedances may be extracted with lower absolute error and higher THD levels for a given PRBS amplitude.

A low voltage prototype of the WFZ device is built, and the extraction of impedance is experimentally demonstrated. Two techniques for characterizing wideband impedance measurement devices are presented in this work. Wideband characterization determines the overall accuracy of the device, whereas per-frequency characterization calculates uncertainty at each frequency. With a standard deviation of 0.026 and a mean absolute error of 0.317, the proposed device performs effectively over a wide range of frequencies. Increasing the resolution of the voltage and current measuring boards can enhance the overall performance of the device.

This work considers only the measurement of passive impedances. To measure impedances of grid with many power electronic converters which

exhibit non-linear behavior, the WFZ device based measurements could be extended to calculate the frequency coupling matrix (FCM) which can capture the coupling among various frequency components, which is covered in Chapter 3.

3

Frequency Coupling Matrix Measurement

3.1 Introduction

3.1.1 Motivation

Integration of RES such as wind and solar PV with the power grid is achieved through the use of power-electronic converters. Frequency coupling effects occur due to the inherent switching behavior of power converters and additionally the nonlinearities introduced by the control system and PLL introduce frequency coupling behavior [21, 34]. The DC side exhibits considerable dynamics due to the volatile nature of renewable sources, and furthermore, commonly, renewable sources are interfaced with the DC link through a DC/DC converter. The DC side dynamics propagate to the AC side directly due to the switching action and also due to the presence of DC side power or voltage controller, which passes reference current to the AC side current controller. Furthermore, in modern power grids, there is a considerable growth in power electronic loads such as Variable-Frequency Drive (VFD)s and other rectifier-driven loads, which create non-linear distortions [70]. Numerous cases of harmonic pollution and harmonic resonance phenomena have been reported in grids with a substantial proliferation of power electronic converters [20]. As a result, nonlinear modeling of power converters is critical for understanding overall system behavior and stability.

To some degree, small-signal behavior may be predicted and explained using Linear-Time Invariant (LTI) modelling techniques based on state-space or transfer function [21, 55]. Nevertheless, the frequency coupling non-linear effects in power converters are not captured by these models, and LTI models are unable to predict the occurring instabilities.

Modelling in both the time and frequency domains is possible using the LTP technique. Unlike LTI models, LTP models account for frequency coupling effects and are better able to capture harmonic amplification [34, 35]. The harmonic impedance model that takes frequency coupling into account may be derived using the LTP technique [35]. The HSS approach offers an additional means of representing the LTP model. In this approach, the harmonics of the state variables are regarded as states and augmented to the model [36]. In a similar vein, time and frequency domain methods may be used to represent the FCM. The product of a state variable and a switching function is expressed in the frequency domain as an infinite discrete convolution sum, necessitating truncation [25, 37]. On the other hand, piece-wise linear differential equations may be solved to fully represent the FCM in the time domain [37]. The above mentioned approaches which either adopt time or frequency domain analysis are useful to formulate analytical or parametric models of power converters.

Nonlinear parametric models of power converters can be derived using the models previously discussed and these approaches typically require converter, filter, and control parameters as well as the control structure must be specified for these models. The models of commercially available power electronic converters cannot be obtained using these modelling techniques as the design and control parameters for hardware are frequently protected by IPR. When an empirical or measurement based approach is required by the grid operator to investigate harmonic interactions in a interconnected system, the non-parametric model of the converter is a valid solution.

The linear non-parametric models are straightforward, however they cannot model frequency coupling effects. With the disadvantage of requiring a large quantity of measurement data, advanced techniques such as Non-linear Poly-Harmonic Distortion (NPHD) modeling allow for the empirical modeling of higher order non-linear effects [71]. Higher order harmonics are ignored by the FCM, which only captures first order frequency coupling. Compared to the NPHD technique, this results in a comparatively simpler model that requires less experimental data for model extraction. Thus, between the two extremes of non-parametric modeling, FCM is a trade-off.

3.1.2 State-of-the-art

The various methods of extracting the FCM of power converters is discussed here. In [38], the FCM of power electronic converter acting as a non-linear load was extracted by means of an experimental method. In this setup, each harmonic is applied successively through a power amplifier [38]. This measurement setup can be used to extract FCM of power electronic converters under laboratory conditions, however, the setup is inadequate for in-field measurements. The FCM is derived by applying each harmonic one after the other. Again, a sequential perturbation-based technique is utilized [39]. Power converter FCM measurement might be accomplished by using a harmonic voltage source, such as a grid emulator. Since the necessary voltage perturbations are generated directly using a grid emulator, the experimental setup described in [38, 39] may be utilized to extract the FCM of the power electronic converter in a laboratory setting. For the following reason, nevertheless, the actual usage of such setups is restricted due to the following reasons:

- Using a voltage source based excitation such as a grid emulator cannot be used in the field, since the power-electronic converter in field is connected to the utility grid which is not a controlled source of harmonic excitation

- Modern grid-connected power converters operate in several modes and may change their control settings according to the operating environment. Because of this, it is not practical to extract every possible FCM in laboratory settings due to the large quantity of data that has to be stored

Due to the reasons mentioned above, a measurement setup that is applicable both in the laboratory and field condition is required. This work proposes a measurement setup that can be used in the field and in the laboratory.

In [40], an empirical approach is proposed to extract the FCM of a VFD by sequentially exciting each harmonic. These approaches may be valid for electrical drive applications; however, the use of wideband excitation signals is beneficial for grid-connected converter applications because the FCM can be extracted through a least squares problem [41]. Furthermore, such a formulation enables recursive updates to the FCM [41] with each new wideband measurement. The FCM approach enables system-level

modeling by aggregating multiple local subsystems modelled as FCMs to form a global system-level FCM [41]. [41] proposes an empirical approach to extracting the global FCM from network harmonic measurements. In [41], an empirical approach is proposed to extract global FCM from network harmonic measurements. To extract the FCM, a least-squares approach can be used while taking harmonic perturbations at multiple frequencies into account.

3.1.3 Main Contribution

This work proposes a wideband excitation-based FCM measurement method for power electronic converters. The wideband perturbation current source employed in the proposed method is connected in parallel with the grid-connected DUT. This study uses a WFZ measurement device to create a wideband perturbation current source [32, 33]. Wideband perturbed currents can be generated by modulating the duty cycle of the WFZ device using a PRBS signal or a sum of sinusoids. The linear impedances of DUT were previously extracted utilizing wideband excitation techniques [28–30, 33]. The proposed method involves numerous repetitions of these wideband perturbation currents applied at the PCC of the DUT, during which the DUT's terminal voltage and current are recorded. Through the repetitive measurements, a substantial number of voltage and current spectrum are retrieved. The goal is to determine the FCM that closely fits the extracted voltage and current spectrum. Through a least-square formulation, the FCM of the converter is extracted. Furthermore, the equivalent FCM of the grid and DUT impedance can be calculated by monitoring the injected WFZ current. The equivalent FCM allows for the direct monitoring of potential frequency points that may create harmonic resonances between the grid and the DUT. Rather than utilizing the PRBS as the perturbation signal which typically leads to a requirement of large number of measurements owing to the high frequency resolution, this work proposes using the sum of sinusoids. The sum of sinusoids only covers a set of frequencies that is defined, the number of measurements required has been significantly reduced. Meta-heuristic algorithms can optimize the phase of each sinusoid to reduce the peak-to-peak amplitude of the perturbation signal [72]. Importantly, by selecting the appropriate perturbation amplitude, the THD of the PCC voltage can be preserved

within grid code specification. This work also discusses the minimum number of measurements required to accurately extract the FCM.

To assess the correctness of the extracted FCM and to interpret it, this work proposes characterization parameters for the FCM. By calculating the diagonal dominance of the FCM, the degree of non-linearity can be assessed. Furthermore, the extracted FCM is validated by means of an experimental method. The characterization of the extracted FCM is carried out through empirical measurements by applying test perturbations to the power-electronic converter. By comparing the predicted voltage / current spectrum calculated from extracted FCM model and the measured spectrum from experiments, the accuracy of the FCM is characterized through mean absolute error calculations.

The contributions to this chapter are summarized as follows:

- Empirical FCM measurement method for power electronic converters using wideband excitation signals.
- FCM characterization method
- Validation of the proposed approach with laboratory experiments and simulation use-cases

The proposed method allows for the creation of black box FCM models and the extraction of FCM from commercially available power electronic converters. The proposed approach could potentially be included into simulation tools to generate non-parametric power converter FCM models.

3.2 WFZ Device-Based FCM Extraction Method

FCM model considers first order coupling terms between two different frequencies of current and voltage unlike its linear counterpart which considers only diagonal one-one coupling. The coupling admittance/impedance matrix includes off-diagonal elements and the degree of linearity can be assessed through the diagonal dominance of the coupling matrix. The FCM that links the different frequency components of the current and voltage of the DUT can be expressed as (3.1), where $\boldsymbol{i} = \begin{bmatrix} i_{j\omega_1} & \dots & i_{j\omega_h} \end{bmatrix}^T$ and $\boldsymbol{v} = \begin{bmatrix} v_{j\omega_1} & \dots & v_{j\omega_h} \end{bmatrix}^T$.

$$\boldsymbol{v} = \begin{bmatrix} z_{11} & \dots & z_{1k} \\ \vdots & \ddots & \vdots \\ z_{h1} & \dots & z_{hh} \end{bmatrix} \boldsymbol{i} \tag{3.1}$$

Higher order coupling non-linearities, including products $(i(j\omega_1)i(j\omega_3))$, higher powers $(i(j\omega_1)^2)$, and combinations $(i(j\omega_1)^2 i(j\omega_3)^3)$, are disregarded in (3.1). To represent non-linearities of a higher order, X-parameters and NPHD modeling techniques may be utilized [71]. Assuming the higher order non-linearities are negligible, the FCM is capable of modeling the DUT with high accuracy.

3.2.1 Generalized FCM Model of Three Phase Power Converter

As shown in Fig. 3.1, the DUT is a generic three-phase power electronic converter for which the FCM needs to be empirically extracted. The spectrum of the terminal voltages is denoted by $\boldsymbol{v}_{a,f}$, $\boldsymbol{v}_{b,f}$, and $\boldsymbol{v}_{c,f}$, whereas the spectrum of the current drawn by the DUT is represented by the symbols $\boldsymbol{i}_{a,f}$, $\boldsymbol{i}_{b,f}$, and $\boldsymbol{i}_{c,f}$ respectively. By considering the frequency spectrum vectors of DC side voltage $\boldsymbol{v}_{dc,f}$ and current $\boldsymbol{i}_{dc,f}$, integration of DC link dynamics is possible. Considering h number of frequency points, each of the voltage and current vectors are of dimension $h \times 1$. Equation (3.2) represents the generalized FCM model of a power electronic converter.

$$\begin{bmatrix} \boldsymbol{v_{a,f}} \\ \boldsymbol{v_{b,f}} \\ \boldsymbol{v_{c,f}} \\ \boldsymbol{v_{dc,f}} \end{bmatrix} = \begin{bmatrix} \boldsymbol{F_{a,a}} & \boldsymbol{F_{a,b}} & \boldsymbol{F_{a,c}} & \boldsymbol{F_{a,dc}} \\ \boldsymbol{F_{b,a}} & \boldsymbol{F_{b,b}} & \boldsymbol{F_{b,c}} & \boldsymbol{F_{b,dc}} \\ \boldsymbol{F_{c,a}} & \boldsymbol{F_{c,b}} & \boldsymbol{F_{c,c}} & \boldsymbol{F_{c,dc}} \\ \boldsymbol{F_{dc,a}} & \boldsymbol{F_{dc,b}} & \boldsymbol{F_{dc,c}} & \boldsymbol{F_{dc,dc}} \end{bmatrix} \begin{bmatrix} \boldsymbol{i_{a,f}} \\ \boldsymbol{i_{b,f}} \\ \boldsymbol{i_{c,f}} \\ \boldsymbol{i_{dc,f}} \end{bmatrix} \tag{3.2}$$

To represent (3.2) in shorthand, the notation $\boldsymbol{v} = \boldsymbol{F_{dut}}\boldsymbol{i}$ is used, in which $\boldsymbol{F_{dut}}$ represents the FCM of the DUT. The dimensions of both $\boldsymbol{i}$ and $\boldsymbol{v}$ are $q \times 1$, where $q = 4h$. $\boldsymbol{F_{dut}}$ is a block matrix of dimension $q \times q$ containing sub-matrices, each with dimension $h \times h$. For example, $\boldsymbol{F_{a,dc}}$ is the sub-FCM that links the DC link current harmonics with the voltage harmonics in phase a and $\boldsymbol{F_{a,a}}$ is the sub-FCM that links the current harmonics in phase a with the voltage harmonics in phase a.

Considering a three phase converter with stiff DC link voltage, the dynamics that propagate between the AC and DC sides are negligible

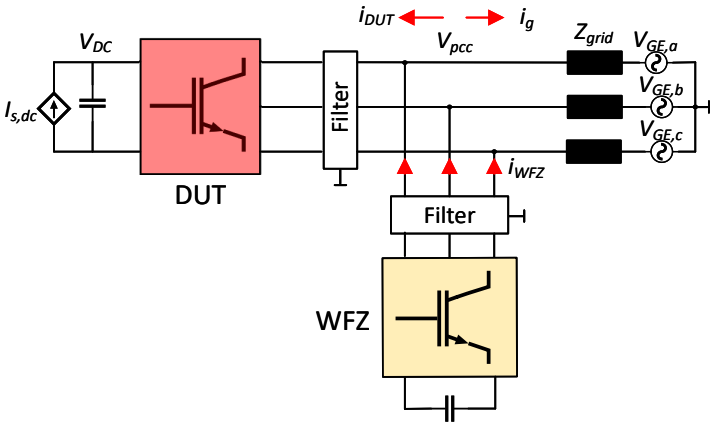

Figure 3.1: Proposed measurement setup

and hence the sub-FCM matrices such as $\boldsymbol{F_{a,dc}}$ and also the DC side relevant sub-FCM matrix $\boldsymbol{F_{dc,dc}}$ can be ignored. Further, the FCM for each phase can be extracted independently assuming balanced condition and ignoring coupling among phases. Thus for an arbitrary phase p, the generalized equation reduces to $\boldsymbol{v_{p,f}} = \boldsymbol{F_{p,p}} \boldsymbol{i_{p,f}}$. As mentioned earlier, this assumption is valid when a power converter is operated in inverter mode with a stiff DC link power supply. However, if the DC side of the inverter is interfaced to the source through a DC/DC converter such as in PV and wind applications, then DC link dynamics cannot be ignored. Additionally, in rectifier mode, the DC link dynamics are significant and thus in such cases, the generalized FCM needs to be considered.

3.2.2 Proposed Measurement Setup

The measurement setup as shown in Fig. 3.1 is considered to measure the impedance of a grid-connected DUT. Under steady state conditions, a WFZ device is proposed to extract the impedance of grid-connected DUTs in a minimally invasive manner [32, 33]. The WFZ device and the DUT are connected in parallel. Under normal steady state conditions, the WFZ device first scans the PCC voltage and DUT current. It is possible

to superimpose a wideband perturbation signal, such as the PRBS or a sum of sinusoids, on the duty cycle of the WFZ device, causing the WFZ device to inject perturbation currents into the PCC. The observed perturbation voltage in the PCC is caused by the WFZ device injected perturbation currents. Note that the grid emulator is prevented from serving as a sink for harmonics within its control bandwidth by the use of a known impedance Z_{grid} between the grid emulator and the PCC. The extraction of the non-parametric impedance can be achieved by comparing the voltage spectrum prior to and during noise injection.

$$Z_{DUT}(j\omega_i) = \frac{v_{DUT,pert}(j\omega_i) - v_{DUT,scan}(j\omega_i)}{i_{pcc,pert}(j\omega_i) - i_{pcc,scan}(j\omega_i)} \tag{3.3}$$

In (3.3), $i_{DUT,pert}$ and $i_{DUT,scan}$ represent the current spectrum drawn by the DUT during perturbation and scanning phases respectively, while $v_{pcc,pert}$ and $v_{pcc,scan}$ denote the spectrum of PCC voltage during those phases. The corresponding voltage and current spectrum are computed by calculating the FFT of the voltage and current samples recorded during the scanning and perturbation phases. When dealing with DUTs that are linear passive or active components, the impedance extraction process is accurate. However, in cases where the DUT exhibits strong non-linear behavior, accurately exciting the linear or diagonal components of the admittance becomes challenging due to cross-coupling among different frequencies. Thus, by simultaneously exciting all frequencies, it is not possible to accurately extract the impedance with one round of measurement. In fact, many rounds of measurements are required so that a least square problem can be formulated and the FCM that closely fits the acquired measurement data can be extracted. This methodology is explained in the subsequent section. Through the proposed procedure, not only the linear or diagonal component of the impedance is extracted but also the off-diagonal (non-linear) components are also extracted. Furthermore, since the proposed measurement setup consists of a parallel connected measurement device, the method is not only applicable to laboratory usage but also to field application.

3.2.3 FCM Measurement

The measurement setup depicted in Fig. 3.1 is proposed to extract the FCM of the converter. The WFZ device injects a perturbation current

during each measurement round and since the WFZ device primarily scans the PCC voltage and DUT current prior to perturbation, the difference in the spectrum during the perturbation and scanning phase is calculated for all voltages and currents. Each of these voltage and current measurement vector pairs are $\boldsymbol{v_1}$ and $\boldsymbol{i_1}$ respectively. With one measurement round, there is only a single measurement vector of dimension q but the FCM has q^2 unknowns. To determine the unknown FCM of the DUT $\boldsymbol{F_{dut}}$, it is required to collect many such measurement vectors to pose an over-determined problem. Let us consider z such measurements, where $z > q$, let us define the matrices for the difference spectrum of current and voltage as follows:

$$\boldsymbol{I_t} = \begin{bmatrix} \boldsymbol{i_1} & \boldsymbol{i_2} & \dots & \boldsymbol{i_z} \end{bmatrix}$$

$$\boldsymbol{V_t} = \begin{bmatrix} \boldsymbol{v_1} & \boldsymbol{v_2} & \dots & \boldsymbol{v_z} \end{bmatrix}$$

Thus, we have an over-determined problem as shown in (3.4).

$$\boldsymbol{V_t} = \boldsymbol{F_{dut}} \boldsymbol{I_t}. \tag{3.4}$$

A least-square minimisation problem is formulated to extract the FCM by defining the objective function (3.5), where $||\cdot||_{\mathcal{F}}$ represents the Frobenius norm, such that

$$\min_{\boldsymbol{F_{dut}}} \quad ||\boldsymbol{V_t} - \boldsymbol{F_{dut}} \boldsymbol{I_t}||_{\mathcal{F}}^2 \tag{3.5}$$

As per the identity $||A||_F^2 = Tr(AA^H)$, the above equation can be expressed through the trace operator (Tr) and A^H represents the Hermitian of A.

$$||\boldsymbol{V_t} - \boldsymbol{F_{dut}} \boldsymbol{I_t}||_{\mathcal{F}}^2 = Tr\Big\{ (\boldsymbol{V_t} - \boldsymbol{F_{dut}} \boldsymbol{I_t}) (\boldsymbol{V_t} - \boldsymbol{F_{dut}} \boldsymbol{I_t})^H \Big\}$$

The derivative of the above function w.r.t $\boldsymbol{F_{dut}}$ leads to the following:

$$\frac{\partial}{\partial \boldsymbol{F_{dut}}} ||\boldsymbol{V_t} - \boldsymbol{F_{dut}} \boldsymbol{I_t}||_{\mathcal{F}}^2 = -2\boldsymbol{V_t} \boldsymbol{I_t}^H - 2\boldsymbol{F_{dut}} \boldsymbol{I_t} \boldsymbol{I_t}^H$$

To minimise the objective function, set the derivative to 0 and thence the FCM is obtained as (3.6).

$$\boldsymbol{F_{dut}} = \boldsymbol{V_t} \boldsymbol{I_t}^H \Big(\boldsymbol{I_t} \boldsymbol{I_t}^H \Big)^{-1} \tag{3.6}$$

As the number of measurements z increases, the accuracy of the extracted FCM would improve. Section 3.4.2 studies the influence of z on the accuracy of the extracted FCM.

Remark 1: If $\boldsymbol{I_t}$ is formed with WFZ current instead of DUT current, then the equivalent FCM of the DUT and the grid impedance is obtained. This would be analogous to the Thevenin equivalent concept which are only applicable for linear networks. By using Kirchoff's Current Law (KCL) which is applicable to both linear and non-linear networks, the WFZ injected current can be expressed as (3.7).

$$\boldsymbol{i_{wfz} = i_{grid} + i_{dut} = (F_{grid}^{-1} + F_{dut}^{-1})v_{pcc}} \tag{3.7}$$

The inverse relationship to express in units of impedance can be simplified with matrix identities as given by (3.8).

$$\boldsymbol{v_{pcc} = (F_{grid}^{-1} + F_{dut}^{-1})^{-1} i_{wfz} = \left\{F_{grid}(F_{grid} + F_{dut})^{-1} F_{dut}\right\} i_{wfz}} \tag{3.8}$$

Notice that (3.7) and (3.8) are analogous to the linear network principles except that frequency coupling is considered. Potential harmonic resonant frequencies can be directly observed from the equivalent FCM as shown in Section 3.4.3.

Remark 2: The FCM represents a coupling map between input and output frequency vector. Since the FCM is derived from measurements, a reverse mapping can also be derived with the same level of accuracy i.e. to consider $\boldsymbol{I_t = F_{dut,v} V_t}$ instead of $\boldsymbol{V_t = F_{dut,i} I_t}$, where, (3.6) needs to be modified by interchanging the current and voltage matrices appropriately.

3.2.4 Wideband Perturbation Signal Design

The wideband perturbation signal might be realized as a sum of sinusoids at specific frequencies, or it could be a PRBS signal, as was previously used in [29, 33]. As the PRBS signal creates a large number of injected frequencies, the FCM is enormous in size and requires a correspondingly high number of measurements. In this study, the perturbation signal of the form (3.9) is represented by a sum of sinusoids to minimize the number of measurements that are needed. The constant amplitude is denoted by A_{pert} at all injection frequencies, and the phase is represented by ϕ_k at each frequency. The balanced perturbation signal is represented by (3.9),

where p denotes the electrical phase and can take the values 0, -1, and 1 for phases A, B, and C, respectively.

$$v_{pert,p}(t) = A_{pert} \sum_{k=1}^{h} sin(k\omega_o t + \phi_k + p2\pi/3) \tag{3.9}$$

The sum of sinusoids could have undesirable peaks if the phases ϕ_k at each frequency k are not carefully chosen, in contrast to the PRBS signal, which has a set peak amplitude as it is digital. The function to be optimized is the peak-peal amplitude of the perturbation signal $Max(v_{pert,p}(t)) - Min(v_{pert,p}(t))$. An offline optimization utilizing meta-heuristic methods, such as Particle Swarm Optimisation (PSO) or Genetic Algorithm (GA), can be used to minimize the peak-to-peak amplitude of the signal $v_{pert,p}(t)$. The techniques mentioned above can solve a h-dimensional search problem as there are h number of phases to be determined. This work uses an algorithm known as Differential Evolution (DE) [72] to solve the optimization offline and acquire the phase values ϕ_k that will be employed in experiments and simulations. The disturbance amplitude A_{pert} is randomly altered within a predetermined range, i.e., $A_{pert,min} < A_{pert} < A_{pert,max}$, during each measurement round. Prior to down-scaling with a factor of $V_{dc}/2$, the signal $v_{pert,p}(t)$ is superimposed over the controller output signal to be expressed as a duty cycle. As such, $v_{pert,p}(t)$ is stated in terms of voltage, and A_{pert}, the amplitude, is expressed as a percentage of V_n, the nominal grid voltage. A_{pert} can be selected arbitrarily high as desired under laboratory test circumstances. Nonetheless, the THD of the PCC voltage must be maintained within bounds in the field. In this case, it is best to gradually increase A_{pert} to determine the range of A_{pert} at which a tolerable THD is achieved.

3.3 Characterization of FCM

This section provides an experimental approach to validate and characterize the extracted FCM, along with recommendations on how to analyze the extracted FCM.

3.3.1 Non-linear Index

Let us examine a specific row from the extracted FCM that denotes the frequency point k. (3.10) gives the relationship between the voltage vector $\boldsymbol{v}$ and the current $i(j\omega_k)$.

$$v(j\omega_k) = \begin{bmatrix} z_{11} & \dots & z_{kk} & \dots & z_{kh} \end{bmatrix} \boldsymbol{i} \tag{3.10}$$

Consider a test excitation signal for the current where all frequency components are equal i.e. $i = i(j\omega_1) = i(j\omega_2) \cdots = i(j\omega_h)$. Then, using (3.11), the contribution to $v(j\omega_k)$ may be split into diagonal and off-diagonal contributions. z_{kk} enables the diagonal or linear contribution to the current, while $\sum_{r=1,r\neq k}^{h} z_{kr}$ provides the off-diagonal non-linear contribution.

$$v(j\omega_k) = \left(z_{kk} + \sum_{r=1,r\neq k}^{h} z_{kr} \right) \boldsymbol{i} \tag{3.11}$$

The Non-Linear Index (NLI) (N_k) thus characterizes the level of non-linearity at each frequency k. As stated in (3.12), the NLI can be defined as the magnitude ratio of the off-diagonal contribution to the overall contribution. When the diagonal contribution is significant compared to the off-diagonal contributions or when $\sum_{r=1,r\neq k}^{h} z_{kr} = 0$, the NLI is close to zero and when $z_{kk} = 0$ or $y_{kk} \ll \sum_{r=1,r\neq k}^{h} z_{kr}$, the NLI is close to unity. N_k, which ranges between 0 and 1, is a measure of the degree of non-linearity at each frequency k.

$$N_k = \frac{\sum_{r=1,r\neq k}^{h} |z_{kr}|}{\sum_{r=1}^{h} |z_{kr}|} \tag{3.12}$$

3.3.2 Model Accuracy

To validate the retrieved FCM ($\boldsymbol{F_{dut}}$), an experimental approach is proposed. The DUT can be subjected to additional rounds of the excitation signal $\boldsymbol{i_{test}}$, and the current that the DUT draws is recorded. These excitation signals may differ in spectrum from the ones used to extract the FCM, or they may be of the same type. As the FCM has a defined structure, the sole prior requirement is that the excitation test current spectrum should not be the same as those test signals that

were included in the FCM derivation phase. The spectrum ($\boldsymbol{v_{act}}$) of the measured PCC voltage can be obtained by calculating the FFT. The ground truth is represented by the experimentally recorded PCC voltage spectrum $\boldsymbol{v_{act}}$.

The extracted FCM model is used to calculate the predicted spectrum of the PCC voltage ($\boldsymbol{v_{pred}}$), as indicated in (3.13), using the excitation signal $\boldsymbol{i_{test}}$.($\boldsymbol{v_{pred}}$) as shown in (3.13).

$$\boldsymbol{v_{pred}} = \boldsymbol{F_{dut}} \boldsymbol{i_{test}} \tag{3.13}$$

The mean absolute error (MAE) can be used to evaluate the accuracy of the extracted FCM. Equation (3.14) defines the MAE between the experimentally measured PCC voltage and the predicted PCC voltage. The MAE can be computed for multiple iterations of test signals with different perturbation magnitudes. Additionally, the precision can be assessed by computing the standard deviation of the resulting MAE. The confidence level for the derived FCM can be determined by performing such repeated calculations.

$$\eta = \frac{1}{h} \sum_{i=1}^{h} \left| \frac{v_{act}(j\omega_i) - v_{pred}(j\omega_i)}{v_{act}(j\omega_i)} \right| \tag{3.14}$$

Moreover, the accuracy of the FCM model may be stated as a function of frequency since the MAE can be computed per-frequency point. Let us define $\eta_{f,i}$ as the MAE at frequency point i in (3.15).

$$\eta_{f,i} = \left| \frac{v_{act}(j\omega_i) - v_{pred}(j\omega_i)}{v_{act}(j\omega_i)} \right| \tag{3.15}$$

3.4 Simulation Study Cases

3.4.1 Simulation Setup

Fig. 3.1 depicts the simulation setup for the proposed approach. The configuration of the DUT is a three phase LCL-filtered grid-following converter with SRF-PLL. The current control is typically modelled in *dq* domain. Table 3.1 provides the parameters of the DUT. The DUT and grid are linked to the WFZ device in parallel, and Table 3.1 provides the parameters that correspond to it. To reduce the resonance of the LCL

Table 3.1: DUT and WFZ device parameters in simulations

Parameters	Values for DUT	Values for WFZ
Switching frequency	20 kHz	20 kHz
DC link capacitor (C_{dc})	270 μF	270 μF
Inverter side inductor (r_c, L_c)	0.15 Ω, 0.21 mH	0.55 Ω, 2.7 mH
Grid side inductor (r_g, L_g)	0.15 Ω, 0.21 mH	0.36 Ω, 1.8 mH
Filter capacitances	150 μF	1 μF
Damping resistor	0.8 Ω	300 Ω
Current control	K_p = 4e-3 , K_i = 30	K_p = 1.5e-3 , K_i = 60

filter, the split capacitor type shunt RC damper is used into the design of both the DUT and WFZ device [73]. Through a series RL branch with values $R_{grid} = 0.3\Omega$ and $L_{grid} = 1mH$, a grid impedance Z_{grid} is realized. In MATLAB/SIMULINK, switched models are used for the simulations, and a time step of $200ns$ is used.

3.4.2 Study Case 1: Stable Scenario

The DUT with its nominal parameters, as indicated in Table 3.1, is taken into consideration in this study case. Since it is expected that the DC link voltage of the DUT is stiff, the DC side dynamics are minimal. Additionally, this work has taken into account balanced operating conditions. As a result, $\boldsymbol{v_{a,f}} = \boldsymbol{F_{a,a}}\boldsymbol{i_{a,f}}$ is adequate to model the FCM for each phase, wherein the FCM $\boldsymbol{F_{a,a}}$ has the units of impedance.

By choosing $h = 40$, perturbation frequency points up to 2 kHz with a resolution of 50 Hz are taken into account. The spectrum of the WFZ injected current is shown in Fig. 3.2. At $t = 0.6$s, the measurement process commences. The WFZ current is almost negligible during the scanning phase, as shown in Fig. 3.2a. The WFZ device just injects current during the perturbation phase, and Fig. 3.2b shows the corresponding spectrum. The current controller attenuates low frequencies that are injected into the duty cycle of the WFZ device. The

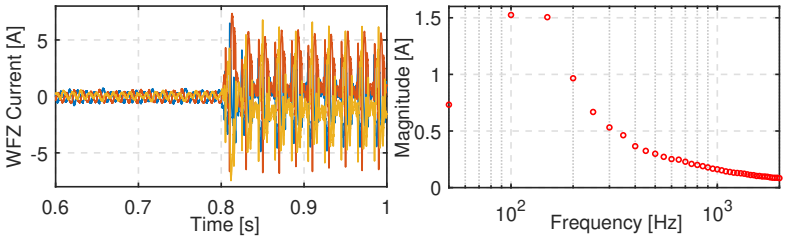

(a) WFZ Current (b) WFZ Current Spectrum

Figure 3.2: WFZ injected current and its spectrum

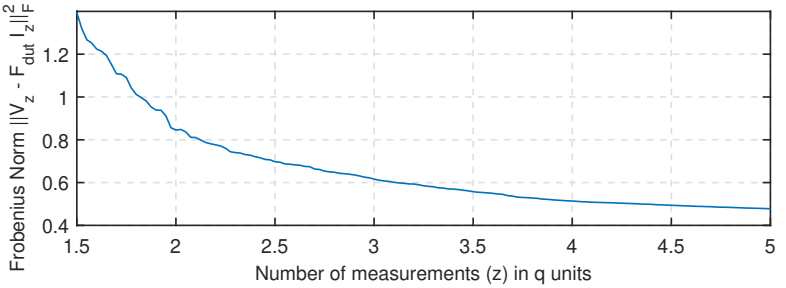

Figure 3.3: Influence of z on the model accuracy

spectrum shown in Fig. 3.2b is explained by the LCL filter of the WFZ device, which attenuates the higher frequency components of the noise current.

The perturbation amplitude A_{pert} is randomly modified within a preset range $A_{pert,min} < A_{pert} < A_{pert,max}$ during each perturbation round. The PCC voltages, WFZ currents, and DUT currents are all measured and recorded. The spectrum of these quantities is obtained by applying FFT. Subtracting the spectrum obtained during the scanning phase from the spectrum obtained during the perturbation phase yields the difference spectrum for each voltage and current variable. The number of elements in $\boldsymbol{i_{a,f}}$ is $q = 1.h$, hence the minimal number of measurement rounds needed to calculate the FCM $\boldsymbol{F_{a,a}}$ with $h = 40$ is $z = q = 40$. The

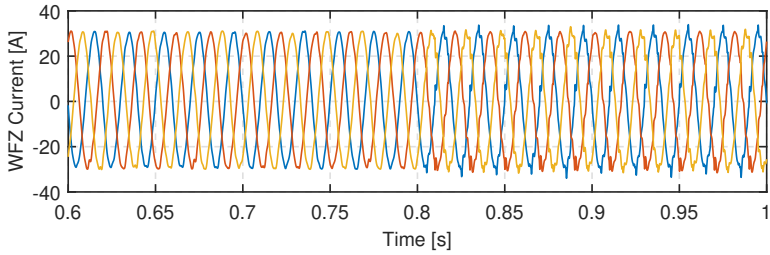

(a) DUT Current

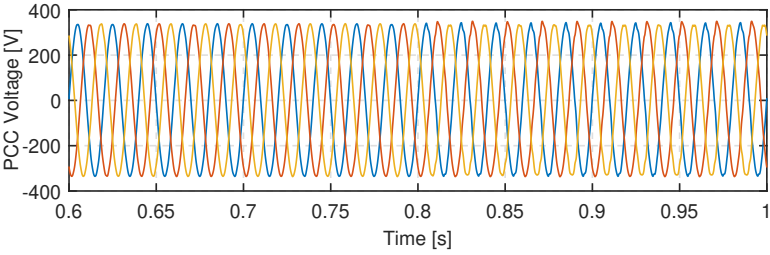

(b) PCC Voltage

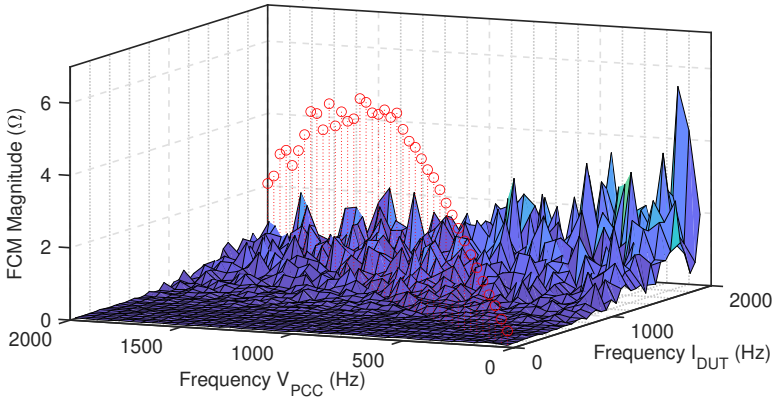

(c) FCM $\boldsymbol{F_{a,a}}$ of DUT

Figure 3.4: FCM measurement in Study Case 1

FCM is computed for each z, ranging from $z = q$ to $z = 5q$, in order to examine the impact of z on the modelling error. The modeling accuracy is represented by the least square norm $||\boldsymbol{I_t} - \boldsymbol{F_{dut}}\boldsymbol{V_t}||_{\mathcal{F}}^2$, which is computed as z varies, as Fig. 3.3 illustrates. It has been observed through a variety of study cases that in order to effectively simulate the power converter, at least $z = 3q$ measurements are needed.

As for study case 1, the FCM measurement findings are shown in Fig. 3.4. Figures 3.4a and 3.4b show the DUT current and PCC voltage during an arbitrary measurement round. The PCC voltage is only slightly affected by the WFZ perturbation currents because the DUT impedance is relatively small and the grid impedance provides a high impedance channel for high current harmonics. Following $z = 5q$ measurements, the FCM $\boldsymbol{F_{a,a}}$ obtained is shown in Fig. 3.4c. For ease of visualization, the linear (diagonal) and off-diagonal components are displayed separately. The high frequency components of DUT currents are coupled with the low frequency components of PCC voltage, as seen in Fig. 3.4c.

3.4.3 Study Case 2: Scenario with Harmonic Instability

The parameters in study case 2 are essentially identical to Table 3.1 except for the current controller gains of the DUT. It is widely accepted that by increasing the current control bandwidth, the harmonic instability condition can be induced. For each given grid impedance, a minimum control bandwidth exists that causes harmonic instability. The system behaves well and is stable at lower grid impedance values. The control gains of the DUT are adjusted to $K_{p,dut} = 0.36$ and $K_{i,dut} = 90$ so that, with the grid impedance Z_{grid}, marginal harmonic instability occurs. The FCM measurement procedure is repeated for the new DUT configuration, as previously described in the study case. The measurement outcomes of study case 2 are shown in Fig. 3.5. The DUT current and PCC voltage for the study case 2 are shown in Figs. 3.5a and 3.5b.

The PCC voltage spectrum assessment reveals the resonance frequency at around 550 Hz. In Fig. 3.6a, the FCM $\boldsymbol{F_{a,a}}$ of the DUT is displayed. It should be noted that the control parameter is the only parameter that has changed in the DUT from study case 1, however, the FCM has changed significantly. Fig. 3.6a shows the FCM acquired from study cases 1 and 2 collectively. As can be shown in Fig. 3.6a, case 2 exhibits much higher linear and off-diagonal components than case 1,

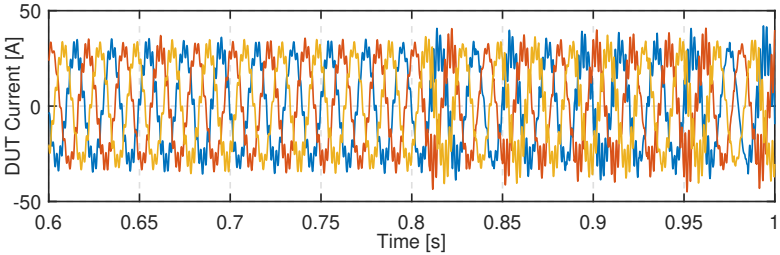

(a) DUT Current

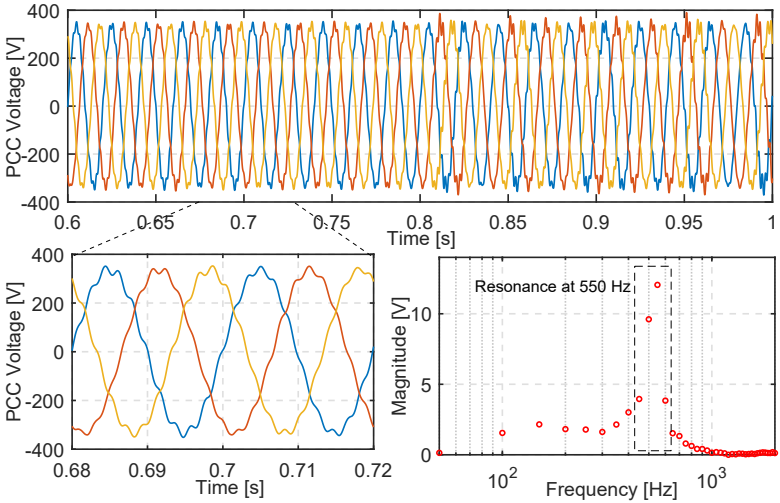

(b) PCC Voltage and its spectrum difference between perturbation and scanning phase

Figure 3.5: PCC voltage and DUT current measurement in study case 2

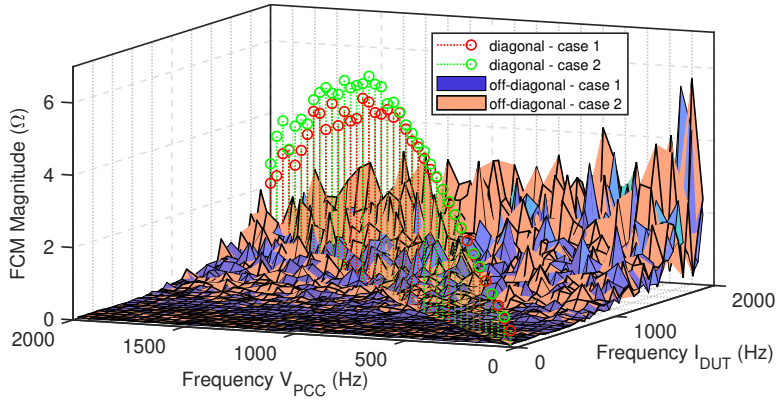

(a) FCM $\boldsymbol{F_{a,a}}$ of DUT

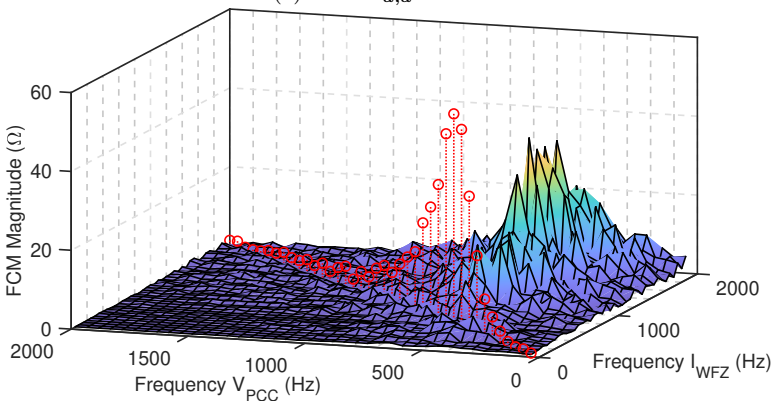

(b) DUT and grid equivalent FCM

Figure 3.6: FCM measurement in study case 2

and higher frequency current harmonics are linked to lower frequency voltage harmonics. As mentioned in Section 3.2.3, the WFZ current and PCC voltage measurements can be used to determine the FCM equivalent of the DUT and grid impedance. Fig. 3.6b displays the corresponding FCM, and at about 550 Hz, the impedance resonance is visible. Both the linear and off-diagonal impedance components that link numerous current harmonics to the 550 Hz voltage harmonic are significant.

3.5 Experimental Verification

3.5.1 Experimental Setup

The hardware configuration in Fig. 3.7 is used to realize the laboratory measurement setup in Fig. 3.1, to further validate the proposed FCM measurement method. Two EA-PSI 91500-30 DC power supply are used to power the DC side of the power converters. A Chroma 61830 regenerative grid simulator acts as the voltage source to which both the power converters synchronize. An adjustable RLC passive rack to used to emulate the grid impedance. As already mentioned, the setup also contains two power electronic converters with LCL filters. The Imperix rapid prototyping technology is used to construct the power electronic converters. In contrast to the shunt RC damper utilized in simulation scenarios, the LCL filters have a series-R type damping. The WFZ measurement device is configured on one converter, while the DUT is configured on the other. The two three phase converters are implemented using Imperix PEB8038 SiC half-bridge power modules. The two power electronic converters are connected in parallel, as seen in Fig. 3.7, and the point of interconnection of both converter forms the PCC. The PCC is connected to the Chroma grid emulator via a programmable RLC passive rack. The DIN-800V and DIN-50A rail-mounted sensors from Imperix are used to measure voltage and current in all phases, respectively. During the measurement, the PCC voltages and the currents injected by the DUT and WFZ device are recorded. It should be noted that the current direction notation provided in Fig. 3.7 is used for FCM calculations. The experimental setup parameters are given in Table 3.2. Both the converters are operated at a switching and sampling frequency of 20 kHz. The grid emulator is operated at 100V RMS between line-neutral and the DC power supplies are operated at 370V.

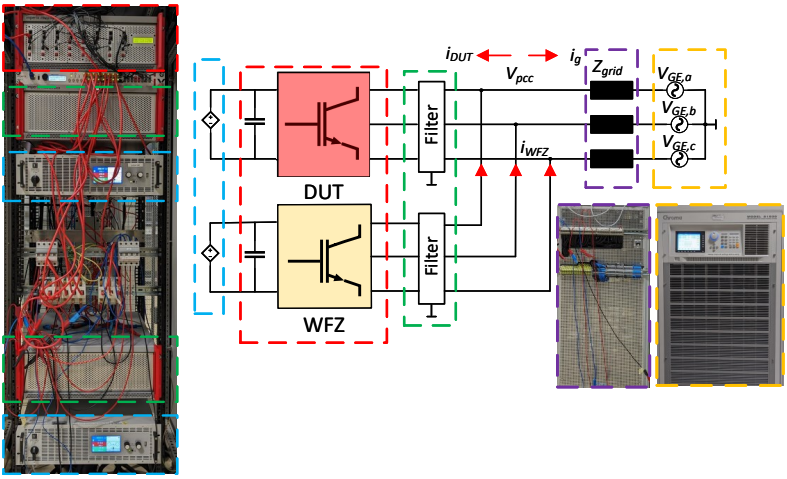

Figure 3.7: Hardware realization of the proposed measurement setup

Table 3.2: Parameters used in experiment

Parameters	Values
Switching frequency	20 kHz
Inverter side inductor (r_c, L_c)	0.2 Ω, 2.3 mH
Grid side inductor (r_g, L_g)	0.2 Ω, 2.4 mH
Filter capacitances	10 μF
Damping resistor	1 Ω
Current control (WFZ)	$K_p = 0.01$, $K_i = 2$
Current control (DUT)	$K_p = 1$, $K_i = 20$
Grid impedance branch	$R_{grid} = 0.3$ Ω , $L_{grid} = 1.5$ mH

3.5.2 Experimental FCM Measurement

The excitation signal is a sum of sinusoids with a starting frequency of 50 Hz and a stop frequency of 1 kHz with a resolution of 50 Hz, as described in Section 3.2.4. The phase of each harmonic is optimized so as to minimize the peak-peak amplitude of the total perturbation signal, using the DE meta-heuristic method [72]. A_{pert} is changed between $1\%V_n < A_{pert} < 2.5\%V_n$ for each perturbation round. The scanning phase, which includes the scanning of all background harmonics and noise in the grid voltage and DUT current, lasts for 0.4 seconds (8000 samples). When the signal v_{pert} is superimposed over the WFZ device's control signal, the perturbation phase similarly lasts for 0.4 seconds. The injected WFZ currents during one of the measurement rounds are shown in Fig. 3.8a. Fig. 3.8a illustrates how a measurement trigger signal is utilized to acquire the waveform that includes both the scanning and perturbation phases. In the respective measurement round, the PCC voltage and DUT current are shown in Figs. 3.8b and 3.8c. The average THD in the perturbed PCC voltage during the measurement is around 2%. Therefore, the extraction of the FCM model is possible with the least amount of grid voltage distortion.

Since switching noise and harmonics are inherent in the PCC voltage, Fig. 3.8b provides a comprehensive test for assessing the efficacy of the proposed empirical modeling approach. Furthermore, as seen in Fig. 3.8c, there is a slight imbalance in Phase B current; hence, the FCM formulation must take into account the coupling effects among each of the phases. Since the DC source is closely controlling the DC link voltage and the harmonics on the DC side are relatively low, the DC link dynamics are excluded for this specific model. However, in a broader sense, DC current and voltage should be considered, particularly in applications like PV inverters or active rectifiers, where DC link dynamics play an important role in stability. Accordingly, based on the aforementioned reasoning, let us consider the following model to be extracted from empirical measurements:

$$\begin{bmatrix} \boldsymbol{v_{a,f}} \\ \boldsymbol{v_{b,f}} \\ \boldsymbol{v_{c,f}} \end{bmatrix} = \boldsymbol{F_{dut}} \begin{bmatrix} \boldsymbol{i_{a,f}} \\ \boldsymbol{i_{b,f}} \\ \boldsymbol{i_{c,f}} \end{bmatrix} \tag{3.16}$$

Observing the spectrum of PCC voltage, it is clear that the 50 Hz perturbation is minimal because the current loop of the WFZ device

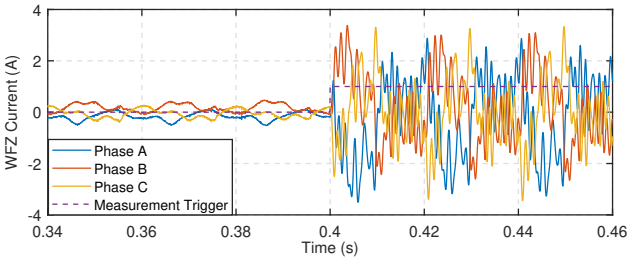

(a) WFZ Current

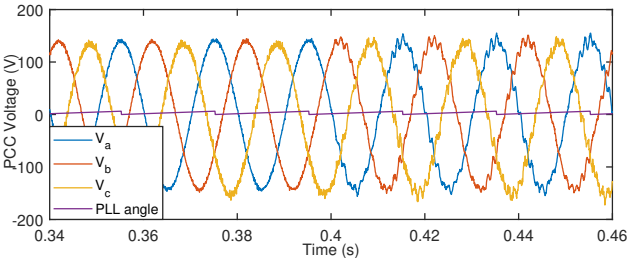

(b) PCC Voltage

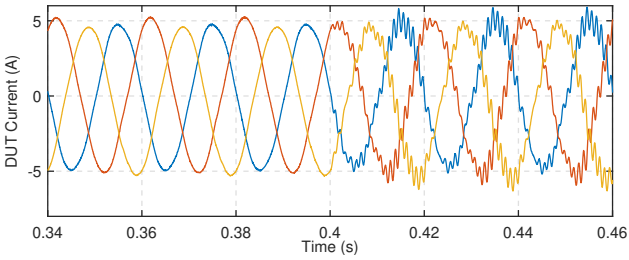

(c) DUT Current

Figure 3.8: Voltage and current waveforms for one trial round using the proposed experimental setup

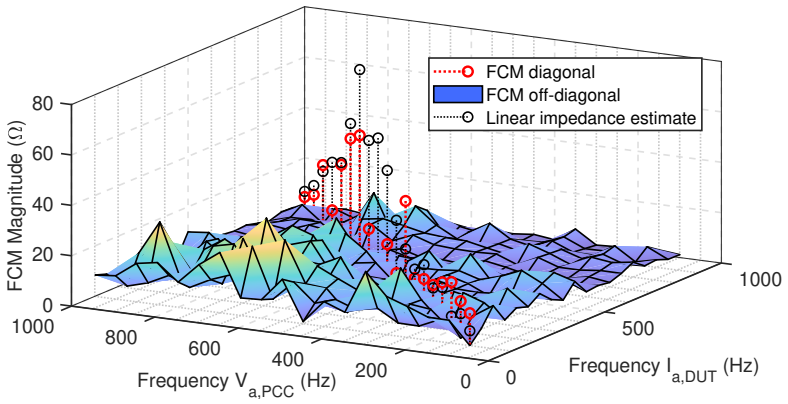

(a) FCM $\boldsymbol{F_{a,a}}$ of DUT

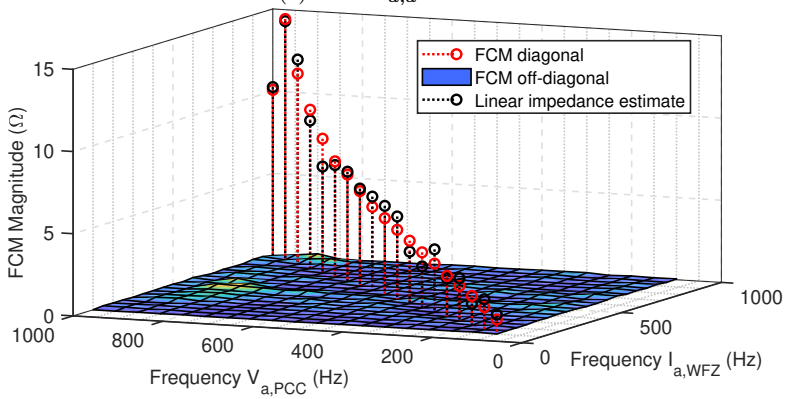

(b) DUT and grid equivalent FCM

Figure 3.9: FCM Extraction using the proposed experimental setup

mitigates the harmonic. As a result, let us only take into account frequencies between 100 Hz and 1 kHz for the analysis in this work, which yields $h = 19$. Each vector containing current and voltage has a dimension of $q = 3h = 57$. The PCC voltage and DUT current data were collected over 150 measurement rounds ($z = 2.6q$), and the corresponding spectrum was computed using FFT. The generalized FCM is computed using least squares, as shown by (3.6), as discussed in Section 3.2.3. The sub-matrices, like $\boldsymbol{F_{aa}}$, can be retrieved from the measured generalized FCM. Fig. 3.9a depicts the FCM $\boldsymbol{F_{aa}}$ magnitude as observed experimentally. Observably, the diagonal component is substantial across the entire frequency range; however, the off-diagonal contributions become substantial above 600 Hz. For a mean perturbation amplitude of $1.5\%V_n$, the linear impedance is also extracted using (3.3), and it is shown in Fig. 3.9a. The linear impedance estimates and the diagonal component of the FCM estimation agree in the low frequency range. On the other hand, a notable distinction between the linear and FCM models is noted between 400 and 800 Hz. The equivalent FCM of the grid and DUT impedance is determined by exchanging the WFZ current spectrum for the DUT current spectrum. The linear Thevenin equivalent impedance measurement is presented for reference in Fig. 3.9b, where the magnitude of equivalent FCM is displayed. The characterisation of FCM is carried out to verify the aforementioned FCM models and to compare the accuracy derived from FCM estimates and linear impedance estimates.

3.5.3 Characterization of FCM

To characterize the extracted FCM experimentally, many rounds of perturbations need to be injected into the PCC from the WFZ device. A halton set is used to generate 50 random test perturbation signals with amplitudes $A_{pert,min} < A_{pert} < A_{pert,max}$ that are not identical to the perturbation amplitudes applied during the model extraction phase, preventing bias caused by depending on known data points. As mentioned in Section 3.3.2, the experimentally measured DUT voltage spectrum serves as the ground truth, while the estimated PCC voltage spectrum from the extracted model via (3.13) serves as the prediction. The MAE is calculated for each measurement trial using equation (3.14). Furthermore, using (3.3) applied to the measurements from the model extraction phase, the average linear model of the converter is extracted. The extracted

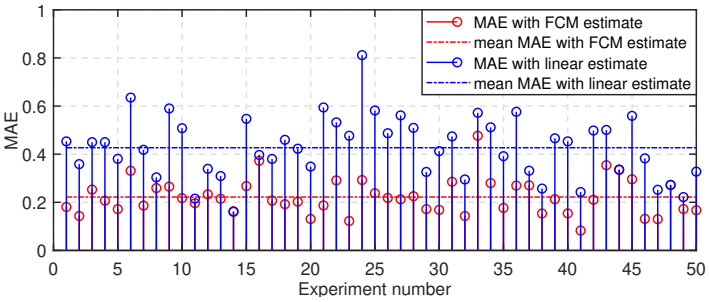

(a) Overall characterization of DUT FCM

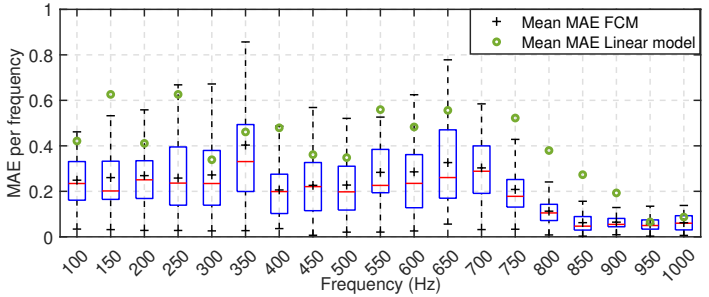

(b) Per Frequency characterization of DUT FCM

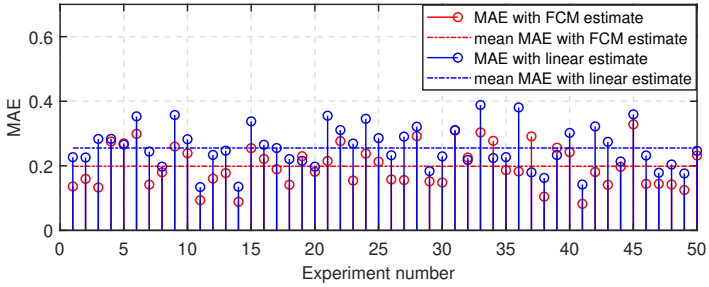

(c) Overall characterization of equivalent FCM

Figure 3.10: FCM characterization through empirical measurements

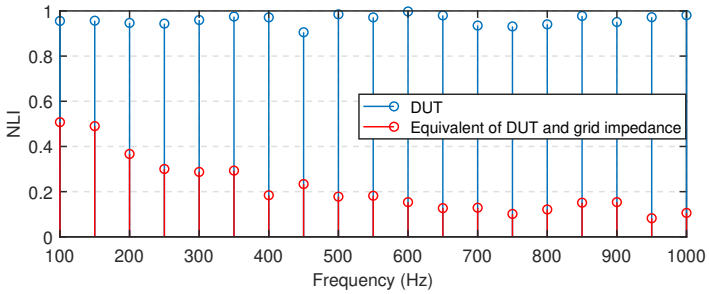

Figure 3.11: NLI of FCM of DUT and NLI of FCM equivalent of DUT and grid impedance

linear impedance model of the converter is used to predict the current spectrum for each of the test perturbations, and the MAE of the linear model is determined. Figure 3.10a compares the MAE for the proposed FCM model versus the linear impedance model. In most of the test cases, the FCM model outperforms the linear model significantly. The FCM model has a reduced overall MAE by 48% compared to the linear model, which demonstrates the superiority of the FCM model. The mean overall MAE with FCM model and linear model are 0.22 and 0.42 respectively.

The MAE can be computed for each frequency using (3.15), allowing to adjudge the accuracy of the extracted FCM as a function of frequency. Figure 3.10b shows the box plot of the MAE for the proposed FCM and the mean of the MAE calculated for the linear model. Fig. 3.10b demonstrates that the FCM model outperforms the linear model at most of the frequency points. The accuracy of the linear model is comparable to that of the FCM model between 0.9 and 1 kHz, whereas the accuracy of the FCM model is consistently low over the entire frequency range.

The NLI is calculated for each of the sub-FCM matrices to determine diagonal dominance. Figure 3.11 depicts the NLI of DUT FCM $\boldsymbol{F_{a,a}}$, as well as the FCM equivalents of DUT and grid. The NLI of $\boldsymbol{F_{a,a}}$ is almost unity over the observed frequency range, indicating a strong off-diagonal contribution. In contrast, the NLI of the equivalent FCM of DUT and grid decreases as the frequency increases as the closed-loop output impedance of the DUT is greater than the grid impedance. As a result, the linear

grid impedance provides a low-impedance path for the injected harmonic currents, and thus the overall dynamics are dominated by the linear grid impedance part at higher frequencies. Fig. 3.10c shows that the linear Thevenin equivalent model performs well in this scenario due to the low NLI of the equivalent FCM at high frequencies. Compared to the Thevenin equivalent linear model, the equivalent FCM model reduces MAE by around 22%.

3.6 Summary

A wideband excitation technique-based FCM measurement method for power electronic converters is proposed in this work. The proposed technique is suitable for both laboratory and field measurement, in contrast to the previously suggested FCM measuring techniques, which are primarily intended for laboratory measurements. The utilization of sum-of-sinusoids is recommended in this work so that meta-heuristic algorithms can optimize each harmonic's phase and perturbation signal. This method reduces the peak-to-peak amplitude of the perturbation. The FCM is extracted by solving a least-square estimate technique after numerous rounds of wideband perturbation application. The FCM model of the power converter can be modified from the generalized FCM model based on the interactions between the AC and DC sides as well as between phases. The equivalent FCM of the grid and DUT can be measured by measuring the WFZ injected current. Potential frequency points that can cause harmonic resonances between the grid and DUT can be accessed, as shown by simulation scenarios. The FCM diagonal and off-diagonal components are considerably altered by changes to the inner control loop.

Additionally, characterization parameters are proposed in this work for evaluating FCM accuracy. The per-frequency MAE shows the accuracy of the FCM as a function of frequency, while the MAE indicates the overall accuracy of the model taking into account all frequency points of interest. The NLI, which is demonstrated to be a measure of the strength of non-linearity, can be used to evaluate the diagonal dominance of the extracted FCM. The analysis carried out in this work leads to the following case-specific conclusions:

1. The experimentally extracted FCM achieves 48 % reduction in MAE compared to estimates made by linear model under the presence of harmonic pollution in PCC voltage

2. From the per-frequency analysis, the proposed method outperforms the linear model at all frequency points

Conducting a comparative analysis of FCM models and NPHD models is necessary in terms of modeling complexity and accuracy. Incorporating FCM models into the existing linear impedance-based harmonic stability analysis tools would improve the predictions made by stability monitoring algorithms and can potentially enable detection of harmonic instability occurrences due to frequency coupling phenomenon.

4

Harmonic Stability Monitoring of Power Electronics Dominated Grids

4.1 Introduction

4.1.1 Motivation and State-of-the-Art

As already covered in Chapter 1, harmonic stability occurs primarily due to the negative or low damping in the medium frequency range introduced by fast inner control bandwidth of the converter, PLLs, control delays in the converter control system, parallel resonance among other converters or power-electronic interfaced constant power loads such as active rectifiers [21, 42, 43, 55]. When a harmonic resonance occurs, the 50 Hz component may remain stable and only the amplitude of the resonant frequency grows over time. Depending on the damping, the magnitude of harmonic may stabilize or continue to grow until the protection triggers which leads to the trip of the power converter[43, 44].

From a theoretical standpoint, harmonic stability analysis could be conducted using state-space models or impedance models which describe the closed-loop behavior of the power converter [21, 69, 74]. State-space approaches are in time-domain and would use eigen value analysis and participation factors. Using the eigen value analysis, the critical oscillatory modes can be identified [21, 74, 75]. Whereas, the impedance based approaches are in frequency-domain and would typically use the Nyquist Stability Criterion (NSC). Using the NSC, the critical frequency where harmonic resonance may occur and the phase margin of the system can be identified. The equivalence of both approaches are well established [21, 74, 75]. Both approaches have a limitation in practical application. Due to the multi-vendor paradigm, these approaches require hardware

parameters, control structure and control parameters to develop detailed models of the converter [76–78]. Measurement-based methods directly overcome this problem, as the model is extracted empirically from the terminal behavior of the converter.

The impedance-based stability analysis was first introduced by R.D Middlebrook for DC systems [79]. Since the Middlebrook criterion is very conservative, several relaxed criterions were developed, and the most widely used method is the NSC [28, 55, 80]. Specific to AC systems, extensions of the NSC for applying to *dq* or sequence domain models are also available [44, 46, 55, 70]. The primary idea of the above-mentioned approaches is to provide a way for evaluating the stability of two interconnected systems. However, such methods are not suitable to evaluate the system-level stability of a multi-bus power network since there are multiple interconnected systems. For state-space approaches, extension to multi-bus system is based on the CCM and they have the same drawback as eigen value analysis [21, 44, 46, 74]. The node admittance matrix approaches provide a way aggregate impedance models into the system level and hence admittance matrix approaches have a computationally efficient compared to CCM approaches and, furthermore, can rely on empirical modelling approaches [21, 44, 46].

Currently, there are only very few non-parametric approaches which use black-box models and they typically use vector fitting approaches to determine or fit a suitable rational transfer function [76–78]. Fitting the non-parametric data to a transfer function remains questionable, especially when poles and zeros of the converter or the grid impedance are not known. Assumptions on the transfer order typically leads to erroneous predictions on the stability. Thus, stability analysis methods that only depend on non-parametric impedance data are required.

4.1.2 Main Contribution

This chapter first proposes a non-parametric formulation of the NSC for a single bus system to determine its stability and compute its stability margin. The proposed method consists of a WFZ device connected to the bus to acquire online impedance measurements of the two interconnected systems. This method is extended to the multi-bus system, and the proposed method is invariant of topology. The key idea is to have WFZ devices only at those nodes that have active components (sources or

loads) and to measure the impedance of active components. Assuming that the topology is known and the cable impedances are known, this dissertation shows that the locally measured converter impedances can be aggregated on a system level, which enables system-level predictions of system stability. The aggregation of impedances on a system level is carried out through nodal analysis using the Y-bus admittance matrix concept. Similar to the single-bus case, a non-parametric stability margin calculation algorithm is also presented. Finally, this dissertation validates the non-parametric stability analysis on a single-bus system, a star-connected system, and a multi-bus test system using hardware experiments.

1. Non-parametric formulation of impedance-based stability criterion

2. Non-parametric impedance-based stability criterion for multi-bus power network

3. Experimental validation for single bus, star-connected and a multi-bus test system

4.2 Impedance based Stability Criterion

Consider a generic three phase grid-connected converter which is represented as a Norton equivalent current source i_c and shunt impedance Z_c as shown in Fig. 4.1. Z_c represents the closed-loop output impedance of the converter. The equivalent grid impedance as measured from the PCC is Z_g. Since the voltage at the PCC is formed by the grid, a Thevenin equivalent representation is considered for the grid, which is a voltage source v_g in series with Z_g as shown in Fig. 4.1. Let the voltage at the PCC and current injected into the grid be v_{pcc} and i_g respectively. Note that the grid and converter are standalone stable systems by design. Interconnection of two stable systems need not result in a resultant system that is stable system. Stability of the interconnection can only be concluded by analysing the interactions either by using theoretical frequency domain models or by an empirical approach.

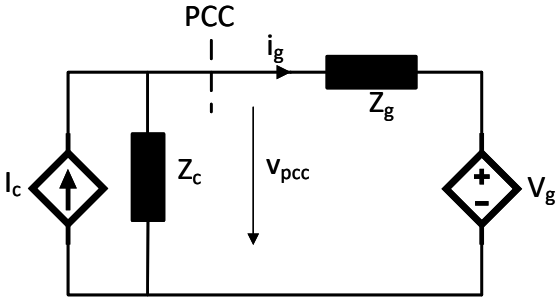

Figure 4.1: Thevenin equivalent model

By KCL and Kirchoff's Voltage Law (KVL), the following equations are valid at the PCC.

$$i_c = i_g + \frac{v_{pcc}}{Z_c} \tag{4.1}$$

$$v_{pcc} = v_g + \frac{i_g}{Z_g} \tag{4.2}$$

Combining the above equations to express v_{pcc} dependency on i_g, we get:

$$v_{pcc} = (Z_g i_c + v_g)\frac{1}{1 + \frac{Z_g}{Z_c}} \tag{4.3}$$

From (4.3), it can be inferred that v_{pcc} is actively influenced by i_c and v_g. Considering the Laplace s-domain of (4.3), the transfer function between i_c and v_{pcc} is derived by ignoring v_g and likewise the transfer function between v_g and v_{pcc} is derived by ignoring i_c. The derived transfer functions are provided in (4.4) and (4.5).

$$V_{pcc}(s) = \frac{Z_g(s)}{1 + \frac{Z_g(s)}{Z_c(s)}} I_c(s) \tag{4.4}$$

$$V_{pcc}(s) = \frac{1}{1 + \frac{Z_g(s)}{Z_c(s)}} V_g(s) \tag{4.5}$$

Both (4.4) and (4.5) can be represented as a feedback transfer function, representation of (4.4) is shown in Fig. 4.2. The impedance ratio

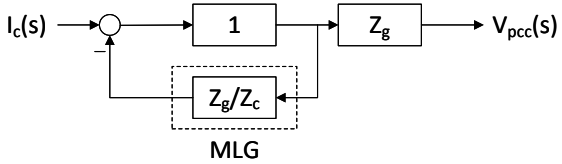

Figure 4.2: Feedback control system representation with MLG

$\frac{Z_g(s)}{Z_c(s)}$ is known as the Minor Loop Gain (MLG). The converter-grid interconnection is stable if the MLG satisfies the NSC. NSC is defined as follows:

Let P be the number of Right Half Plane (RHP) poles of the MLG and N represent the number of clockwise (CW) encirclements of Nyquist plot of the MLG around the critical point $-1 + j0$. Then the number of RHP poles of the closed loop system Z can be determined from (4.6). For a stable system, the number of CW encirclements must equal the number of RHP poles of the MLG i.e. $Z = 0$.

$$Z = P + N \tag{4.6}$$

Denominator of $Z_g(s)$ and the numerator of $Z_c(s)$ contributes to the open-loop unstable poles of the MLG. It is fair to assume that $Z_g(s)$ is stable by design since the grid impedance is typically passive. The converter impedance Z_c on the other hand can have RHP poles particularly due to control delays [81]. However, as the switching frequency of converters are increased every year with improved semiconductor switches and also the control delays are significantly reduced due to improved computational power and double update in PWM, the frequency of the RHP zeros would be pushed to much higher frequencies. The bandwidth limitation with RHP zeros would be negligible in such cases. With the above assumptions, the number of unstable poles of MLG $P = 0$. Therefore, the stability of the closed-loop system can be directly adjudged by observing the encirclement of critical point.

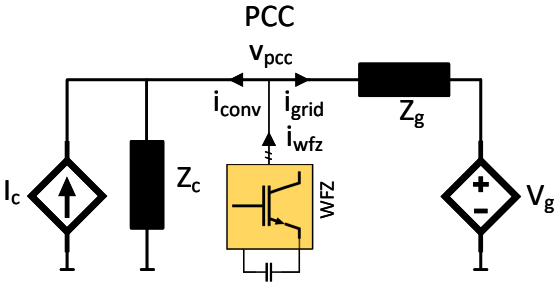

Figure 4.3: WFZ based impedance measurement

4.2.1 Non-parametric Formulation

Consider the measurement setup shown in Fig. 4.3. The WFZ device introduced in Chapter 2 and 3 is connected at the PCC. In this chapter, only the stationary domain measurements are considered and due to balanced assumption, impedance measurement of any arbitrary phase is sufficient. As explained in Section 3.2.4, a sum of sinusoid type of perturbation signal is used due to its advantages over the PRBS signal. The sum-of-sinusoid perturbation signal taken the form in (3.9). The phase of each harmonic is optimized offline using meta-heuristic algorithm to minimize the peak-peak amplitude of the perturbation signal [72]. As already covered in Chapter 2 and 3, the WFZ device uses the scanning and perturbation phases to create a noticeable spectral difference. Let $\Delta V_{pcc}(j\omega_i)$, $\Delta I_{conv}(j\omega_i)$ and $\Delta I_{grid}(j\omega_i)$ represent the difference spectrum of the PCC voltage, converter current and grid current respectively. Using (4.7-4.9), the converter, grid and Thevenin equivalent impedance can be extracted empirically for frequencies $\omega_1 < \omega_i < \omega_{max}$.

$$Z_c(j\omega_i) = \frac{\Delta V_{pcc}(j\omega_i)}{\Delta I_{conv}(j\omega_i)} \tag{4.7}$$

$$Z_g(j\omega_i) = \frac{\Delta V_{pcc}(j\omega_i)}{\Delta I_{grid}(j\omega_i)} \tag{4.8}$$

$$Z_{th}(j\omega_i) = \frac{\Delta V_{pcc}(j\omega_i)}{\Delta I_{wfz}(j\omega_i)} \tag{4.9}$$

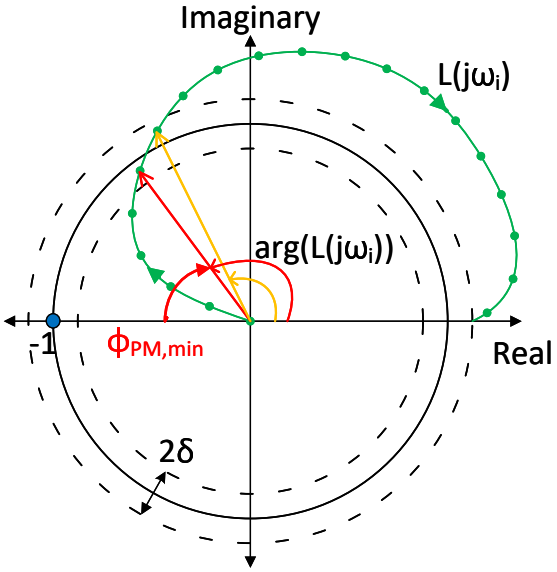

Figure 4.4: Non-parametric NSC for single bus system

The MLG ($\mathcal{L}$) is calculated as a function of frequency ω_i as shown in (4.10).

$$\mathcal{L}(j\omega_i) = \frac{Z_g(j\omega_i)}{Z_c(j\omega_i)} \tag{4.10}$$

By identifying the point where $\mathcal{L}(j\omega_i)$ intersects with the unit circle, the phase margin can be calculated, and the frequency at which this intersection happens is termed the critical frequency (ω_c) or gain crossover frequency. When the phase margin is significantly low, there is a possibility that the system may resonate at the critical frequency. Consider the exemplary Nyquist plot shown in Fig. 4.4, where, the non-parametric locus of $\mathcal{L}(j\omega_i)$ is shown as ω_i varies. Consider two circles whose radius are $1-\delta$ and $1+\delta$ respectively which forms an annular region that is symmetric around the unit circle. Note that δ needs to be selected offline based on observation and it is fixed. δ is dependent on the frequency resolution of the perturbation. Higher the frequency resolution lower the

δ value. The algorithm 1 provides the steps to calculate the minimum phase margin and critical frequency for a non-parametric analysis.

Algorithm 1 Phase margin calculation for single bus system

Require: $Z_c(j\omega_i)$ and $Z_g(j\omega_i)$ for all $\omega_1 < \omega_i < \omega_h$
Ensure: $i = 1$ and $flag = 0$
  while $i \leq h$ **do**
    Calculate MLG $\mathcal{L}(j\omega_i)$
    Calculate $|\mathcal{L}(j\omega_i)|$
    if $1 - \delta < |\mathcal{L}(j\omega_i)| < 1 + \delta$ **then**
      Calculate phase margin $\Phi_{PM,Calc}$ = 180 - $arg\big(\mathcal{L}(j\omega_i)\big)$
      if $flag = 0$ **then**
        $\Phi_{PM,min} = \Phi_{PM,Calc}$ and $\omega_c = \omega_i$ and $flag = 1$
      end if
      if $flag = 1$ and $\Phi_{PM,Calc} < PM_{PM,min}$ **then**
        $\Phi_{PM,min} = \Phi_{PM,Calc}$ and $\omega_c = \omega_i$
      end if
    end if
    $i = i + 1$
  end while

An alternate method to using the Nyquist plot would be to use the Bode plot to calculate the phase margin. Note that this method would be suitable for single bus systems such as star-connected system. The description of this method is covered in detail in Chapter 5.2.1, focusing on its application to a particular topology involving a star-connected system. The analysis using Bode plots are not suited for MIMO system.

4.3 Non-parametric Nyquist Stability Criterion for Multi-bus Power Network

Consider a n node multi-bus power network as shown in Fig. 4.5. Let g be the number of buses with active sources and active loads. Active source represent an external grid connection with an equivalent impedance, a GFL or GFM acting as a source or a GFL acting as a load. Let l be the number of buses which do not have any current injection or have only

passive components such as resistive loads and shunt capacitors. The total number of buses in the power network is $n = g + l$.

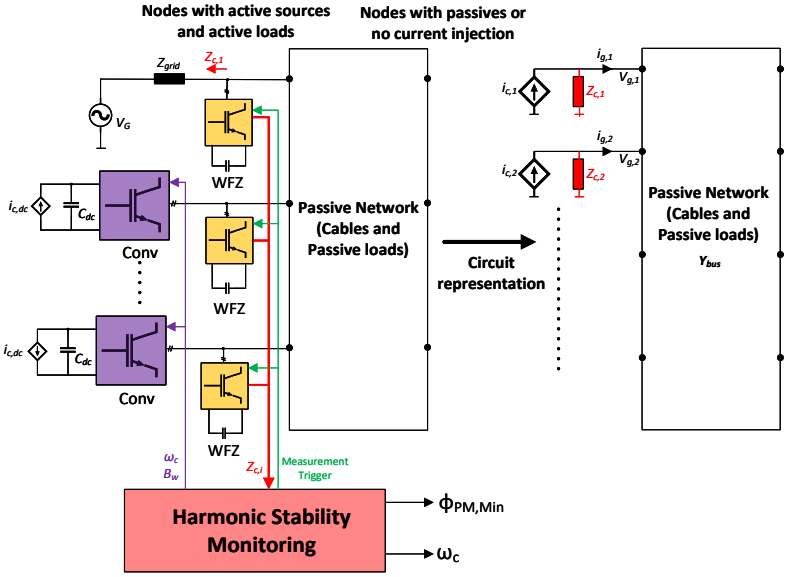

Figure 4.5: Harmonic Stability Monitoring Concept

At each source node, a WFZ device is connected to measure the closed-loop output impedance of the source $Z_{c,i}$ as shown in Fig. 4.5. This work proposes a centralized harmonic stability monitoring system that analyzes and quantifies the stability of the system. The following steps are performed by the centralized platform when the stability monitoring is required:

- Step 1: When the system is in steady state, the measurement trigger is applied to all WFZ devices simultaneously

- Step 2: Each WFZ device performs a scanning and perturbation phase with identical and equal timings to compute the

non-parametric impedance $Z_{c,i}$ of the source. The measured impedances is published to the centralized platform

- Step 3: Non-parametric stability monitoring is performed to calculate the minimum phase margin of the system $\Phi_{PM,Min}$ and the critical frequency ω_c where harmonic resonance may occur

- Step 4: To mitigate harmonic instability, a minimum guaranteed system phase margin needs to be specified. Based on this specification, the bandwidth $\mathcal{B}_w$ (frequency range around the critical frequency) where virtual damping is required would be computed. ω_c and $\mathcal{B}_w$ values are published to all converters. This step is covered in Chapter 5

The measurement trigger is applied simultaneously to all WFZ devices, and the coordination is done with the centralized monitoring system. This simultaneous application of perturbation does not create any interference with the local impedance measurements. At each node, the local WFZ current injection along with the perturbations from other nodes appears as a perturbed voltage source to the converter.

Let $V_n(j\omega_i)$ represent the voltage vector for all n buses at frequency point ω_i. The following partitioning of nodes can be made $V_n(j\omega_i) = \begin{bmatrix} V_g(j\omega_i) & V_l(j\omega_i) \end{bmatrix}^T$.

The current injection vector $I_n(j\omega_i)$ can be partitioned as $I_n(j\omega_i) = \begin{bmatrix} I_g(j\omega_i) & \mathbf{0} \end{bmatrix}^T$, where $I_g(j\omega_i)$ represents the current injection at the g number of source buses. In the derivation that follows, each equation represents an independent complex-valued calculation at frequency ω_i and therefore the notation $(j\omega_i)$ is dropped for improved readability. The circuit representation in Fig. 4.5 separates all active current injections from the passive components in the network. The network consists mainly of cables that interconnect various nodes, resistive loads, and shunt capacitors. Thus, the node voltage dependence on the current injections can be expressed through the Y-bus admittance matrix Y_{bus} as shown in (4.11).

$$\begin{bmatrix} I_g \\ \mathbf{0} \end{bmatrix} = \underbrace{\begin{bmatrix} Y_{bus,gg} & Y_{bus,gl} \\ Y_{bus,lg} & Y_{bus,ll} \end{bmatrix}}_{Y_{bus}} \begin{bmatrix} V_g \\ V_l \end{bmatrix} \tag{4.11}$$

Since l nodes have no current injection, the voltage V_l can be expressed in terms of V_g.

$$V_l = -Y_{bus,ll}^{-1} Y_{bus,lg} V_g \tag{4.12}$$

Using (4.12) in the first row of (4.11), we have I_g expressed in terms of V_g as shown in (4.13). This reductive step is also known as Kron reduction and $\boldsymbol{Y_{red}}$ is the Kron reduced admittance matrix.

$$I_g = \underbrace{\left\{Y_{bus,gg} - Y_{bus,gl} Y_{bus,ll}^{-1} Y_{bus,lg}\right\}}_{\boldsymbol{Y_{red}}} V_g \tag{4.13}$$

As the goal is to study the influence of converter current injections I_c on the node voltages, consider the circuit representation in Fig. 4.5 and by applying KCL to the source nodes, we have the following:

$$I_g = I_c - \boldsymbol{Z_c}^{-1} V_g \tag{4.14}$$

Here, $\boldsymbol{Z_c}$ is a diagonal matrix of dimension $g \times g$ consisting of all the measured source impedances i.e $\boldsymbol{Z_c} = diag(Z_{c1}, Z_{c1}, \ldots, Z_{cg})$. Equating (4.13) and (4.14), the closed-loop transfer function matrix that maps the source current I_c with the node voltage v_g is obtained.

$$\{\boldsymbol{Z_c}^{-1} + \boldsymbol{Y_{red}}\}^{-1} I_c = V_g \tag{4.15}$$

By factoring $\boldsymbol{Y_{red}}$ from the above equation, the transfer function of the MIMO system is obtained in the standard feedback form as (4.16).

$$\{I + \boldsymbol{Y_{red}}^{-1} \boldsymbol{Z_c}^{-1}\}^{-1} \boldsymbol{Y_{red}}^{-1} I_c = V_g \tag{4.16}$$

The MLG matrix $\boldsymbol{\mathcal{L}_1}$, which is the feedback transfer function matrix of the above MIMO system is given by (4.17).

$$\boldsymbol{\mathcal{L}_1}(j\omega_i) = \boldsymbol{Y_{red}}^{-1} \boldsymbol{Z_c}^{-1} \tag{4.17}$$

To adjudge the stability of a MIMO system, the Generalized Nyquist Criterion (GNC) needs to be applied. The GNC is stated as follows:

Let P be the number of unstable poles of $\boldsymbol{\mathcal{L}_1}$ and let $\lambda_1(j\omega_i)$, $\lambda_2(j\omega_i) \ldots$ $\lambda_g(j\omega_i)$ represent the g eigen values of $\boldsymbol{\mathcal{L}_1}(j\omega_i)$ at frequency ω_i. The characteristic loci are defined as the paths traced by each eigen value as the frequency runs from ω_{min} to ω_{max}. Consider n_1, $n_2 \ldots$ be the number of CW encirclements of each eigen value loci around the critical point

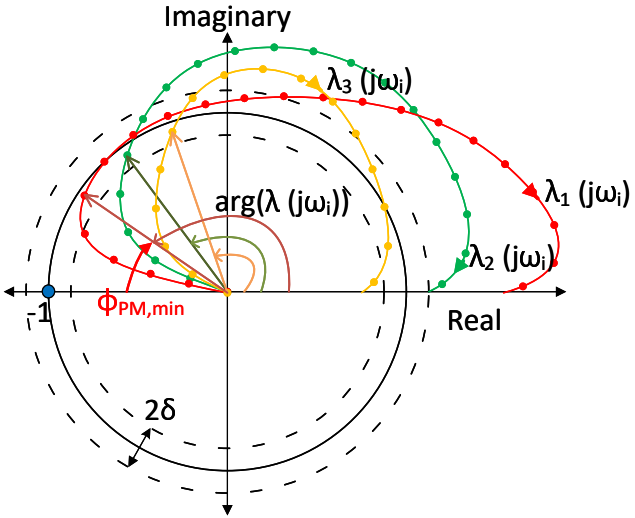

Figure 4.6: Non-parametric NSC for a multi-bus system

$-1 + j0$. The total number of CW encirclements is $N = n_1 + n_2 + \ldots n_q$. Then, for a system to be a stable, the number of RHP poles of the closed loop system $Z = P + N$ must be 0.

It is observed $\boldsymbol{Z_c}^{-1}$ can be numerically unstable especially when the voltage perturbations are negligible under strong grid (low grid impedance) conditions. Therefore, instead of $\boldsymbol{\mathcal{L}_1}$, the inverse MLG $\boldsymbol{\mathcal{L}_2}$ as provided in 4.18 can be used. The eigen values of $\boldsymbol{\mathcal{L}_2}$ are the reciprocal of the eigen values of $\boldsymbol{\mathcal{L}_1}$. By the Generalized Inverse Nyquist Criterion (GINC), the stability rule as states above is valid for the reciprocal of eigen values. Thus, in this dissertation, for the above-mentioned reason, the stability analysis is performed using $\boldsymbol{\mathcal{L}_2}$.

$$\boldsymbol{\mathcal{L}_2}(j\omega_i) = \boldsymbol{Z_c Y_{red}} \tag{4.18}$$

As shown in Fig. 4.6, phase margin is computed for each eigen value loci and the smallest critical phase value is the overall minimum phase margin of the MIMO system. Similar to the non-parametric phase margin calculation for single bus system, Algorithm 2 provides the

steps to calculate the phase margins and critical frequency of each eigen value loci and also determine the overall minimum phase margin and its corresponding critical frequency. Algorithm 2 is applicable not only for meshed networks but also for radial systems as shown in Fig. 4.7.

Algorithm 2 Phase margin calculation for multi-bus system

Require: $\boldsymbol{\lambda}(j\omega_i)$ for all $\omega_1 < \omega_i < \omega_h$
Ensure: $i = 1$, $k = 1$ and $flag = 0$
  while $k \leq g$ **do**
    while $i \leq h$ **do**
      Calculate $|\lambda_k(j\omega_i)|$
      if $1 - \delta < |\lambda_k(j\omega_i)| < 1 + \delta$ **then**
        Calculate phase margin $\Phi_{PM,k,Calc}$ = 180 - $arg\big(\lambda_k(j\omega_i)\big)$
        if $flag = 0$ **then**
          $\Phi_{PM,k,min} = \Phi_{PM,k,Calc}$ and $\omega_{c,k} = \omega_i$ and $flag = 1$
        end if
        if $flag = 1$ and $\Phi_{PM,k,Calc} < PM_{PM,k,min}$ **then**
          $\Phi_{PM,k,min} = \Phi_{PM,k,Calc}$ and $\omega_{c,k} = \omega_i$
        end if
      end if
      $i = i + 1$
    end while
    $flag = 0$ and $k = k + 1$
  end while
  $\Phi_{PM,min} = Min(\Phi_{PM,k,min}) \rightarrow$ get index m of $Min(\Phi_{PM,k,min}) \rightarrow \omega_c = \omega_{c,m}$

4.4 Experimental Investigation and Validation

To validate the non-parametric stability criterion for single bus from Section 4.2.1 and multi-bus system from Section 4.3, the experimental setup in Fig. 4.8 is considered. The Chroma 618300 grid emulator acts as the voltage source that represents the grid connection. An adjustable RLC passive rack is used to realize the grid model. In this study, three types of grid models are considered: single grid-connected converter, multiple converters within star connection and a 3-bus meshed network.

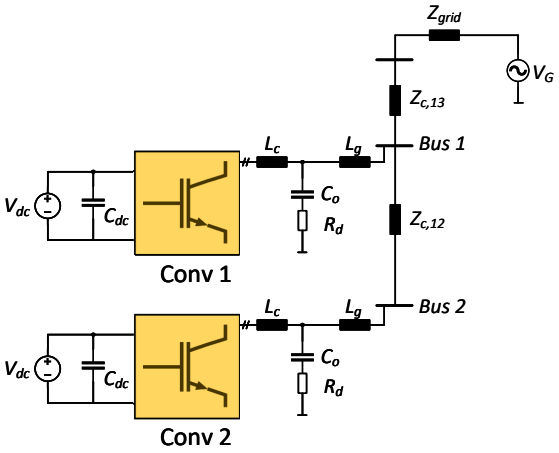

Figure 4.7: Radial system

The two three phase converters are implemented using Imperix PEB8038 SiC half-bridge power modules. Elimination of switching harmonics are achieved through an output LCL filter and to damp the resonance of the LCL filter, a series resistor type damping is used. The parameters of the converter are provided in Table 3.2. The DIN-800V and DIN-50A rail-mounted sensors from Imperix are used to measure voltage and current in all phases, respectively. Two EA-PSI 91500-30 DC power supply are used to power the DC side of the power converters. It must be noted that the two converters are used interchangeably. To measure the impedance of converter 1, converter 2 is configured as the low bandwidth WFZ device and vice versa. The control parameters needs be appropriately setup based on Table 3.2. A sum-of-sinusoid perturbation signal is used in the WFZ device and the start and end frequencies are 100 Hz and 2 kHz respectively with an interval of 50 Hz. The phase of each harmonic is optimized to reduce the peak-peak amplitude of the signal [72]. The measurement and scanning phases for all measurements are 0.4s each and an external trigger signal is used to start the perturbation phase. All the converters use a three phase SRF-PLL to synchronize with the voltage produced by the grid emulator. The grid emulator is operated

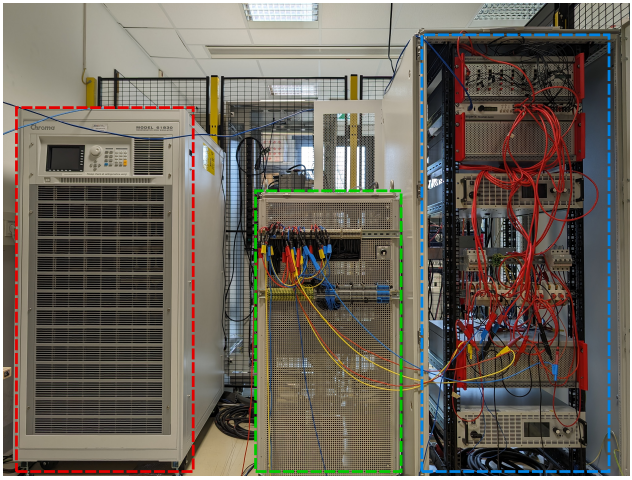

Figure 4.8: Picture of the experimental system

with an AC voltage of 100V RMS and the DC side supply voltages for the power converters are set as 370V.

4.4.1 Study Case 1: Single Converter System

The single line diagram of the proposed setup is shown in Fig. 4.9. The setup consists of converter 1 acting as a GFL with *dq* domain current control function. Converter 2 is configured to act as the WFZ device to measure the impedance of converter 1 and to measure the grid impedance. The time domain waveforms of the DC link voltage, WFZ current (converter 2 current), PCC voltage and converter 1 current are shown in Fig. 4.10. Perturbation currents from the WFZ device are injected only after 0.4s when the trigger signal is applied. The injected perturbation currents split into two paths, one current path is through converter 1 while the other is through the grid emulator. The injected currents cause perturbations on converter 1 current as well the PCC voltage. Fig. 4.10 also shows the difference spectrum for the above 3 quantities.

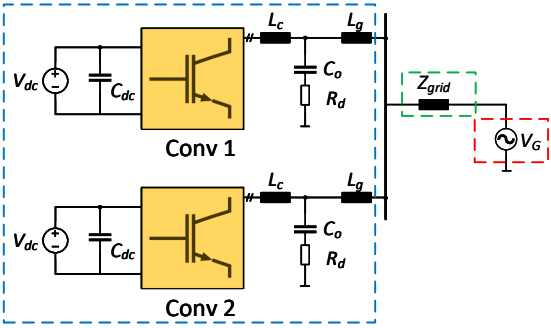

Figure 4.9: Star-connected system

Using the converter and WFZ current measurements, the grid current that flow into the grid emulator is also known. Thus, using (4.7) and (4.8), the non-parametric impedance and subsequently the MLG is calculated and furthermore, applying Algorithm 1, the critical frequency and the stability margins can also be determined.

Remark: Note that the grid emulator is not an ideal or stiff voltage source. The grid emulator is also a power electronic converter with bandwidth limitations. The grid impedance that is measured in this work is a series combination of the known passive grid impedance branch along with the closed-loop output impedance of the grid emulator.

Grid impedance has a significant impact on the stability of the system as the the intersection or overlap point of the grid and converter impedance magnitude depends on the grid impedance. The phase difference between the converter and grid impedance at this critical frequency gives the phase margin. The experiments pertaining to influence of grid impedance are shown in Fig. 4.11 and three grid impedance cases are considered. The resistive component of grid impedance is 0.3 Ω and the the inductances are 0.5, 1.0 and 1.5 mH. During the test cases, the control parameters are kept at the nominal values. The corresponding impedance magnitude and phase plots are shown in Figs. 4.11a and 4.11b respectively. The critical frequencies at which the inverter and grid admittance intersect and the corresponding phase margins are shown in Table 4.1.

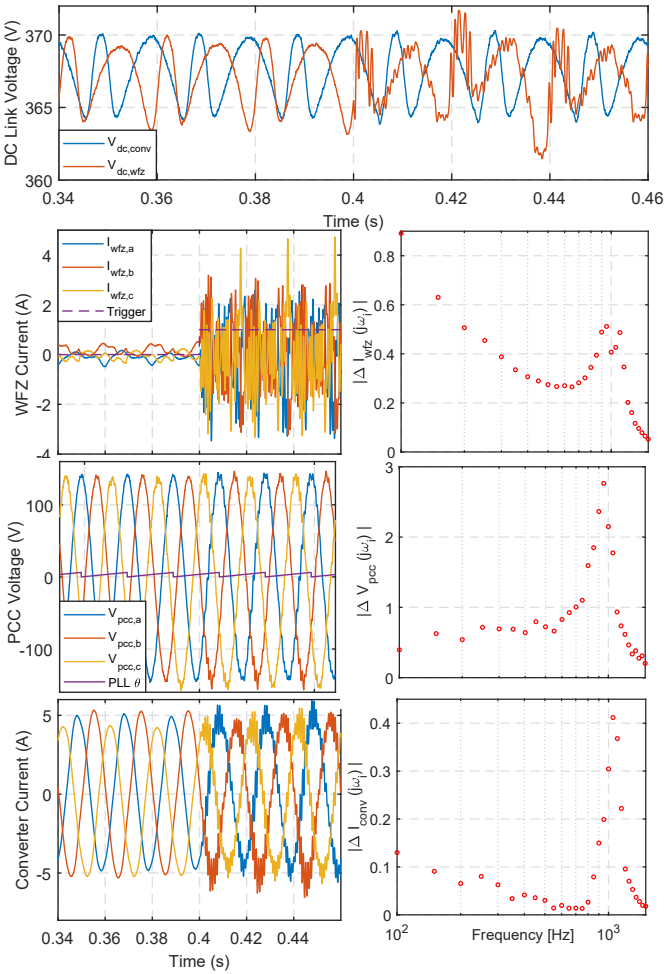

Figure 4.10: Time domain plot - grid and converter impedance extraction for NP-NSC

Table 4.1: Study case 1: Influence of grid impedance on converter stability

Grid impedance parameters	Critical frequency (ω_c) (Hz)	Phase margin (degrees)
0.3Ω, 0.5mH	950	70.30
0.3Ω, 1.0mH	1000	58.50
0.3Ω, 1.5mH	1000	48.25

The Nyquist plots shown in Fig. 4.11c concur with the analysis from the bode plots. The critical frequency (ω_c) is the frequency at which the Nyquist plot intersects the unit circle. The following clarification should be made on the Nyquist plot:

As the perturbation injection resolution is 50 Hz, the impedances are acquired for every 50 Hz starting from 100Hz to 2 kHz. The MLG is also computed with the same resolution. Let us define another frequency vector starting from 100 Hz until 2 kHz with a resolution of 10Hz. Using the cubic-spline interpolation technique [82], the MLG is interpolated to virtually increase the frequency resolution. Using the updated frequency vector, Algorithm 1 is applied to determine the phase margin. The parameter δ is set as $1e-2$ which is sufficient enough to capture the data points of the Nyquist loci that lies close to the unit circle. ω_c and $\Phi_{PM,min}$ computed from the NP-NSC matches the results obtained from Bode plots as shown in Table 4.1.

The proportional gain $K_{p,cc}$ of the inner current control loop has a significant role in harmonic stability as this parameter modifies the medium frequency magnitude and phase behavior of the converter. Since the star-connected system is an extended case of a single converter system, this analysis is performed for the star-connected system.

4.4.2 Study Case 2: Star-Connected System

The single line diagram of the star-connected system is shown in Fig. 4.9. The star connection resembles a PV or wind-farm collector grid of RES based power plant. The proportional gain of the inner current control modifies the out impedance shape in the medium frequency range. It is possible excite a resonance either with the grid impedance or with the neighboring parallel converters.

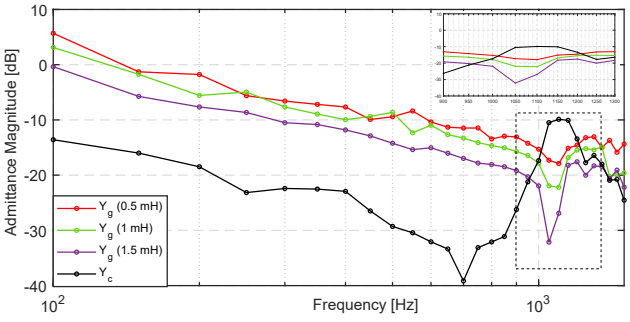

(a) Impedance magnitude

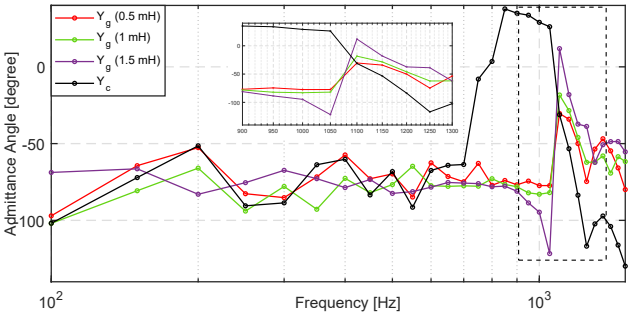

(b) Impedance phase

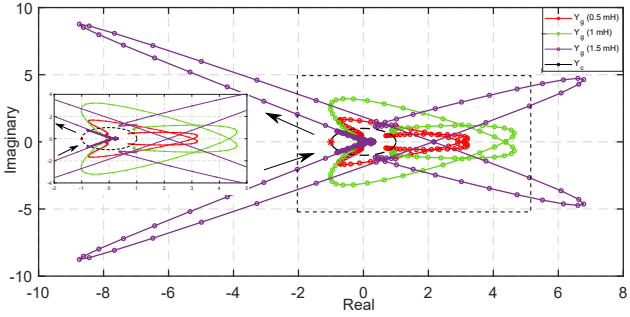

(c) NP-NSC plot

Figure 4.11: Study case 1: Influence of grid impedance on system stability

Table 4.2: Study case 2: Influence of proportional gain on stability of the star-connected system

Proportional gains	Critical frequency (ω_c) (Hz)	Phase margin (degrees)
$K_{p,cc1} = 1$, $K_{p,cc2} = 1$	980	39.90
$K_{p,cc1} = 2$, $K_{p,cc2} = 1$	905	39.9
$K_{p,cc1} = 3$, $K_{p,cc2} = 1$	910	31.7
$K_{p,cc1} = 5$, $K_{p,cc2} = 1$	unstable at 910 Hz	-20

To measure the impedance of the power converter 1, converter 2 is configured as the WFZ device and similarly converter 1 is configured as the WFZ device to measure the impedance of converter 2. The two converter impedances, due to the parallel connection, can be reduced to 1 equivalent impedance. During the above mentioned impedance measurements, the grid impedance is also measured. The grid impedance consists of both the passive branch and the impedance of the grid emulator. For these set of experiments, the grid impedance is constant with a resistance of 0.3Ω and inductance of 1.5 mH. Current references for converter 1 are $i_{dq} = [5 - 3]^T$ A and for converter 2 are $i_{dq} = [3 - 5]^T$ A. The integral gains for both converters are set as 20. Table 4.2 provides the phase margin and critical frequency as $K_{p,cc1}$ is increased. It can be seen that the phase margin reduces and becomes negative. Fig. 4.12a shows that the admittance magnitude of the converter reduces and the phase increase is significant. Observe that the phase difference between the grid and converter admittance is equal or greater than 180 degrees around the critical frequency. This shows that the system is unstable for high gain values. Identical conclusions are reached with the Nyquist plot as well. From the comparative case it has been observed that the phase margins reduce with increase in $K_{p,cc}$ and furthermore for $K_{p,cc} = 5$ and higher, the Nyquist plot encircles the critical point twice.

The experimental verification of the stable scenario considering gains of $K_{p,cc1} = 1$ and $K_{p,cc2} = 1$ is shown in Fig. 4.13. The current waveforms

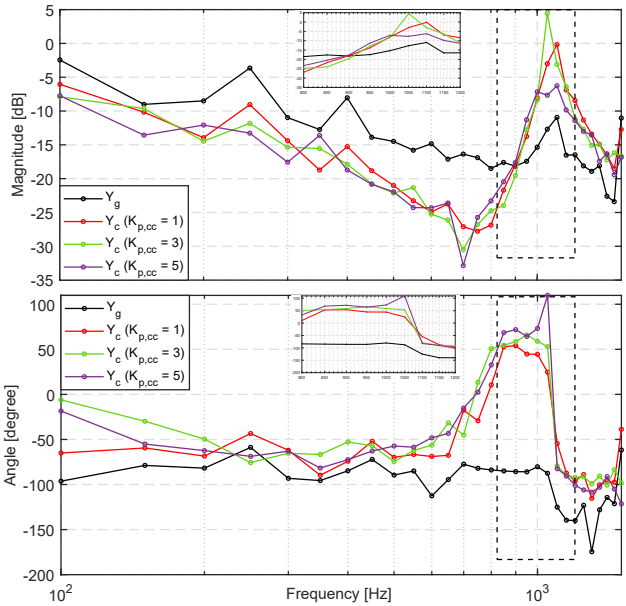

(a) Impedance magnitude and phase

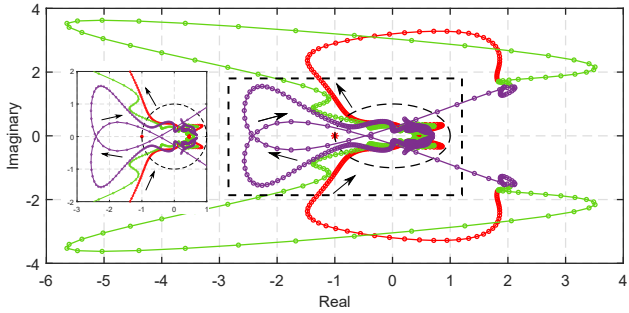

(b) NP-NSC plot

Figure 4.12: Study case 2: Influence of control parameter on system stability

are very stable and do not cause any higher order harmonics and similarly the PCC voltage quality is also clean.

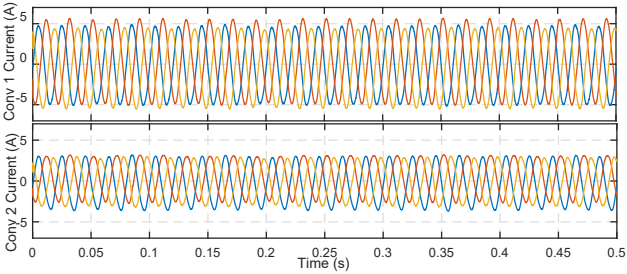

Figure 4.13: Study case 2: Stable operation of the star-connected system for $K_{p,cc1} = 1$ and $K_{p,cc2} = 1$

The experimental validation of the unstable scenario considering gains of $K_{p,cc1} = 5$ and $K_{p,cc2} = 1$ is shown in Fig. 4.14. The converter is started up with a low gain to achieve a stable steady. In steps, the control gains are increased to $K_{p,cc} = 5$ and as a result harmonic instability issue occurs which slowly gets amplified as shown in Fig. 4.14. Due to the negative damping, the harmonics amplify and once either one of currents exceed the peak safety setting of 10A, all PWMs for both converters would be turned-off. Around 0.42s, the current in converter 1 exceeds 10A limit which leads to the turn-off of both power converters. The frequency of oscillation observed to be close to 950 Hz during the hardware experiment is very close to the impedance based model.

4.4.3 Study Case 3: Multi-bus system

The experimental setup corresponding to the multi-bus system is shown in Fig. 4.15. The multi-bus system as shown in Fig. 4.15 consists of 3 buses, 2 GFL and 1 external grid connection. The 3 buses are interconnected with cables which are realized as lumped RL lines representing short distribution line. Consider that $r_{c,ij}$ and $l_{c,ij}$ represent the cable resistance and impedance between buses i and j. The cables have the following parameters: $r_{c,12} = 0.3\Omega$, $l_{c,12} = 0.5mH$; $r_{c,12} = 0.3\Omega$, $l_{c,13} = 1.0mH$ and $r_{c,23} = 0.3\Omega$, $l_{c,23} = 1.0mH$.

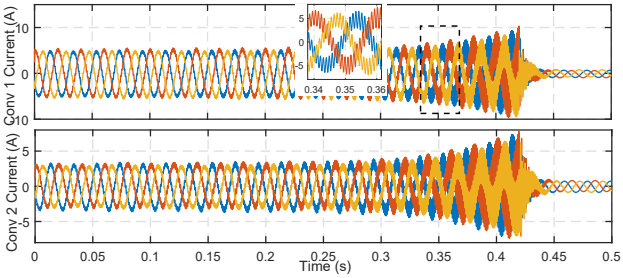

Figure 4.14: Study case 2: Unstable operation of the star-connected system for $K_{p,cc1} = 5$ and $K_{p,cc2} = 1$

Table 4.3: Study case 3: Influence of proportional gain on multi-converter system stability

Proportional gains	Critical frequency (ω_c) (Hz)	Phase margin (degrees)
$K_{p,cc1} = 1$, $K_{p,cc2} = 1$	965	28.50
$K_{p,cc1} = 2$, $K_{p,cc2} = 2$	965	19.00
$K_{p,cc1} = 3$, $K_{p,cc2} = 2$	965	14.40
$K_{p,cc1} = 4$, $K_{p,cc2} = 2$	965	4.1
$K_{p,cc1} = 5$, $K_{p,cc2} = 2$	Unstable at 1.035kHz	-4.9

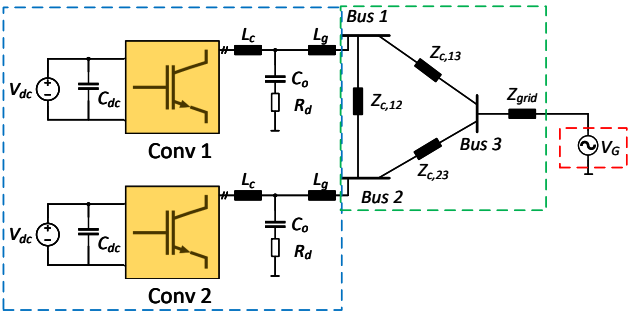

Figure 4.15: Multi-bus system

As explained previously, the goal is to show that local impedance measurements can be aggregated on a system level to show accurate system-level stability predictions. To measure the impedance of converter 1, converter 2 is configured to operate in WFZ mode and furthermore, converter 2 is connected to Bus 1 to measure the impedance of converter 1. Following the previous step, converter 1 is configured as a WFZ device and it is connected to Bus 2 to make the impedance measurement of converter 2.

By reverting back to the original configuration, the time domain response is observed for the converters. The observation of the time-domain cases matches the predictions of the frequency-domain analysis for all of the cases.

Current references for converter 1 are $i_{dq} = [5 - 3]^T$ A and for converter are $i_{dq} = [3 - 5]^T$ A. The integral gains for both converters are set as 20 whereas the proportional gains are varied. Since the network has 3 buses ($n = 3$) and all buses have active sources ($g = 3$), there is no need of a Kron-reduction and the Y_{bus} can be directly used. For the given 3-bus system, there are 3 characteristic eigen value loci (λ_1, λ_2 and λ_3). By computing the MLG matrix, the eigen values are computed. By defining a new frequency vector with higher resolution, the eigen values are interpolated using the cubic-spline method [82]. By applying Algorithm 2, the phase margin and minimum critical frequency are identified.

Initially, the proportional gains of both converters are set as $K_{p,cc1} = K_{p,cc2} = 1$ and the grid impedance is kept at 1.5mH. The phase margin

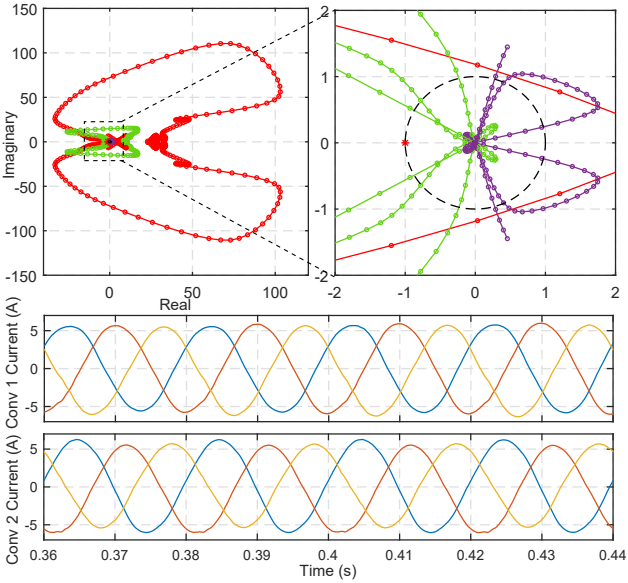

Figure 4.16: Study case 3: Stable operation of the multi-bus system for $K_{p,cc1} = K_{p,cc2} = 1$; λ_1 - red, λ_2 - green, λ_3 - violet

recorded for this configuration is 28.5 degrees as shown in Fig. 4.3. The gain of converter 1 is subsequently increased and it can be seen from 4.3 that the phase margin decreases significantly.

The Nyquist plot corresponding to the stable case of $K_{p,cc1} = K_{p,cc2} = 1$ is shown in Fig. 4.16.The time domain waveforms also confirm the stability of the system as no oscillatory modes are observed. In Fig. 4.16, it can be seen that λ_1 and λ_3 are far away from the critical point. However, as the gain increases, it is noticed that the eigen value loci of λ_1 intercepts the unit circle at reduced angles indicating a decrement in phase margin. At a gain of $K_{p,cc1} = 4$, $K_{p,cc2} = 2$, the system is barely stable with an extremely low phase margin and at a gain of $K_{p,cc1} = 5$, $K_{p,cc2} = 2$, the eigen value loci of λ_1 encircles the critical point indicating an unstable system as shown in Fig. 4.17.

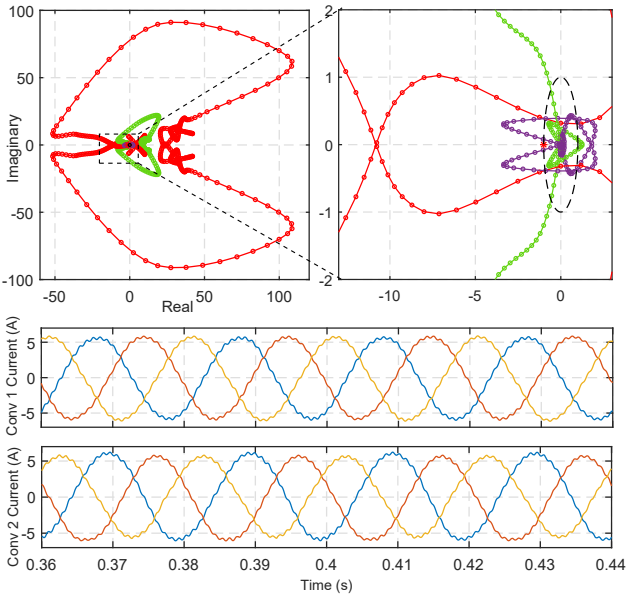

Figure 4.17: Study case 3: Unstable operation of the multi-bus system for $K_{p,cc1} = 5$ and $K_{p,cc2} = 2$; λ_1 - red, λ_2 - green, λ_3 - violet

To validate the above prediction, the system is connected as shown in Fig. 4.15 and the system started with low gains to have stable operation. In a step wise fashion, the gains are increased to the final values of $K_{p,cc1} = 5$, $K_{p,cc2} = 2$. It is observed that the harmonic stability occurs at 1.035 kHz as shown in Fig. 4.17.

4.5 Summary

This chapter proposes a non-parametric formulation of the NSC for a single bus system and extends the method to the multi-bus system. The proposed approach segregates active components and passive components in the network, and it is assumed that WFZ devices are present at the nodes with active components to measure the impedance of the

active components. A nodal admittance matrix approach is adopted to aggregate active component impedance measurements on a system level. A MIMO non-parametric formulation is obtained which maps the current injections of the active components to the node voltages where the active components are present. By applying the proposed non-parametric NSC for multi-bus system, the stability margins of the system can be computed. As the proposed method is invariant of topology, it is applicable to all types of grids. Since the nodes with power electronic converters with significant current injections are critical nodes, the required number of impedance measurement devices are significantly low. The proposed method is validated experimentally considering a single-bus system, a star-connected system, and a multi-bus test system. The experimental studies validate that locally measured converter impedances can be aggregated on a system level to make accurate predictions about system-level stability.

5

Advanced Virtual Output Impedance Shaping Control of Power Converters

5.1 Introduction

5.1.1 Motivation

Concerns about harmonic instabilities are rising in different sectors of the power grid. These resonances are observed in LV distribution grids with high RES penetration as well as in HV/MV systems such as wind and PV farms. With increased power-electronics-driven RES, the grid becomes weak and showcases large variations in grid impedance and loss of inertia. Furthermore, from experiments, it is clear that even minor background grid voltage distortions can significantly impact the current harmonics that power converters inject [37, 47, 48]. The terminal behavior of the converter is characterized by its output impedance, and thus the output impedance needs to be shaped to avoid resonance between the power converter and the grid. Since the grid impedance, as seen from the PCC, is changing due to changes in loads, topologies, and modifications to the operational modes of other converters in the grid, the harmonic resonance frequency is subject to change, and thus the developed damping solutions need to be adaptive. Furthermore, since the order of the grid impedance transfer function becomes difficult and may be impossible to predict, complex curve-fitting tools may produce erroneous transfer functions. Thus, such approaches cannot be used to design virtual impedance-shaping controllers. To overcome these difficulties, this dissertation proposes an adaptive Virtual Output Impedance (VOI) shaping controller that relies on non-parametric impedance measurements and harmonic stability monitoring. The key idea is to detect the critical

resonance frequency between the converter side and grid side using measurements and identify the bandwidth where damping needs to be applied.

5.1.2 State-of-the-art

VOI control has been used in the literature for various control objectives [17, 51, 52]. In the context of AC microgrids, particularly in grid-forming converters, VOI control loops are used in the outer loops to enable active and reactive power sharing among converters. The ratio of power sharing is dependent on the magnitude of the virtual impedance values used by every converter. These virtual impedance loops only modify the 50 Hz impedance due to their placement in the outer control loop. As harmonic instability occurs at super-synchronous frequencies, the VOI control is typically placed within the innermost control loops to modify the impedance behavior well above the fundamental frequency. AD approaches typically aim to damp the resonance frequency of the LCL filter by emulating passive damping elements that could be either connected across the filter capacitor or grid-side inductor. AD approaches use capacitor current or voltage feedback and typically require more measurements [83]. The approaches that emulate a damping resistor connected in series to the capacitor can help to damp the LCL filter resonance; however, they cannot be applied to damp inter-harmonic frequencies. Advanced AD controllers that emulate a trap filter are required to introduce damping at inter-harmonic frequencies. The measurement of grid current is sufficient to implement virtual damping, thus leading to a 2-DoF control structure. By using grid-current feedback for implementing virtual damping, additional measurements such as capacitor current or voltage measurements are avoided [84, 85]. Grid current measurement feed-forward through a bandpass filter leads to a bandstop command tracking characteristic, which is highly desirable [84, 86, 87]. Knowledge of grid impedance and the critical frequency is required to reshape the inverter output impedance [47, 49–51]. The measured grid impedance, which is non-parametric, is transferred into parametric form via complex curve fitting. However, the practicability of such approaches is limited [49, 51].

5.1.3 Main Contribution

Fig. 5.1 illustrates the proposed concept for measuring harmonic stability margins and mitigating resonances. This work proposes using parallel-connected WFZ monitoring equipment at the power plant's PCC. The WFZ device assesses the non-parametric impedance of the grid and converter [32, 33]. The impedance ratio (MLG) is estimated for each frequency, and the phase margin is calculated at the gain crossover frequency, which is also the critical frequency where the converter and grid impedance intersect.

The bandwidth signifies the frequency range centered around the critical frequency, where maintaining a phase difference between the grid and converter impedance below a predefined threshold is essential. This bandwidth, surrounding the critical frequency, is the key zone for implementing virtual damping. The non-parametric stability monitoring tool identifies both the critical frequency and bandwidth and passes this information to individual converters. The converters implement the damping through the proposed adaptive VDC, which is implemented as a digital IIR filter with adaptive parameters such as the critical frequency and bandwidth. Upon receiving the adaptive parameters from the monitoring tool, the controller swiftly adjusts the impedance within a brief interval of 1.5 times the sampling period. Additionally, the virtual damping control operates effectively with only grid current measurements, establishing a 2-DoF control structure. The proposed VDC is a type of VOI control since it actively modifies the closed-loop output impedance of the converter in the medium-frequency range with a specific objective of mitigating harmonic instabilities.

The contributions of this chapter are summarized as follows:

1. A non-parametric stability monitoring tool to identify critical frequency and bandwidth

2. An adaptive VDC

3. Experimental validation of the proposed method in the laboratory

5.2 Proposed Harmonic Stability Mitigation Strategy

5.2.1 Non-parametric Harmonic Stability Monitoring

This study proposes the utilization of a parallel-connected WFZ device at the PCC of the power plant, as illustrated in Fig. 5.1. Connecting the WFZ device to the PCC enables the measurement of grid-side impedance, converter impedance, and the Thevenin equivalent of the grid and converter-side impedances. To introduce perturbations into the PCC voltage, a wideband signal, such as a sum-of-sinusoids, is injected into the WFZ device duty cycle. Perturbation currents are consequently injected into the PCC, perturbing the PCC voltage based on the equivalent grid impedance. The impedances of the converter and grid are determined by measuring the converter current, grid current, and PCC voltage. To prevent the activation of strong non-linearities, a frequency resolution of 50 Hz is chosen. Using higher frequency resolutions such as 10 Hz or 5 Hz tends to increase the non-linear interactions, and thus they cannot be used to accurately extract the linear component. In such cases, the FCM has to be extracted by applying several rounds of perturbation, and the linear components are basically the diagonals of the obtained FCM. The MLG is defined as the ratio of the converter and grid impedance ($L = Y_{inv}Z_{grid}$) and it is calculated at each frequency. Subsequently, the MLG is interpolated to every 10 Hz using the cubic method to precisely determine the phase margin and the critical gain crossover frequency ω_c. The intersection of the impedance and admission magnitudes of the grid and inverter, as shown in Fig. 5.2 indicates the critical frequency ω_c. The phase difference between the inverter and the grid impedance is a crucial parameter, as depicted in Fig. 5.2. A phase difference close to or exceeding 180 degrees often leads to harmonic instability. Let us define the phase difference between the inverter and grid admittance as a function of frequency, as shown in (5.1).

$$\Delta\Phi(j\omega_i) = \phi\big(Y_{inv}(j\omega_i)\big) - \phi\big(Y_{grid}(j\omega_i)\big) \tag{5.1}$$

In (5.1), phase of the inverter admittance and grid admittance are $\phi(Y_{inv})$ and $\phi(Y_{grid})$ respectively. At the critical frequency ω_c, the phase margin of the grid-connected converter system in degrees is given by (5.2).

$$\Phi_{PM} = 180 - \Delta\Phi(j\omega_c) \tag{5.2}$$

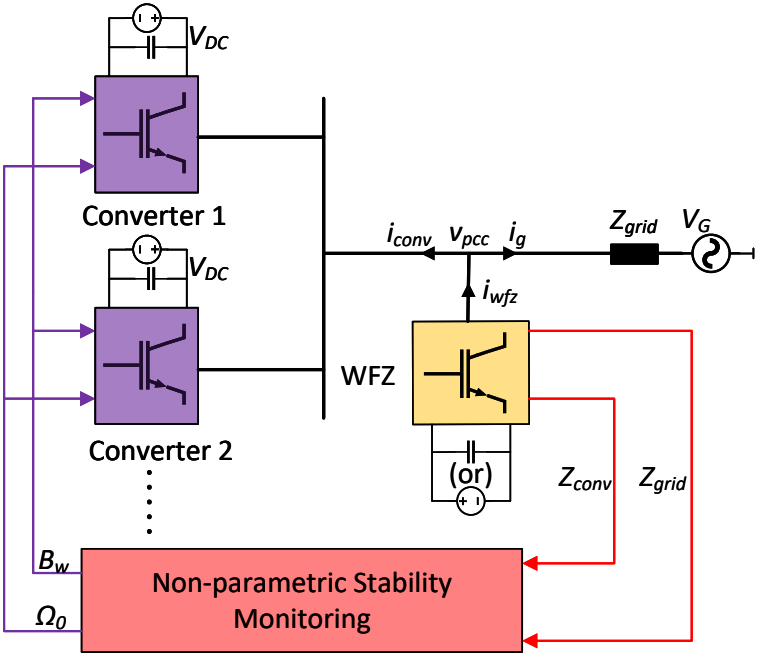

Figure 5.1: Schematic of the Proposed Monitoring Strategy

To ensure the stability of the grid-connected system and its robustness, a sufficient phase margin needs to be guaranteed at the critical frequency. Furthermore, since the critical frequency is subject to change as the grid impedance changes or the inverter control parameter changes, a maximum value of the phase difference between the converter and grid admittance ($\Delta\Phi_{max}$) is needed to guarantee stable and robust operation. This maximum phase value $\Delta\Phi_{max}$ basically upper bounds the phase difference between the converter admittance and grid admittance around the critical frequency as defined in (5.3).

$$\Delta\Phi(j\omega_i) < \Delta\Phi_{max} \tag{5.3}$$

The safe phase margins depend on the topology of the grid, the converter parameters and their control dynamics, cable parameters and lengths, and thus, the minimum phase margin needs to be fixed based on an offline stability analysis. As a rule of thumb, phase margins above 30 degrees ensure sufficient robustness without compromising the dynamics of the converter. This work assumes that such a safe minimum margin can be determined through offline analysis. A minimum phase margin $\Phi_{PM,min}$ is defined such that the maximum phase difference is calculated using (5.3).

$$\Delta\Phi_{max} = 180 - \Phi_{PM,min} \tag{5.4}$$

Frequency points ω_{c1} and ω_{c2} are identified where the specified maximum allowed phase difference condition in (5.3) fails. The frequency interval or bandwidth requiring damping application is consequently determined as $\omega_{c2} - \omega_{c1}$. Since the proposed virtual damping design has a symmetric frequency domain response with respect to the center frequency, the bandwidth $\mathcal{B}_w$ is chosen by the following conditions:

$$\mathcal{B}_w = \begin{cases} 2|\omega_{c1} - \omega_c|, & \text{if } |\omega_{c1} - \omega_c| > |\omega_{c2} - \omega_c| \\ 2|\omega_{c2} - \omega_c|, & \text{if } |\omega_{c2} - \omega_c| > |\omega_{c1} - \omega_c| \end{cases} \tag{5.5}$$

The non-parametric harmonic stability monitoring tool analyzes the impedance ratio to determine the critical frequency ω_c and the bandwidth $\mathcal{B}_w$ and sends this information to the local converters, which implement the proposed damping.

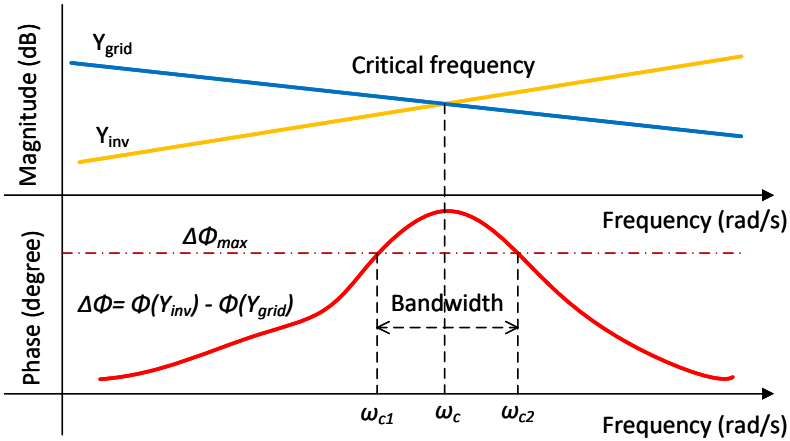

Figure 5.2: Non-parametric harmonic stability analysis

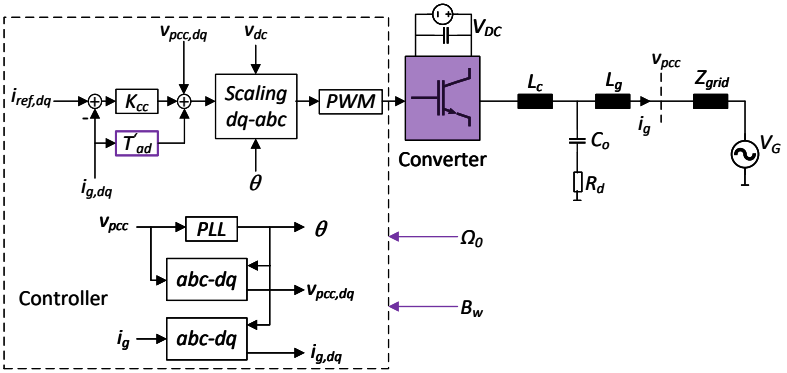

Figure 5.3: Proposed 2-DOF Virtual Damping Control Structure

5.2.2 Virtual Damping Control Design

Harmonic instability arises from the low or negative phase margin at the critical frequency, where the magnitude of the impedance of the converter and the equivalent grid impedance coincide, as previously explained. Fig. 5.3 illustrates the generic inner control structure of the grid-connected converter. The traditional control structure comprises a SRF-PLL intended to monitor the phase of the PCC voltage and a current controller K_{cc} implemented in the dq domain. Minimal measurements are required to attain harmonic damping at the identified critical frequency, as the grid current measurement is sufficient. Active damping strategies that rely on capacitor current or voltage feedback are widely proposed; however, grid current feedback is the subject of only a limited number of research studies. A measurement feed-forward transfer function T_{ad} is proposed to form a 2-DoF control structure, which is illustrated in Fig. 5.3. Assigning a bandpass filter to T_{ad} is necessary to induce bandstop behavior in the injected grid current. In the following analysis, we shall investigate a second-order bandpass denoted as (5.6), where $\mathcal{B}_w$ represents the bandwidth and Ω_0 signifies the center bandstop frequency.

$$T_{ad}(s) = \frac{\mathcal{B}_w s}{s^2 + \mathcal{B}_w s + \Omega_0^2} \tag{5.6}$$

The absolute frequency interval between the two passband frequencies is denoted by the bandwidth $\mathcal{B}_w$. The two passband frequencies at which T_{ad} crosses -3dB are symmetric with respect to Ω_0. The bandwidth expressed in terms of quality factor is $\mathcal{B}_w = \frac{\Omega_0}{Q}$.

Implementing the filter as an IIR digital filter involves applying a Tustin transformation $s = \frac{2}{T_s}\frac{z-1}{z+1}$ to (5.6), resulting in the following IIR filter:

$$T_{ad}(z) = \frac{n_0 + n_2 z^{-2}}{d_0 + d_1 z^{-1} + d_2 z^{-2}}, \tag{5.7}$$

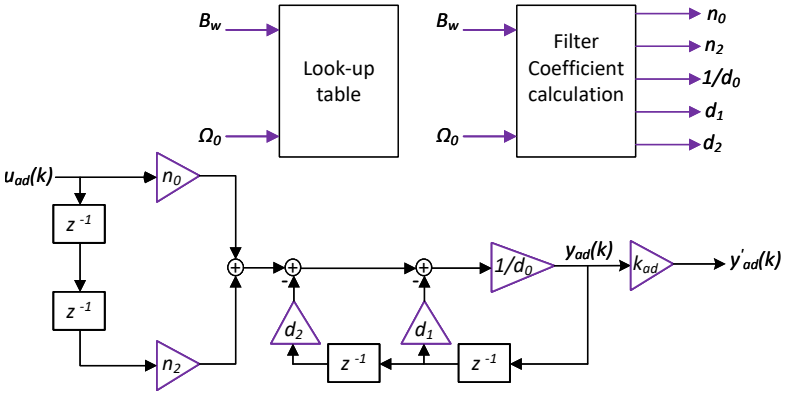

Figure 5.4: Proposed adaptive filter realization

where the derived filter coefficients are provided in (5.8)-(5.12) and T_s is the sampling and PWM frequency of the converter.

$$n_0 = 2\mathcal{B}_w T_s \tag{5.8}$$

$$n_2 = -2\mathcal{B}_w T_s \tag{5.9}$$

$$d_0 = 4 + 2\mathcal{B}_w T_s + (\Omega_0 T_s)^2 \tag{5.10}$$

$$d_1 = 2(\Omega_0 T_s)^2 - 8 \tag{5.11}$$

$$d_2 = 4 - 2\mathcal{B}_w T_s + (\Omega_0 T_s)^2 \tag{5.12}$$

Considering u_{ad} and y_{ad} as the input and output of the damping controller, the following difference equation can be obtained:

$$y_{ad}(k) = \frac{1}{d_0}\big(n_0 u(k) + n_2 u(k-2) - d_1 y(k-1) - d_2 y(k-2)\big) u_{ad}(k) \tag{5.13}$$

The practical implementation of the intended IIR filter defined in (5.13) is illustrated in Fig. 5.4. The coefficients of the IIR filter are determined by Ω_0 and $\mathcal{B}_w$, allowing (5.13) to operate as an adaptive bandpass filter with tunable input parameters Ω_0 and $\mathcal{B}_w$. The center frequency Ω_0 and the frequency range $\mathcal{B}_w$ where damping is needed are defined using

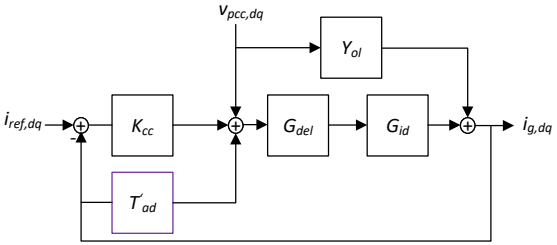

Figure 5.5: Control block diagram

non-parametric stability monitoring. A gain parameter k_{ad} is introduced to control the overall damping T'_{ad}, where $T'_{ad} = k_{ad}T_{ad}$.

In the diagram presented in Fig. 5.5, we shall examine the control block diagram of the grid-connected converter. In this diagram, the current control transfer function is denoted as G_{id}, the delay is represented by G_{del}, and the open-loop admittance of the converter is denoted as Y_{ol}. The closed-loop admittance TF and reference tracking TF, which account for the damping controller, are derived through block-reduction methods and are denoted as (5.14) and (5.15), respectively.

$$T_{CL} = \frac{G_{id}G_{del}K_{cc}}{1 + G_{id}G_{del}(K_{cc} - T'_{ad})} \tag{5.14}$$

$$Y_{CL} = \frac{Y_{ol} + G_{id}G_{del}}{1 + G_{id}G_{del}(K_{cc} - T'_{ad})} \tag{5.15}$$

By utilizing the transfer functions (5.14) and (5.15), the closed-loop system stability can be examined, and the impact of control delay (G_{del}) and the virtual damping controller T'_{ad} [88] can be investigated. The proposed second-order virtual damper can be cascaded to attenuate multiple resonance frequencies. This enables the regulation of attenuation independently for every resonance frequency. An alternate method is to use a single-stage filter with a wide bandwidth, wherein the center frequency is chosen such that sufficient attenuation is obtained at both resonance frequencies. This will increase the robustness of the damping controller, especially when grid impedance changes.

Table 5.1: Parameters used in experiment

Parameters	Values
Switching frequency	20 kHz
Inverter side inductor (r_c, L_c)	0.2 Ω, 2.3 mH
Grid side inductor (r_g, L_g)	0.2 Ω, 2.4 mH
Filter capacitances	10 μF
Damping resistor	1 Ω
Current control (WFZ)	$K_p = 0.01$, $K_i = 2$
Grid impedance branch	$R_{grid} = 0.3$ Ω , $L_{grid} = 1.5$ mH

Look-up table for k_{ad}

The parameter k_{ad} has a significant influence on the standalone stability of the converter. Each converter needs to determine the gain k_{ad} such that all poles of T_{CL} lie within the unit circle and the phase margin of the loop transfer function $G_{id}G_{del}(K_{cc} - T'_{ad})$ is around 60 degrees for sufficient dynamic response and robustness. The determination of optimal gain k_{ad} can be performed offline, and a look-up table is created to determine the optimal k_{ad} based on $\mathcal{B}_w$ and Ω_0. For a given $\mathcal{B}_w$ and Ω_0, as k_{ad} is increased, it can be noted that the phase margin of loop transfer function of converter reduces. The optimal k_{ad} value corresponds to a phase margin of 60 degrees for the loop transfer function. k_{ad} can be further increased without losing stability; however, under such conditions, the margins are too low and could lead to instability due to a lack of robustness. Increasing k_{ad} arbitrarily high moves a conjugate pole pair of T_{CL} to the RHP, causing instability. Thus, based on a desirable phase margin, the optimal value of k_{ad} can be obtained offline for each Ω_0 and $\mathcal{B}_w$ value. Thus, a look-up table is formulated for each grid-connected converter with inputs Ω_0 and $\mathcal{B}_w$ and the output as optimal k_{ad}.

5.3 Experimental Verification

5.3.1 Description of Setup

Fig. 5.6 shows the picture of the laboratory setup, which consists of two identical three-phase LCL-filtered converters connected in parallel, and

Figure 5.6: Experimental setup

each converter is powered by a separate DC power supply. One of the converter is configured as the WFZ device, and the other is configured as the main converter. The converter setup is implemented using the Imperix rapid prototyping system. A passive RL grid impedance connects the parallel-connected converters to the Chroma 618300 grid emulator. Table 5.1 provides the parameters pertaining to the experimental setup. The test setup is run with a nominal current of 5A and a line-neutral voltage of 100V RMS and the DC side voltage is set to 370V. The WFZ device under nominal operation injects quasi-zero current, with the exception of injecting noise currents to measure the impedance of the grid and converter. Sum-of-sinusoid perturbation signal with identical amplitude at each frequency are superimposed over the duty cycle of the WFZ device to inject perturbation currents. Simultaneous injection of frequencies within the range 100 Hz to 1.5 kHz is performed with a resolution of 50 Hz. Using offline optimization, the phase of each sinusoidal component is optimized to keep the peak-peak amplitude low.

5.3.2 Influence of Control Parameters

The influence of k_{ad} on the impedance shaping and stability is depicted in Fig. 5.7. Fig. 5.7a depicts the measured admittance magnitude and phase on the grid side and converter side. $\mathcal{B}_w = 0.5$ kHz and $\Omega_0 = 1.35$ kHz are fixed as constants during these measurements to strictly study the influence of k_{ad}. Note that $\mathcal{B}_w$ and Ω_0 to be utilized in the filter design have units of rad/s but the unit Hz is used in the experimental section and in the graphs for easier visualization. The converter impedance is measured experimentally for 4 cases, with the values of k_{ad} as 0, 2.5, 10 and 20. From Fig. 5.7a, notice that the amplitude and phase of converter admittance decrease with increasing k_{ad}, resulting in a reduced phase difference between converter and grid admittance at the critical frequency. As seen in Fig. 5.7b, the stability margins are rather small when no virtual damping control is activated due to the substantial phase difference between the grid and converter admittance, and the phase margins increase significantly with an increase in k_{ad}. The intersection of the Nyquist plots with the unit circle is seen in the zoomed part of Fig. 5.7b.

When the converter receives a new set of Ω_0 and $\mathcal{B}_w$, it must size k_{ad} to place stable poles in the closed-loop transfer function since increasing

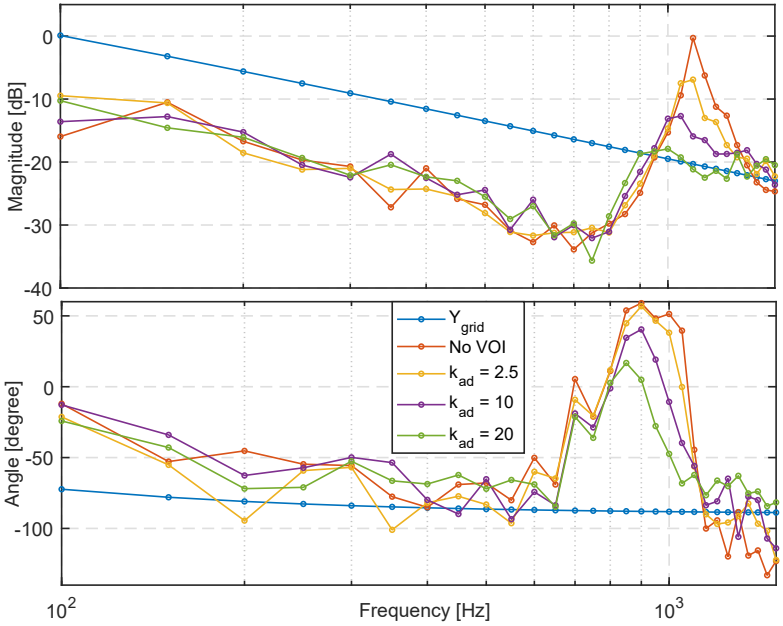

(a) Influence of k_{ad}

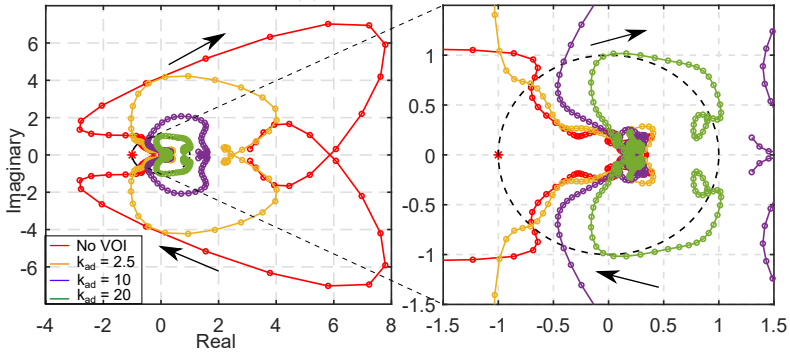

(b) Nyquist stability criterion for different k_{ad}

Figure 5.7: Impedance Shaping through k_{ad}

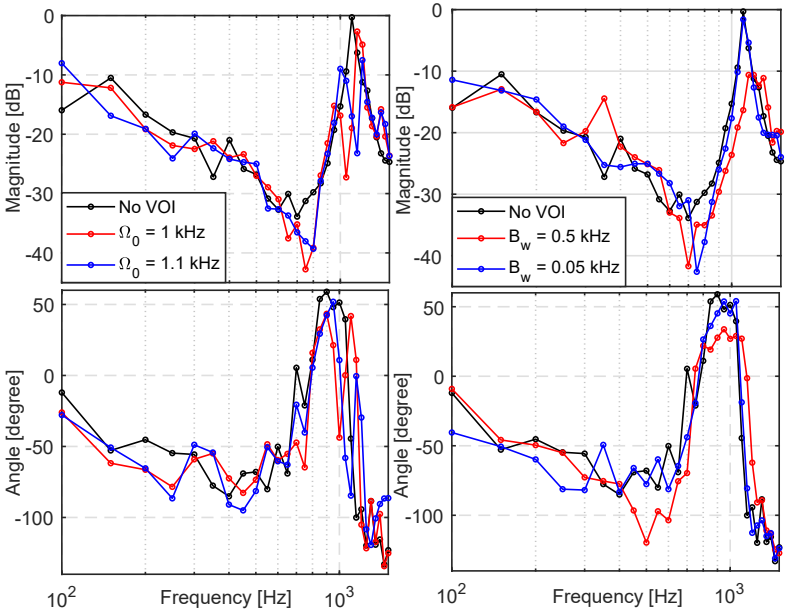

(a) Influence of Ω_0 (b) Influence of $\mathcal{B}_w$

Figure 5.8: Impedance Shaping through Ω_0 and $\mathcal{B}_w$

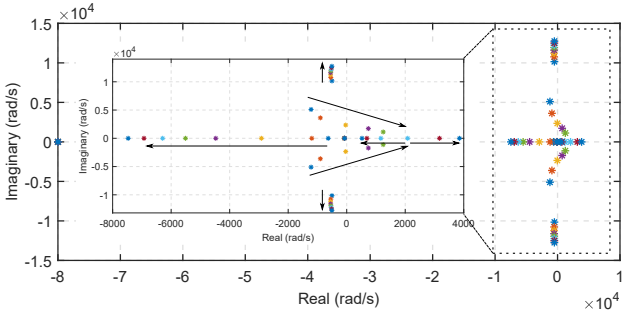

Figure 5.9: Influence of increasing k_{ad} on the pole locations of $T_{CL,AD}$

k_{ad} arbitrarily would cause the converter to become unstable. Choosing low values of k_{ad} might not provide adequate damping, due to which the harmonic instability could persist. The influence of increasing k_{ad} on the closed-loop pole locations of $T_{CL,AD}$ is shown in Fig. 5.9. It can be noted that as k_{ad} is increased, the dominant pole of $T_{CL,AD}$ which lies on the Left Half Plane (LHP) real axis, moves to the left, indicating faster system dynamics. There are 2 sets of complex conjugate pairs of eigenvalues, each with a different influence from the increment of k_{ad}. As shown in Fig. 5.9, one complex conjugate eigenvalue has a negative real part, and the imaginary part increases as k_{ad} is increased, thus it does not contribute to instability. As observed in Fig. 5.9, the other set of complex conjugate eigenvalues moves to the RHP as k_{ad} is increased and thus contributes to instability. In summary, increasing k_{ad} improves the transient damping response; however, there is a hard upper limit on k_{ad} since one of the complex conjugate pole pairs moves to the RHP.

It is essential to establish the influence of k_{ad} on the phase margin of the loop transfer function, particularly for different pairs of Ω_o and $\mathcal{B}_w$. Fig. 5.10 shows the influence of k_{ad} on the phase margin for different pairs of Ω_o and $\mathcal{B}_w$. It can be seen that the phase margin decreases with an increase in k_{ad}. Since the loop transfer function is dependent on converter hardware parameters and inner current control parameters, which are fixed values for a given converter, an optimal gain can be determined for every Ω_o and $\mathcal{B}_w$ pair offline. By choosing the desired phase margin for the loop transfer function, the optimal gain can be determined by increasing k_{ad}. In this

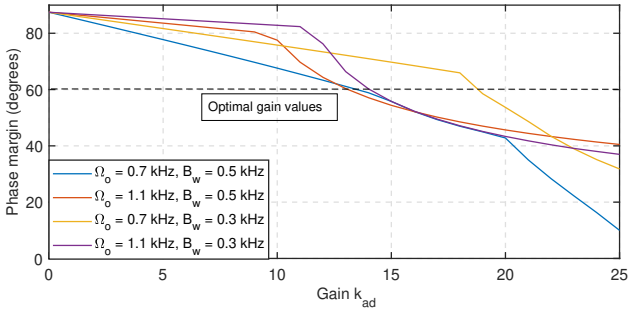

Figure 5.10: Phase margin of loop transfer function dependency on k_{ad} for different set of Ω_0 and $\mathcal{B}_w$

work, the desired phase margin for loop transfer function is considered to be 60 degrees, and thus, as shown in Fig. 5.10, the optimal k_{ad} values are determined for an exemplary set of Ω_o and $\mathcal{B}_w$. The aforementioned process is repeated for several sets of Ω_o and $\mathcal{B}_w$ pairs to determine the $k_{ad,opt}$ to be used, and thus a lookup table is formulated. Fig. 5.11 shows the $k_{ad,opt}$ obtained as a function of Ω_o and $\mathcal{B}_w$. Using the aforementioned procedure, each converter manufacturer can generate a lookup table for each converter offline. In operation, the converters can automatically select the optimal k_{ad} based on Ω_o and $\mathcal{B}_w$ published by the centralized monitoring system.

Ω_0 and $\mathcal{B}_w$ can be used to achieve impedance shaping, as seen in Fig. 5.8. As explained previously, Ω_0 influences the center frequency where the VDC provides the highest attenuation, and $\mathcal{B}_w$ determines the width of the attenuation. To study the impact of Ω_0 on the closed-loop admittance shaping, $\mathcal{B}_w$ and k_{ad} are fixed as constants. A high quality factor is attained by fixing $\mathcal{B}_w$ to 0.05 kHz, and k_{ad} is selected to be 20. Fig. 5.8a clearly illustrates enhanced damping at the appropriate frequencies of Ω_0 = 1 and 1.1 kHz when compared to admittance measured with no VOI case.

The influence of $\mathcal{B}_w$ in shaping the inverter admittance is studied by fixing Ω_0 and k_{ad}. The impedance of the converter is measured by fixing $\Omega_0 = 0.7$ kHz and $k_{ad} = 10$ and the two values of the bandwidth considered are $\mathcal{B}_w = 0.5$ kHz and $\mathcal{B}_w = 0.05$ kHz. While $\mathcal{B}_w = 0.05$ kHz

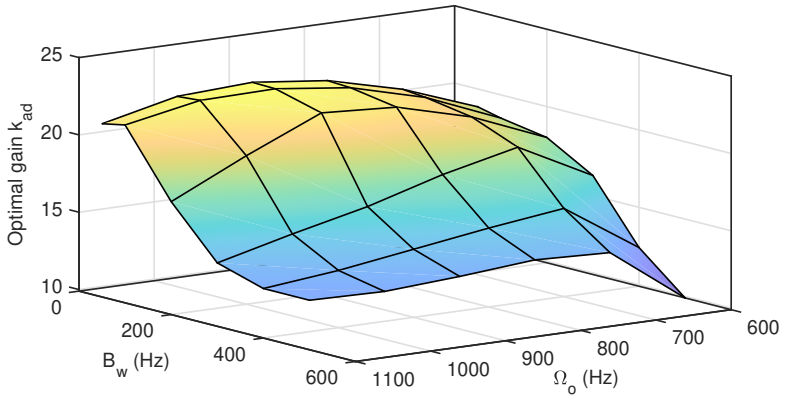

Figure 5.11: Optimal gain k_{ad} dependency on Ω_0 and $\mathcal{B}_w$

clearly exhibits damping at the intended frequency of 0.7 kHz, as observed in Fig. 5.8b, admittance measured with $\mathcal{B}_w = 0.5$ kHz shows damping over a wide range of frequencies. The case corresponding to $\mathcal{B}_w = 0.05$ kHz shows damping at $\Omega_0 = 0.7$ kHz and follows the trend of the no VOI case at other frequencies. With $\mathcal{B}_w = 0.5$ kHz, both magnitude and phase are significantly modified around the center frequency $\Omega_0 = 0.7$ kHz. Thus, using a wider bandwidth parameter enables damping at a wide range of frequencies, which increases the robustness of the converter to grid impedance variations.

5.3.3 Transient Damping Tests

To drive the system toward harmonic instability, the proportional gain of the PI current controller is set at $K_p = 5.5$. Without a VOI controller, the system is unstable for the setup shown above. The above condition has been experimentally verified. As the grid current indicates that the harmonic instability happens at 1.35 kHz, $\Omega_0 = 1.35$ kHz is chosen, and $\mathcal{B}_w = 0.5$ kHz is chosen for its strong robustness against grid impedance fluctuation. As seen in Fig. 5.12, a number of tests are carried out to evaluate the transient response introduced by the damping controller. A very stable condition is reached when $k_{ad} = 20$. When

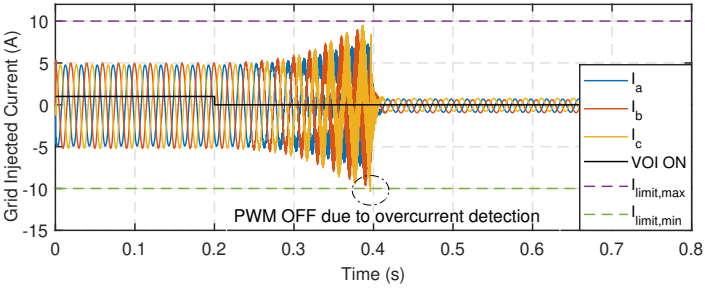

(a) $k_{ad} = 20$ with VOI switch-OFF at $t = 0.2s$

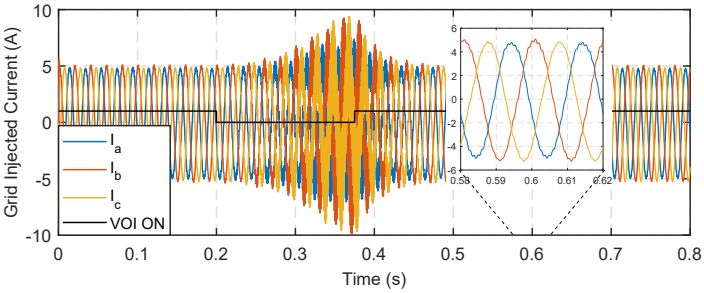

(b) $k_{ad} = 2.5$ with VOI transitions at $t = 0.2s$ and $t = 0.38s$

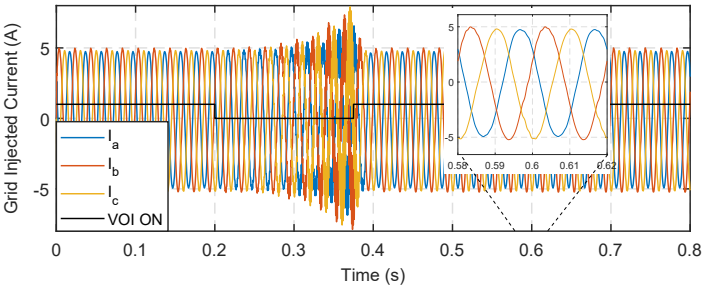

(c) $k_{ad} = 20$ with VOI transitions at $t = 0.2s$ and $t = 0.38s$

Figure 5.12: Transient damping test

the controller is deactivated by setting $k_{ad} = 0$, the harmonic currents increase exponentially until the 10A current magnitude limit is exceeded. As seen in Fig. 5.12a, the user-defined fault condition disables the PWM, safeguarding the converter. The small currents that are noticed past the deactivation of PWMs are the currents delivered from the grid emulator to the exposed LC stage of the LCL-filtered converter. A timed turn-off and turn-on of the VOI control is carried out, taking into account $k_{ad} = 2.5$ and $k_{ad} = 20$, as seen in Figs. 5.12b and 5.12c to study the transient behavior of damping. The harmonic instability occurs when the VOI is turned off, and the damping starts as soon as the VOI is turned on. When comparing Figs. 5.12b and 5.12c, it can be observed that the damping controller constructed with $k_{ad} = 20$ recovers faster than the one with $k_{ad} = 2.5$. Moreover, steady harmonic oscillations are seen in the zoomed area of Fig. 5.12b, but there are no such harmonics in the currents in Fig. 5.12c. Harmonic stability analysis needs to be performed by measuring the impedance of the converter and grid to determine the stability and margins for both $k_{ad} = 2.5$ and $k_{ad} = 20$.

As seen in Fig. 5.13, the non-parametric Nyquist stability criterion is applied, and the impedance of the converter is measured for both configurations to confirm this observation. The case where $k_{ad} = 2.5$ results in an encirclement around the critical point that indicates an unstable interconnection; in contrast, $k_{ad} = 20$ is stable and has a phase margin of 29.4 degrees, confirming the finding from the time-domain response. Thus, low and high values of k_{ad} when chosen arbitrarily can lead to instabilities. Inadequate damping causes instability with low values of k_{ad}, while in the case of high values of k_{ad}, the placement of RHP poles in the closed-loop transfer function of the converter results in instability. The optimal damping gain calculated from the look-up table ensures that sufficient damping is obtained and a healthy phase margin is maintained for the local converter.

5.4 Summary

A non-parametric method for monitoring and mitigating harmonic instabilities in renewable-based power plants is presented in this chapter. The proposed method consists of a centralized non-parametric harmonic stability monitoring algorithm and a decentralized virtual damping solution. At the terminal of the power plant, a WFZ device is connected,

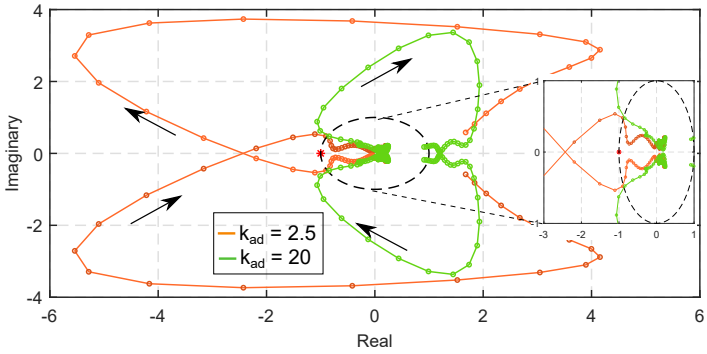

Figure 5.13: Comparison of Nyquist stability criterion for $k_{ad} = 2.5$ and 20

which measures the impedance of the grid and the equivalent impedance of the power plant. From the ratio of the impedances, the critical frequency (Ω_0) at which damping is required is determined. By defining a maximum value of the phase difference between the converter and grid admittance ($\Delta\Phi_{max}$), two corner frequencies between which the maximum phase condition fails are identified, and thus the required bandwidth $\mathcal{B}_w$ is determined. Taking into account the critical frequency and bandwidth identified by the stability monitoring tool, an adaptive VDC is proposed. The proposed virtual damper does not require any additional measurements and requires only the grid current measurement, which is also required by the inner current controller. A second-order bandpass filter realized as an IIR filter is proposed for the virtual damper. The coefficients are derived as a function of Ω_0 and $\mathcal{B}_w$. A $2-$DoF control structure is obtained wherein the proposed virtual damper feed-forwards the measured grid current. To ensure standalone stability, each converter must independently determine the damping gain k_{ad}. This work proposes an offline look-up table design where the optimal gain $k_{ad,opt}$ is calculated based on Ω_0 and $\mathcal{B}_w$. Through an experimental setup, the proposed method is validated for a wide range of operating conditions. The impact of the control parameters on the shaping of impedance is studied. By examining the impact of control parameters,

large values of bandwidth $\mathcal{B}_w$ are advised to increase robustness against abrupt grid impedance variations. The stability margin of converter-grid interconnection is greatly increased by the proposed VDC, and in terms of dynamics, the proposed method achieves fast recovery from harmonic instability conditions.

6

Conclusion and Future Work

6.1 Conclusion

Harmonic instabilities are constantly arising in different sectors of the power grid and these phenomena are observed over a wide frequency range. With increased power-electronics-driven RES, the grid becomes weaker and showcases large variations in grid impedance and loss of inertia. Harmonic stability is characterized as an impedance-based phenomenon, and there are some major challenges to solving this problem. Converter manufacturers or vendors protect their hardware and control algorithms with IPR and thus grid operators cannot rely on parametric approaches, which are well known.

Furthermore, when local impedance information is available, it is not clear how the locally measured converter impedances can be aggregated on a system level to make system-level predictions of stability.

This dissertation was dedicated to solving this problem, and in this regard, this dissertation has 4 unique contributions:

1. A standalone WFZ device and its uncertainty characterization
2. A WFZ device-based FCM extraction method and its uncertainty characterization
3. A non-parametric harmonic stability monitoring method for multi-bus power system
4. An advanced VDC for grid-connected power electronic converters

The conclusions specific to each contribution are covered below:

6.1.1 A Standalone WFZ Device and its Uncertainty Characterization

This work describes a standalone WFZ device that can measure non-parametric grid impedance under steady-state conditions without requiring grid interruption. Operational sequences for the WFZ device are proposed, and also the uncertainty characterization methods for determining the accuracy of such wideband impedance measuring devices are discussed.

To enable the WFZ device for *dq* impedance extraction, two operational sequences are proposed: sequential and parallel. Considering the same frequency resolution, the parallel method is almost twice as fast as the sequential method. In terms of accuracy and THD, for a given amplitude of perturbation, the sequential method on an average provides around 50% reduction in the mean absolute error and lower THD levels than the parallel method, showing higher accuracy. The requirements of PRBS amplitude in relation to the minimum impedance magnitude to be measured are also studied in this research. The choice of the PRBS amplitude is a trade-off between absolute error and THD needs, since larger impedances may be extracted with lower absolute error and higher THD levels for a given PRBS amplitude.

A low voltage prototype of the WFZ device is built, and the extraction of impedance is experimentally demonstrated. This work presents two techniques for characterizing of wideband impedance measurement devices. Wideband characterization determines the overall accuracy of the device, whereas per-frequency characterization calculates uncertainty at each frequency.

The PRBS is suitable for extraction of linear impedances. For power converters, extracting linear component of impedance with PRBS is error-prone since there is significant coupling between high-frequency and low-frequency components. Thus, utilization of sum-of-sinusoid as an excitation signal is recommended for measuring the linear impedance component of power converters. With sum-of-sinusoid, the maximum frequency of injection and the frequency resolution can be chosen such that the frequency coupling effects are minimal and thus the impedance accuracy is improved. The accuracy is still not high since there are still frequency coupling effects which are not considered in the linear impedance extraction, and thus it is recommended to extract the FCM.

The diagonal of the FCM provides an improved representation of the linear component of power converter impedance.

6.1.2 A WFZ Device based FCM Extraction Method and its Uncertainty Characterization

A wideband excitation technique-based FCM measurement method for power electronic converters is proposed in this work. The proposed technique is suitable for both laboratory and field measurement, in contrast to the previously suggested FCM measuring techniques, which are primarily intended for laboratory measurements.

The utilization of sum-of-sinusoids is recommended in this work, wherein meta-heuristic algorithms can optimize the phase of each harmonic offline, which reduces the peak-to-peak amplitude of the perturbation. The FCM is extracted by solving a least-square estimate technique after numerous rounds of wideband perturbation application. The FCM model of the power converter can be modified from the generalized FCM model based on the interactions between the AC and DC sides as well as between phases. The equivalent FCM of the grid and DUT can be measured by measuring the WFZ injected current. Potential frequency points that can cause harmonic resonances between the grid and DUT can be accessed, as shown by simulation scenarios. The FCM diagonal and off-diagonal components are considerably altered by changes to the inner control loop.

Additionally, characterization parameters are proposed in this work for evaluating FCM accuracy. The per-frequency MAE shows the accuracy of the FCM as a function of frequency, while the MAE indicates the overall accuracy of the model, taking into account all frequency points of interest. The NLI, which is demonstrated to be a measure of the strength of non-linearity, can be used to evaluate the diagonal dominance of the extracted FCM.

6.1.3 A Non-parametric Harmonic Stability Monitoring Method for Multi-bus Power System

This work proposes a non-parametric formulation of the NSC for a single bus system and extends the method to the multi-bus system. The proposed approach segregates active components and passive components

in the network, and it is assumed that WFZ devices are present at the nodes with active components to measure the impedance of the active components. A nodal admittance matrix approach is adopted to aggregate active component impedance measurements on a system level. A MIMO non-parametric formulation is obtained which maps the current injections of the active components to the node voltages where the active components are present. As the proposed method is invariant of topology, it is applicable to all types of grids. Since the nodes with power electronic converters are critical nodes, the required number of impedance measurement devices is significantly low. The proposed method is validated experimentally considering a single-bus system, a star-connected system, and a multi-bus test system. The experimental studies validate that locally measured converter impedances can be aggregated on a system level to make accurate predictions about system-level stability.

It is identified that the grid impedance and inner control loop parameters can affect the critical resonance frequency. The proposed impedance scanning and stability monitoring algorithm enables the calculation of stability margins, thereby enabling constant monitoring of the stability of the power grid.

6.1.4 Advanced Virtual Damping Control Strategy for Grid-connected Power Electronic Converters

A non-parametric method for monitoring and mitigating harmonic instabilities in renewable-based power plants is presented. The proposed method consists of a centralized non-parametric harmonic stability monitoring algorithm and a decentralized virtual damping solution.

The centralized monitoring identifies the critical frequency at which damping is required along with the bandwidth. By defining a maximum value of the phase difference between the converter and grid admittance, the bandwidth is determined.

An adaptive VDC is proposed that requires only the grid-feed current, and thus a 2-DoF control structure is achieved. The controller coefficients are updated based on the center frequency and bandwidth published by the centralized monitoring system.

Through an experimental setup, the proposed method is validated for a wide range of operating conditions. The impact of the control parameters

on the shaping of impedance is studied. By examining the impact of control parameters, large values of bandwidth are advised to increase robustness against abrupt grid impedance variations. The stability margin of converter-grid interconnection is significantly increased by the proposed VDC, and in terms of dynamics, the proposed method achieves fast recovery from harmonic instability conditions.

6.2 Future Work

Since this dissertation has two aspects, the possible future extension and scope pertaining to each aspect are covered below:

6.2.1 Measurement Aspect

- To access how often and how dynamically the grid impedance changes, field application of impedance measurement devices could be beneficial. In this vein, continuous monitoring and measurement of grid impedances would pave the way towards developing proper timing of harmonic stability monitoring schemes, and also such impedance data is useful for testing of power converters. Field application of such devices also enables the study of perturbation magnitudes that are required, its impact on measurement accuracy, and THD

- Conducting a comparative analysis of FCM models, and NPHD models are necessary in terms of modeling complexity and accuracy

6.2.2 Control and Stability Aspect

- Investigation of the proposed non-parametric NSC for a larger system would be beneficial, and furthermore, considering different GFMs, GFLs and rectifier types would be required to study the effectiveness of the proposed approach and identify the required modifications

- Investigation of methods to aggregate system-level dynamics using FCM to consider frequency coupling effects and compare the performance of FCM and linear stability analysis. FCM based stability monitoring tools can potentially enable detection

of harmonic instability occurrences due to frequency coupling phenomenon

- Examining the role of smart active damping and impedance cancellation devices. Investigate methodologies on how to integrate wideband impedance measurement and smart active damping functionalities in one device since their control philosophies may diametrically oppose each other. WFZ devices ideally require low control bandwidth, whereas smart AD devices require fast bandwidth

Curriculum Vitae

Sep 2024 - Present	Senior Electrical Engineer RWE Technology International GmbH Essen, Germany
July 2017 - Aug 2024	Research Associate and Doctoral Candidate Institute for Automation of Complex Power System RWTH Aachen University, Germany
Mar 2017 - Jun 2017	Scientific Help (WiHi) Institute for Automation of Complex Power System RWTH Aachen University, Germany
Nov 2015 - May 2015	Internship SMA Solar Technology AG, Niestetal, Germany
Oct 2014 - Mar 2017	M.Sc. Electrical Power Engineering RWTH Aachen University, Aachen, Germany
Jul 2010 - May 2014	B.Tech Electrical and Electronics Engineering SRM University, Chennai, India
June 2008 - Mar 2010	All India Senior Secondary Examination (AISSE) Modern Senior Secondary School, Chennai, India
Feb 12 1992	born in Thanjavur, India

List of Acronyms

PV Photovoltaic 1, 141

PWM Pulse Width Modulation 21

RES Renewable Energy Sources 1

RHP Right Half Plane 83

ROA Region of Attraction 15

ROCOF rate-of-change of frequency 2

SG Synchronous Generator 5

SRF Synchronous Reference Frame 21

THD Total Harmonic Distortion 10

TSO Transmission System Operator 5

VDC Virtual Damping Controller 9

VFD Variable-Frequency Drive 49

VOI Virtual Output Impedance 107

VSC Voltage Source Converter 5

VSM Virtual Synchronous Machine 2

WF Wind Farm 5

WFZ Wideband-frequency Impedance 8

WT Wind Turbine 4

List of Figures

List of Tables

List of Algorithms

Bibliography

[1] *Public Net Electricity Generation 2023 in Germany: Renewables Cover the Majority of German Electricity Consumption for the First Time*. Fraunhoffer ISE. URL: https://www.ise.fraunhofer.de/en/press-media/press-releases/2024/public-electricity-generation-2023-renewable-energies-cover-the-majority-of-german-electricity-consumption-for-the-first-time.html.

[2] *Greenhouse Gas Emission Inventory & Calculation Methodology*. RWE AG. URL: https://www.rwe.com/en/responsibility-and-sustainability/#reports.

[3] *Renewable Energy Sources Act (EEG 2017)*. Federal Ministry of Economic Affairs and Climate Action (BMWK). URL: https://www.bmwk.de/Redaktion/EN/Downloads/renewable-energy-sources-act-2017.html.

[4] *Recent Facts about Photovoltaic in Germany*. Fraunhoffer ISE. URL: https://www.ise.fraunhofer.de/en/publications/studies/photovoltaics-report.html.

[5] B. Bayer and A. Marian. "Innovative measures for integrating renewable energy in the German medium-voltage grids". In: *Energy reports* 6 (2020), pp. 336–342. DOI: https://doi.org/10.1016/j.egyr.2019.12.028.

[6] P. Christensen et al. *High penetration of power electronic interfaced power sources and the potential contribution of grid forming converters*. ENTSO-E. 2020. URL: https://consultations.entsoe.eu/system-development/entso-e-connection-codes-implementation-guidance-d-3/user_uploads/igd-high-penetration-of-power-electronic-interfaced-power-sources.pdf.

[7] *The massive integration of power electronic devices (MIGRATE) project*. Project MIGRATE. URL: https://cordis.europa.eu/project/id/691800/results.

[8] *stoRE - Final Publishable Report*. Project stoRE. URL: https://www.bmwk.de/Redaktion/EN/Downloads/renewable-energy-sources-act-2017.html.

[9] *D3.3 Power electronics System-level stability criteria*. Project RESERVE. URL: https://www.re-serve.eu/deliverables.html.

[10] *D3.5 Specification for an on-line system level monitoring system*. Project RESERVE. URL: https://www.re-serve.eu/deliverables.html.

[11] A. Monti, R. Uhl, and S. K. Gurumurthy. "Vorrichtung zur Emulation eines Versorgungsnetzes zur Validierung von Komponenten eines Stromversorgungssystems". DE102019217291A1. May 2021. URL: https://worldwide.espacenet.com/patent/search/family/073198313/publication/DE102019217291A1?q=pn%3DDE102019217291A1.

[12] S. K. Gurumurthy et al. "Load Bus Frequency Estimation in Converter-Driven Grids-A Dynamic Phasor Approach". In: *IEEE Transactions on Power Systems* (2023). DOI: 10.1109/TPWRS.2023.3334194.

[13] F. Milano and A. Ortega. "Frequency divider". In: *IEEE Transactions on Power Systems* 32.2 (2016), pp. 1493–1501. DOI: 10.1109/TPWRS.2016.2569563.

[14] J. Ainsworth. "Harmonic instability between controlled static convertors and ac networks". In: *Proceedings of the Institution of Electrical Engineers*. Vol. 114. 7. IET. 1967, pp. 949–957. DOI: https://doi.org/10.1049/piee.1967.0182.

[15] P. Hazell and J. Flower. "Theoretical analysis of harmonic instability in ac-dc convertors". In: *Proceedings of the Institution of Electrical Engineers*. Vol. 117. 9. IET. 1970, pp. 1869–1878. DOI: https://doi.org/10.1049/piee.1970.0333.

[16] G. Lemieux. "Power system harmonic resonance-a documented case". In: *IEEE Transactions on Industry Applications* 26.3 (1990), pp. 483–488. DOI: 10.1109/ICHQP.2014.6842806.

[17] S. K. Gurumurthy and A. Monti. “Converter-Based Dynamics and Control of Modern Power Systems”. In: Academic Press, 2020. Chap. 11 - Dynamic Voltage Stability, p. 305. DOI: https://doi.org/10.1016/C2018-0-02717-6.

[18] E. Ebrahimzadeh et al. “Efficient approach for harmonic resonance identification of large wind power plants”. In: *2016 IEEE 7th International Symposium on Power Electronics for Distributed Generation Systems (PEDG)*. IEEE. 2016, pp. 1–7. DOI: 10.1109/PEDG.2016.7527043.

[19] J. Lyu et al. “Sub-synchronous oscillation mechanism and its suppression in MMC-based HVDC connected wind farms”. In: *IET Generation, Transmission & Distribution* 12.4 (2018), pp. 1021–1029. DOI: https://doi.org/10.1049/iet-gtd.2017.1066.

[20] J. Wachter, L. Gröll, and V. Hagenmeyer. “Survey of real-world grid incidents–opportunities, arising challenges and lessons learned for the future converter dominated power system”. In: *IEEE Open Journal of Power Electronics* (2023). DOI: 10.1109/OJPEL.2023.3343167.

[21] X. Wang and F. Blaabjerg. “Harmonic stability in power electronic-based power systems: Concept, modeling, and analysis”. In: *IEEE Transactions on Smart Grid* 10.3 (2018), pp. 2858–2870. DOI: 10.1109/TSG.2018.2812712.

[22] M. Benhabib, J. Myrzik, and J. Duarte. “Harmonic effects caused by large scale PV installations in LV network”. In: *2007 9th International Conference on Electrical Power Quality and Utilisation*. IEEE. 2007, pp. 1–6. DOI: 10.1109/EPQU.2007.4424134.

[23] C. Li. “Unstable operation of photovoltaic inverter from field experiences”. In: *IEEE Transactions on Power Delivery* 33.2 (2017), pp. 1013–1015. DOI: 10.1109/TPWRD.2017.2656020.

[24] H. Liu, X. Xie, and W. Liu. “An oscillatory stability criterion based on the unified *dq*-frame impedance network model for power systems with high-penetration renewables”. In: *IEEE Transactions on Power Systems* 33.3 (2018), pp. 3472–3485. DOI: 10.1109/TPWRS.2018.2794067.

[25] S. K. Gurumurthy et al. “Hybrid dynamic phasor modeling approaches for accurate closed-loop simulation of power converters”. In: *IEEE Access* 10 (2022), pp. 101643–101655. DOI: 10.1109/ACCESS.2022.3208963.

[26] C. Buchhagen et al. “BorWin1-First Experiences with harmonic interactions in converter dominated grids”. In: *International ETG Congress 2015; Die Energiewende-Blueprints for the new energy age*. VDE. 2015, pp. 1–7.

[27] J. H. Enslin and P. J. Heskes. “Harmonic interaction between a large number of distributed power inverters and the distribution network”. In: *IEEE transactions on power electronics* 19.6 (2004), pp. 1586–1593. DOI: 10.1109/TPEL.2004.836615.

[28] A. Riccobono, M. Mirz, and A. Monti. “Noninvasive online parametric identification of three-phase AC power impedances to assess the stability of grid-tied power electronic inverters in LV networks”. In: *IEEE Journal of Emerging and Selected Topics in Power Electronics* 6.2 (2017), pp. 629–647. DOI: 10.1109/JESTPE.2017.2783042.

[29] T. T. Tran et al. “Enhancing Performance of Andronov-Hopf Oscillator-Based Grid-Forming Converters in Microgrids With Non-Invasive Online Impedance Estimation”. In: *IEEE Transactions on Smart Grid* 14.6 (2023), pp. 4479–4493. DOI: 10.1109/TSG.2023.3260721.

[30] T. Roinila, M. Vilkko, and J. Sun. “Broadband methods for online grid impedance measurement”. In: *2013 IEEE Energy Conversion Congress and Exposition*. IEEE. 2013, pp. 3003–3010. DOI: 10.1109/ECCE.2013.6647093.

[31] T. Roinila and T. Messo. “Online grid-impedance measurement using ternary-sequence injection”. In: *IEEE Transactions on Industry Applications* 54.5 (2018), pp. 5097–5103. DOI: 10.1109/TIA.2018.2825938.

[32] A. Monti et al. “Vorrichtung zur Bestimmung der Impedanz in Abhängigkeit der Frequenz eines zu messenden Versorgungsnetzes”. DE102019214533A1. Mar. 2021. URL: https://worldwide.espacenet.com/patent/search/family/072665242/publication/DE102019214533A1?q=pn%3DDE102019214533A1.

[33] S. K. Gurumurthy et al. “Non-Invasive Wideband-frequency Grid Impedance Measurement Device”. In: *2019 IEEE 10th International Workshop on Applied Measurements for Power Systems (AMPS)*. IEEE. 2019, pp. 1–6. DOI: 10.1109/AMPS.2019.8897787.

[34] F. Cecati et al. “LTP Modeling and Analysis of Frequency Coupling in PLL-Synchronized Converters for Harmonic Power Flow Studies”. In: *IEEE Transactions on Smart Grid* (2022). DOI: 10.1109/TSG.2022.3228616.

[35] S. Zhu et al. “Stability assessment of modular multilevel converters based on linear time-periodic theory: Time-domain vs. frequency-domain”. In: *IEEE Transactions on Power Delivery* 37.5 (2022), pp. 3980–3995. DOI: 10.1109/TPWRD.2022.3142751.

[36] J. Lyu et al. “Harmonic state-space based small-signal impedance modeling of a modular multilevel converter with consideration of internal harmonic dynamics”. In: *IEEE Transactions on Power Electronics* 34.3 (2018), pp. 2134–2148. DOI: 10.1109/TPEL.2018.2842682.

[37] P. Lehn and K. Lian. “Frequency coupling matrix of a voltage-source converter derived from piecewise linear differential equations”. In: *IEEE Transactions on Power Delivery* 22.3 (2007), pp. 1603–1612. DOI: 10.1109/TPWRD.2006.886779.

[38] D. Gallo et al. “A new test procedure to measure power electronic devices frequency coupling admittance”. In: *IEEE Transactions on Instrumentation and Measurement* 67.10 (2018), pp. 2401–2409. DOI: 10.1109/TIM.2018.2819318.

[39] F. Yahyaie and P. W. Lehn. “Using frequency coupling matrix techniques for the analysis of harmonic interactions”. In: *IEEE Transactions on Power Delivery* 31.1 (2015), pp. 112–121. DOI: 10.1109/TPWRD.2015.2442573.

[40] J. Yadav et al. “Frequency Coupling Matrix Model of a Three-Phase Variable Frequency Drive”. In: *IEEE Transactions on Industry Applications* 58.3 (2022), pp. 3652–3663. DOI: 10.1109/TIA.2022.3156104.

[41] A. Lesage-Landry, S. Chen, and J. A. Taylor. "Estimating the frequency coupling matrix from network measurements". In: *IEEE Transactions on Control of Network Systems* 7.2 (2019), pp. 724–733. DOI: 10.1109/TCNS.2019.2940265.

[42] J. Sun. "Impedance-based stability criterion for grid-connected inverters". In: *IEEE transactions on power electronics* 26.11 (2011), pp. 3075–3078. DOI: 10.1109/TPEL.2011.2136439.

[43] J. Sun et al. "A theory for harmonics created by resonance in converter-grid systems". In: *IEEE Transactions on Power Electronics* 34.4 (2018), pp. 3025–3029. DOI: 10.1109/TPEL.2018.2869781.

[44] J. Sun. "Frequency-domain stability criteria for converter-based power systems". In: *IEEE Open Journal of Power Electronics* 3 (2022), pp. 222–254. DOI: 10.1109/OJPEL.2022.3155568.

[45] B. Wen et al. "Inverse Nyquist stability criterion for grid-tied inverters". In: *IEEE Transactions on Power Electronics* 32.2 (2016), pp. 1548–1556. DOI: 10.1109/TPEL.2016.2545871.

[46] W. Cao et al. "D–Q impedance based stability analysis and parameter design of three-phase inverter-based AC power systems". In: *IEEE Transactions on Industrial Electronics* 64.7 (2017), pp. 6017–6028. DOI: 10.1109/TIE.2017.2682027.

[47] D. Yang, X. Ruan, and H. Wu. "Impedance shaping of the grid-connected inverter with LCL filter to improve its adaptability to the weak grid condition". In: *IEEE Transactions on Power Electronics* 29.11 (2014), pp. 5795–5805. DOI: 10.1109/TPEL.2014.2300235.

[48] X. Zong, P. A. Gray, and P. W. Lehn. "New metric recommended for IEEE standard 1547 to limit harmonics injected into distorted grids". In: *IEEE Transactions on Power Delivery* 31.3 (2015), pp. 963–972. DOI: 10.1109/TPWRD.2015.2403278.

[49] M. Céspedes and J. Sun. "Online grid impedance identification for adaptive control of grid-connected inverters". In: *2012 IEEE Energy Conversion Congress and Exposition (ECCE)*. IEEE. 2012, pp. 914–921. DOI: 10.1109/ECCE.2012.6342721.

[50] M. Cespedes and J. Sun. “Impedance shaping of three-phase grid-parallel voltage-source converters”. In: *2012 Twenty-Seventh Annual IEEE Applied Power Electronics Conference and Exposition (APEC)*. IEEE. 2012, pp. 754–760. DOI: 10.1109/APEC.2012.6165904.

[51] S. K. Gurumurthy, M. Cupelli, and A. Monti. “A generalized framework for synthesizing virtual output impedance control of grid integrated power electronic converters”. In: *2018 IEEE International Conference on Power Electronics, Drives and Energy Systems (PEDES)*. IEEE. 2018, pp. 1–6. DOI: 10.1109/PEDES.2018.8707895.

[52] S. K. Gurumurthy and A. Monti. “A Non-Parametric Approach to Harmonic Instability Mitigation for Renewable-Based Power Plants”. In: *2024 IEEE 15th International Symposium on Power Electronics for Distributed Generation Systems (PEDG)*. IEEE. 2024, pp. 1–6. DOI: 10.1109/PEDG61800.2024.10667385.

[53] M. Cupelli et al. “Port controlled Hamiltonian modeling and IDA-PBC control of dual active bridge converters for DC microgrids”. In: *IEEE Transactions on Industrial Electronics* 66.11 (2019), pp. 9065–9075. DOI: 10.1109/TIE.2019.2901645.

[54] J. Zhao et al. “Passivity-oriented design of LCL-type grid-connected inverters with Luenberger observer-based active damping”. In: *IEEE Transactions on Power Electronics* 37.3 (2021), pp. 2625–2635. DOI: 10.1109/TPEL.2021.3109434.

[55] B. Wen et al. “Analysis of DQ small-signal impedance of grid-tied inverters”. In: *IEEE Transactions on Power Electronics* 31.1 (2015), pp. 675–687. DOI: 10.1109/TPEL.2015.2398192.

[56] A. Adib et al. “On stability of voltage source inverters in weak grids”. In: *Ieee Access* 6 (2018), pp. 4427–4439. DOI: 10.1109/ACCESS.2017.2788818.

[57] F. Bignucolo et al. “Impact of distributed generation grid code requirements on islanding detection in LV networks”. In: *Energies* 10.2 (2017), p. 156. DOI: https://doi.org/10.3390/en10020156.

[58] H. Langkowski et al. “Spectral grid impedance identification on different voltage levelsChallenges and realization”. In: *2017 IEEE Power & Energy Society General Meeting*. IEEE. 2017, pp. 1–5. DOI: 10.1109/PESGM.2017.8274683.

[59] M. Jordan et al. “Online network impedance identification with wave-package and inter-harmonic signals”. In: *2015 International School on Nonsinusoidal Currents and Compensation (ISNCC)*. IEEE. 2015, pp. 1–6. DOI: 10.1109/ISNCC.2015.7174700.

[60] T. T. Do et al. “Novel grid impedance measurement setups in electrical power systems”. In: *2016 IEEE International Workshop on Applied Measurements for Power Systems (AMPS)*. IEEE. 2016, pp. 1–6. DOI: 10.1109/AMPS.2016.7602808.

[61] *Impedance measurement kit*. IOZ/VLA2500. Venable Instruments. URL: https://www.venableinstruments.com/accessories/input-output-impedance-measurement.

[62] J. Liu et al. “Impedance measurement of three-phase inverter in the stationary frame using frequency response analyzer”. In: *IEEE Transactions on Power Electronics* 35.9 (2020), pp. 9390–9401. DOI: 10.1109/TPEL.2020.2974805.

[63] M. Bienholz and G. Griepentrog. “Wide-band impedance measurement for converter impedance determination in lv-grids”. In: *2018 20th European Conference on Power Electronics and Applications (EPE’18 ECCE Europe)*. IEEE. 2018, P–1.

[64] M. Cespedes and J. Sun. “Three-phase impedance measurement for system stability analysis”. In: *2013 IEEE 14th Workshop on Control and Modeling for Power Electronics (COMPEL)*. IEEE. 2013, pp. 1–6. DOI: 10.1109/COMPEL.2013.6626404.

[65] T. Roinila, T. Messo, and E. Santi. “MIMO-identification techniques for rapid impedance-based stability assessment of three-phase systems in DQ domain”. In: *IEEE Transactions on Power Electronics* 33.5 (2017), pp. 4015–4022. DOI: 10.1109/TPEL.2017.2714581.

[66] E. Levy. “Complex-curve fitting”. In: *IRE transactions on automatic control* 1 (1959), pp. 37–43. DOI: 10.1109/TAC.1959.6429401.

[67] E. S. Bañuelos-Cabral, J. A. Gutiérrez-Robles, and B. Gustavsen. "Rational fitting techniques for the modeling of electric power components and systems using MATLAB environment". In: *Rational Fitting Techniques for the Modeling of Electric Power Components and Systems Using MATLAB Environment*. IntechOpen, 2017. DOI: 10.5772/intechopen.71358.

[68] A. Rygg et al. "A modified sequence-domain impedance definition and its equivalence to the dq-domain impedance definition for the stability analysis of AC power electronic systems". In: *IEEE Journal of Emerging and Selected Topics in Power Electronics* 4.4 (2016), pp. 1383–1396. DOI: 10.1109/JESTPE.2016.2588733.

[69] A. Rygg et al. "On the equivalence and impact on stability of impedance modeling of power electronic converters in different domains". In: *IEEE Journal of Emerging and Selected Topics in Power Electronics* 5.4 (2017), pp. 1444–1454. DOI: 10.1109/JESTPE.2017.2744988.

[70] B. Wen and P. Mattavelli. "Harmonic current analysis of the active front end system in the presence of grid voltage disturbance". In: *2018 IEEE applied power electronics conference and exposition (APEC)*. IEEE. 2018, pp. 499–504. DOI: 10.1109/APEC.2018.8341058.

[71] M. Mirz et al. "Measurement-based parameter identification of non-linear polynomial frequency domain model of single-phase four diode bridge rectifier". In: *2017 IEEE International Instrumentation and Measurement Technology Conference (I2MTC)*. IEEE, 2017, pp. 1–6. DOI: 10.1109/I2MTC.2017.7969758.

[72] R. Storn and K. Price. "Differential evolution–a simple and efficient heuristic for global optimization over continuous spaces". In: *Journal of global optimization* 11 (1997), pp. 341–359.

[73] R. N. Beres et al. "Optimal design of high-order passive-damped filters for grid-connected applications". In: *IEEE Transactions on Power Electronics* 31.3 (2015), pp. 2083–2098. DOI: 10.1109/TPEL.2015.2441299.

[74] M. Amin and M. Molinas. “Small-signal stability assessment of power electronics based power systems: A discussion of impedance-and eigenvalue-based methods”. In: *IEEE Transactions on Industry Applications* 53.5 (2017), pp. 5014–5030. DOI: 10.1109/TIA.2017.2712692.

[75] S. Jiang and G. Konstantinou. “Impedance-based stability analysis: Nodal admittance or bus admittance?” In: *IEEE Transactions on Power Systems* (2023). DOI: 10.1109/TPWRS.2023.3267504.

[76] M. K. Bakhshizadeh et al. “Improving the impedance-based stability criterion by using the vector fitting method”. In: *IEEE Transactions on Energy Conversion* 33.4 (2018), pp. 1739–1747. DOI: 10.1109/TEC.2018.2849347.

[77] N. Cifuentes et al. “Black-box impedance-based stability assessment of dynamic interactions between converters and grid”. In: *IEEE Transactions on Power Systems* 37.4 (2021), pp. 2976–2987. DOI: 10.1109/TPWRS.2021.3128812.

[78] M. Nahalparvari et al. “DC-side impedance estimation of a modular multilevel converter through system identification of a partially black-boxed control system”. In: *IEEE Transactions on Energy Conversion* 37.4 (2022), pp. 2708–2721. DOI: 10.1109/TEC.2022.3175802.

[79] R. D. Middlebrook and S. Cuk. “A general unified approach to modelling switching-converter power stages”. In: *1976 IEEE power electronics specialists conference*. IEEE. 1976, pp. 18–34. DOI: 10.1109/PESC.1976.7072895.

[80] A. Riccobono and E. Santi. “Comprehensive review of stability criteria for DC power distribution systems”. In: *IEEE Transactions on Industry Applications* 50.5 (2014), pp. 3525–3535. DOI: 10.1109/ECCE.2012.6342299.

[81] Y. Liao and X. Wang. “Impedance-based stability analysis for interconnected converter systems with open-loop RHP poles”. In: *IEEE Transactions on Power Electronics* 35.4 (2019), pp. 4388–4397. DOI: 10.1109/TPEL.2019.2939636.

[82] S. McKinley and M. Levine. “Cubic spline interpolation”. In: *College of the Redwoods* 45.1 (1998), pp. 1049–1060.

[83] A. Aapro et al. “Effect of active damping on output impedance of three-phase grid-connected converter”. In: *IEEE Transactions on Industrial Electronics* 64.9 (2017), pp. 7532–7541. DOI: 10.1109/TIE.2017.2696494.

[84] C. P. Dick et al. “Active damping of LCL resonance with minimum sensor effort by means of a digital infinite impulse response filter”. In: *2007 European Conference on Power Electronics and Applications*. IEEE. 2007, pp. 1–8. DOI: 10.1109/EPE.2007.4417362.

[85] M. Liserre, A. Dell’Aquila, and F. Blaabjerg. “Genetic algorithm-based design of the active damping for an LCL-filter three-phase active rectifier”. In: *IEEE Transactions on Power Electronics* 19.1 (2004), pp. 76–86. DOI: 10.1109/APEC.2003.1179221.

[86] X. Wang et al. “An active damper for stabilizing power-electronics-based AC systems”. In: *IEEE Transactions on Power Electronics* 29.7 (2013), pp. 3318–3329. DOI: 10.1109/TPEL.2013.2278716.

[87] X. Wang, F. Blaabjerg, and P. C. Loh. “Grid-current-feedback active damping for LCL resonance in grid-connected voltage-source converters”. In: *IEEE Transactions on Power Electronics* 31.1 (2015), pp. 213–223. DOI: 10.1109/TPEL.2015.2411851.

[88] J. Wang et al. “Delay-dependent stability of single-loop controlled grid-connected inverters with LCL filters”. In: *IEEE Transactions on Power Electronics* 31.1 (2015), pp. 743–757. DOI: 10.1109/TPEL.2015.2401612.

E.ON ERC Band 1
Streblow, R.
Thermal Sensation and Comfort Model for Inhomogeneous Indoor Environments
1. Auflage 2011
ISBN 978-3-942789-00-4

E.ON ERC Band 2
Naderi, A.
Multi-phase, multi-species reactive transport modeling as a tool for system analysis in geological carbon dioxide storage
1. Auflage 2011
ISBN 978-3-942789-01-1

E.ON ERC Band 3
Westner, G.
Four Essays related to Energy Economic Aspects of Combined Heat and Power Generation
1. Auflage 2012
ISBN 978-3-942789-02-8

E.ON ERC Band 4
Lohwasser, R.
Impact of Carbon Capture and Storage (CCS) on the European Electricity Market
1. Auflage 2012
ISBN 978-3-942789-03-5

E.ON ERC Band 5
Dick, C.
Multi-Resonant Converters as Photovoltaic Module-Integrated Maximum Power Point Tracker
1. Auflage 2012
ISBN 978-3-942789-04-2

E.ON ERC Band 6
Lenke, R.
A Contribution to the Design of Isolated DC-DC Converters for Utility Applications
1. Auflage 2012
ISBN 978-3-942789-05-9

E.ON ERC Band 7
Brännström, F.
Einsatz hybrider RANS-LES-Turbulenzmodelle in der Fahrzeugklimatisierung
1. Auflage 2012
ISBN 978-3-942789-06-6

E.ON ERC Band 8
Bragard, M.
The Integrated Emitter Turn-Off Thyristor - An Innovative MOS-Gated High-Power Device
1. Auflage 2012
ISBN 978-3-942789-07-3

E.ON ERC Band 9
Hoh, A.
Exergiebasierte Bewertung gebäudetechnischer Anlagen
1. Auflage 2013
ISBN 978-3-942789-08-0

E.ON ERC Band 10
Köllensperger, P.
The Internally Commutated Thyristor - Concept, Design and Application
1. Auflage 2013
ISBN 978-3-942789-09-7

E.ON ERC Band 11
Achtnicht, M.
Essays on Consumer Choices Relevant to Climate Change: Stated Preference Evidence from Germany
1. Auflage 2013
ISBN 978-3-942789-10-3

E.ON ERC Band 12
Panašková, J.
Olfaktorische Bewertung von Emissionen aus Bauprodukten
1. Auflage 2013
ISBN 978-3-942789-11-0

E.ON ERC Band 13
Vogt, C.
Optimization of Geothermal Energy Reservoir Modeling using Advanced Numerical Tools for Stochastic Parameter Estimation and Quantifying Uncertainties
1. Auflage 2013
ISBN 978-3-942789-12-7

E.ON ERC Band 14
Benigni, A.
Latency exploitation for parallelization of power systems simulation
1. Auflage 2013
ISBN 978-3-942789-13-4

E.ON ERC Band 15
Butschen, T.
Dual-ICT – A Clever Way to Unite Conduction and Switching Optimized Properties in a Single Wafer
1. Auflage 2013
ISBN 978-3-942789-14-1

E.ON ERC Band 16
Li, W.
Fault Detection and Protection inMedium Voltage DC Shipboard Power Systems
1. Auflage 2013
ISBN 978-3-942789-15-8

E.ON ERC Band 17
Shen, J.
Modeling Methodologies for Analysis and Synthesis of Controls and Modulation Schemes for High-Power Converters with Low Pulse Ratios
1. Auflage 2014
ISBN 978-3-942789-16-5

E.ON ERC Band 18
Flieger, B.
Innenraummodellierung einer Fahrzeugkabine in der Programmiersprache Modelica
1. Auflage 2014
ISBN 978-3-942789-17-2

E.ON ERC Band 19
Liu, J.
Measurement System and Technique for Future Active Distribution Grids
1. Auflage 2014
ISBN 978-3-942789-18-9

E.ON ERC Band 20
Kandzia, C.
Experimentelle Untersuchung der Strömungsstrukturen in einer Mischlüftung
1. Auflage 2014
ISBN 978-3-942789-19-6

E.ON ERC Band 21
Thomas, S.
A Medium-Voltage Multi-Level DC/DC Converter with High Voltage Transformation Ratio
1. Auflage 2014
ISBN 978-3-942789-20-2

E.ON ERC Band 22
Tang, J.
Probabilistic Analysis and Stability Assessment for Power Systems with Integration of Wind Generation and Synchrophasor Measurement
1. Auflage 2014
ISBN 978-3-942789-21-9

E.ON ERC Band 23
Sorda, G.
The Diffusion of Selected Renewable Energy Technologies: Modeling, Economic Impacts, and Policy Implications
1. Auflage 2014
ISBN 978-3-942789-22-6

E.ON ERC Band 24
Rosen, C.
Design considerations and functional analysis of local reserve energy markets for distributed generation
1. Auflage 2014
ISBN 978-3-942789-23-3

E.ON ERC Band 25
Ni, F.
Applications of Arbitrary Polynomial Chaos in Electrical Systems
1. Auflage 2015
ISBN 978-3-942789-24-0

E.ON ERC Band 26
Michelsen, C. C.
The *Energiewende* in the German Residential Sector: Empirical Essays on Homeowners' Choices of Space Heating Technologies
1. Auflage 2015
ISBN 978-3-942789-25-7

E.ON ERC Band 27
Rohlfs, W.
Decision-Making under Multi-Dimensional Price Uncertainty for Long-Lived Energy Investments
1. Auflage 2015
ISBN 978-3-942789-26-4

E.ON ERC Band 28
Wang, J.
Design of Novel Control algorithms of Power Converters for Distributed Generation
1. Auflage 2015
ISBN 978-3-942789-27-1

E.ON ERC Band 29
Helmedag, A.
System-Level Multi-Physics Power Hardware in the Loop Testing for Wind Energy Converters
1. Auflage 2015
ISBN 978-3-942789-28-8

E.ON ERC Band 30
Togawa, K.
Stochastics-based Methods Enabling Testing of Grid-related Algorithms through Simulation
1. Auflage 2015
ISBN 978-3-942789-29-5

E.ON ERC Band 31
Huchtemann, K.
Supply Temperature Control Concepts in Heat Pump Heating Systems
1. Auflage 2015
ISBN 978-3-942789-30-1

E.ON ERC Band 32
Molitor, C.
Residential City Districts as Flexibility Resource: Analysis, Simulation, and Decentralized Coordination Algorithms
1. Auflage 2015
ISBN 978-3-942789-31-8

E.ON ERC Band 33
Sunak, Y.
Spatial Perspectives on the Economics of Renewable Energy Technologies
1. Auflage 2015
ISBN 978-3-942789-32-5

E.ON ERC Band 34
Cupelli, M.
Advanced Control Methods for Robust Stability of MVDC Systems
1. Auflage 2015
ISBN 978-3-942789-33-2

E.ON ERC Band 35
Chen, K.
Active Thermal Management for Residential Air Source Heat Pump Systems
1. Auflage 2015
ISBN 978-3-942789-34-9

E.ON ERC Band 36
Pâques, G.
Development of SiC GTO Thyristors with Etched Junction Termination
1. Auflage 2016
ISBN 978-3-942789-35-6

E.ON ERC Band 37
Garnier, E.
Distributed Energy Resources and Virtual Power Plants: Economics of Investment and Operation
1. Auflage 2016
ISBN 978-3-942789-37-0

E.ON ERC Band 38
Calì, D.
Occupants' Behavior and its Impact upon the Energy Performance of Buildings
1. Auflage 2016
ISBN 978-3-942789-36-3

E.ON ERC Band 39
Isermann, T.
A Multi-Agent-based Component Control and Energy Management System for Electric Vehicles
1. Auflage 2016
ISBN 978-3-942789-38-7

E.ON ERC Band 40
Wu, X.
New Approaches to Dynamic Equivalent of Active Distribution Network for Transient Analysis
1. Auflage 2016
ISBN 978-3-942789-39-4

E.ON ERC Band 41
Garbuzova-Schiftler, M.
The Growing ESCO Market for Energy Efficiency in Russia: A Business and Risk Analysis
1. Auflage 2016
ISBN 978-3-942789-40-0

E.ON ERC Band 42
Huber, M.
Agentenbasierte Gebäudeautomation für raumlufttechnische Anlagen
1. Auflage 2016
ISBN 978-3-942789-41-7

E.ON ERC Band 43
Soltau, N.
High-Power Medium-Voltage DC-DC Converters: Design, Control and Demonstration
1. Auflage 2017
ISBN 978-3-942789-42-4

E.ON ERC Band 44
Stieneker, M.
Analysis of Medium-Voltage Direct-Current Collector Grids in Offshore Wind Parks
1. Auflage 2017
ISBN 978-3-942789-43-1

E.ON ERC Band 45
Bader, A.
Entwicklung eines Verfahrens zur Strompreisvorhersage im kurzfristigen Intraday-Handelszeitraum
1. Auflage 2017
ISBN 978-3-942789-44-8

E.ON ERC Band 46
Chen, T.
Upscaling Permeability for Fractured Porous Rocks and Modeling Anisotropic Flow and Heat Transport
1. Auflage 2017
ISBN 978-3-942789-45-5

E.ON ERC Band 47
Ferdowsi, M.
Data-Driven Approaches for Monitoring of Distribution Grids
1. Auflage 2017
ISBN 978-3-942789-46-2

E.ON ERC Band 48
Kopmann, N.
Betriebsverhalten freier Heizflächen unter zeitlich variablen Randbedingungen
1. Auflage 2017
ISBN 978-3-942789-47-9

E.ON ERC Band 49
Fütterer, J.
Tuning of PID Controllers within Building Energy Systems
1. Auflage 2017
ISBN 978-3-942789-48-6

E.ON ERC Band 50
Adler, F.
A Digital Hardware Platform for Distributed Real-Time Simulation of Power Electronic Systems
1. Auflage 2017
ISBN 978-3-942789-49-3

E.ON ERC Band 51
Harb, H.
Predictive Demand Side Management Strategies for Residential Building Energy Systems
1. Auflage 2017
ISBN 978-3-942789-50-9

E.ON ERC Band 52
Jahangiri, P.
Applications of Paraffin-Water Dispersions in Energy Distribution Systems
1. Auflage 2017
ISBN 978-3-942789-51-6

E.ON ERC Band 53
Adolph, M.
Identification of Characteristic User Behavior with a Simple User Interface in the Context of Space Heating
1. Auflage 2018
ISBN 978-3-942789-52-3

E.ON ERC Band 54
Galassi, V.
Experimental evidence of private energy consumer and prosumer preferences in the sustainable energy transition
1. Auflage 2017
ISBN 978-3-942789-53-0

E.ON ERC Band 55
Sangi, R.
Development of Exergy-based Control Strategies for Building Energy Systems
1. Auflage 2018
ISBN 978-3-942789-54-7

E.ON ERC Band 56
Stinner, S.
Quantifying and Aggregating the Flexibility of Building Energy Systems
1. Auflage 2018
ISBN 978-3-942789-55-4

E.ON ERC Band 57
Fuchs, M.
Graph Framework for Automated Urban Energy System Modeling
1. Auflage 2018
ISBN 978-3-942789-56-1

E.ON ERC Band 58
Osterhage, T.
Messdatengestützte Analyse und Interpretation sanierungsbedingter Effizienzsteigerungen im Wohnungsbau
1. Auflage 2018
ISBN 978-3-942789-57-8

E.ON ERC Band 59
Frieling, J.
Quantifying the Role of Energy in Aggregate Production Functions for Industrialized Countries
1. Auflage 2018
ISBN 978-3-942789-58-5

E.ON ERC Band 60
Lauster, M.
Parametrierbare Gebäudemodelle für dynamische Energiebedarfsrechnungen von Stadtquartieren
1. Auflage 2018
ISBN 978-3-942789-59-2

E.ON ERC Band 61
Zhu, L.
Modeling, Control and Hardware in the Loop in Medium Voltage DC Shipboard Power Systems
1. Auflage 2018
ISBN 978-3-942789-60-8

E.ON ERC Band 62
Feron, B.
An optimality assessment methodology for Home Energy Management System approaches based on uncertainty analysis
1. Auflage 2018
ISBN 978-3-942789-61-5

E.ON ERC Band 63
Diekerhof, M.
Distributed Optimization for the Exploitation of Multi-Energy Flexibility under Uncertainty in City Districts
1. Auflage 2018
ISBN 978-3-942789-62-2

E.ON ERC Band 64
Wolisz, H.
Transient Thermal Comfort Constraints for Model Predictive Heating Control
1. Auflage 2018
ISBN 978-3-942789-63-9

E.ON ERC Band 65
Pickartz, S.
Virtualization as an Enabler for Dynamic Resource Allocation in HPC
1. Auflage 2019
ISBN 978-3-942789-64-6

E.ON ERC Band 66
Khayyamim, S.
Centralized-decentralized Energy Management in Railway System
1. Auflage 2019
ISBN 978-3-942789-65-3

E.ON ERC Band 67
Schlösser, T.
Methodology for Holistic Evaluation of Building Energy Systems under Dynamic Boundary Conditions
1. Auflage 2019
ISBN 978-3-942789-66-0

E.ON ERC Band 68
Cui, S.
Modular Multilevel DC-DC Converters Interconnecting High-Voltage and Medium-Voltage DC Grids
1. Auflage 2019
ISBN 978-3-942789-67-7

E.ON ERC Band 69
Hu, J.
Modulation and Dynamic Control of Intelligent Dual-Active-Bridge Converter Based Substations for Flexible DC Grids
1. Auflage 2019
ISBN 978-3-942789-68-4

E.ON ERC Band 70
Schiefelbein, J.
Optimized Placement of Thermo-Electric Energy Systems in City Districts under Uncertainty
1. Auflage 2019
ISBN 978-3-942789-69-1

E.ON ERC Band 71
Ferdinand, R.
Grid Operation of HVDC-Connected Offshore Wind Farms: Power Quality and Switching Strategies
1. Auflage 2019
ISBN 978-3-942789-70-7

E.ON ERC Band 72
Musa, A.
Advanced Control Strategies for Stability Enhancement of Future Hybrid AC/DC Networks
1. Auflage 2019
ISBN 978-3-942789-71-4

E.ON ERC Band 73
Angioni, A.
Uncertainty modeling for analysis and design of monitoring systems for dynamic electrical distribution grids
1. Auflage 2019
ISBN 978-3-942789-72-1

E.ON ERC Band 74
Möhlenkamp, M.
Thermischer Komfort bei Quellluftströmungen
1. Auflage 2019
ISBN 978-3-942789-73-8

E.ON ERC Band 75
Voss, J.
Multi-Megawatt Three-Phase Dual-Active Bridge DC-DC Converter
1. Auflage 2019
ISBN 978-3-942789-74-5

E.ON ERC Band 76
Siddique, H.
The Three-Phase Dual-Active Bridge Converter Family: Modeling, Analysis, Optimization and Comparison of Two-Level and Three-Level Converter Variants
1. Auflage 2019
ISBN 978-3-942789-75-2

E.ON ERC Band 77
Heesen, F.
An Interdisciplinary Analysis of Heat Energy Consumption in Energy-Efficient Homes: Essays on Economic, Technical and Behavioral Aspects
1. Auflage 2019
ISBN 978-3-942789-76-9

E.ON ERC Band 78
Möller, R.
Untersuchung der Durchschlagspannung von Mineral-, Silikonölen und synthetischen Estern bei mittelfrequenten Spannungen
1. Auflage 2020
ISBN 978-3-942789-77-6

E.ON ERC Band 79
Höfer, T.
Transition Towards a Renewable Energy Infrastructure: Spatial Interdependencies and Stake-holder Preferences
1. Auflage 2020
ISBN 978-3-942789-78-3

E.ON ERC Band 80
Freitag, H.
Investigation of the Internal Flow Behavior in Active Chilled Beams
1. Auflage 2020
ISBN 978-3-942789-79-0

E.ON ERC Band 81
Razik, L.
High-Performance Computing Methods in Large-Scale Power System Simulation
1. Auflage 2020
ISBN 978-3-942789-80-6

E.ON ERC Band 82
Mirz, M.
A Dynamic Phasor Real-Time Simulation Based Digital Twin for Power Systems
1. Auflage 2020
ISBN 978-3-942789-81-3

E.ON ERC Band 83
Schmitz, H.
Energy Consumption Behavior of Private Households: Heterogeneity, Prosuming, and Rebound
1. Auflage 2020
ISBN 978-3-942789-82-0

E.ON ERC Band 84
Cupelli, L.
Data-driven Methods for Voltage Control in Distribution Networks: A Bottom-Up Approach
1. Auflage 2020
ISBN 978-3-942789-83-7

E.ON ERC Band 85
Happ, S.
A Scalable Simulation Method for Cyber-Physical Power Systems
1. Auflage 2020
ISBN 978-3-942789-84-4

E.ON ERC Band 86
Rewitz, K.
Modellierung des thermischen Komforts in Kabinen-innenräumen
1. Auflage 2021
ISBN 978-3-948234-00-3

E.ON ERC Band 87
Wesseling, M.
Probabilistische Bewertung von Entrauchungsanlagen
1. Auflage 2021
ISBN 978-3-948234-01-0

E.ON ERC Band 88
Stoyanova, I.
Cooperative Energy Management and Cross-Domain Optimization for Electro-Thermal Devices at City-District and City-Level
1. Auflage 2021
ISBN 978-3-948234-02-7

E.ON ERC Band 89
Tran, T.
Advanced hierarchical control structure for Virtual Oscillator-based distributed generation in multi-bus microgrids under different grid dynamics and disturbances
1. Auflage 2021
ISBN 978-3-948234-03-4

E.ON ERC Band 90
Yang, Z.
On the Stability of Three-Phase Grid-Tied Photovoltaic Inverter Systems
1. Auflage 2021
ISBN 978-3-948234-04-1

E.ON ERC Band 91
Wang, T.
Fault Detection and Isolation in DC Distribution Grids
1. Auflage 2021
ISBN 978-3-948234-05-8

E.ON ERC Band 92
Beushausen, S.
A GaN-Based Switched-Mode Gate-Drive Unit for Medium-Voltage IGBTs
1. Auflage 2021
ISBN 978-3-948234-06-5

E.ON ERC Band 93
Schumacher, M.
Design and Assessment of Grid-driven Distributed Cogeneration
1. Auflage 2021
ISBN 978-3-948234-07-2

E.ON ERC Band 94
Joebges, P.
Distributed Real-Time Simulation of Modular Bidirectional DC-DC Converters for Control-Hardware-in-the-Loop
1. Auflage 2021
ISBN 978-3-948234-08-9

E.ON ERC Band 95
Averous, R.
Analysis of the Application of a Grid Emulator to Conduct Grid Compliance Tests for Multi-Megawatt Wind Turbines A Contribution towards Ground Testing of Wind Turbines
1. Auflage 2021
ISBN 978-3-948234-09-6

E.ON ERC Band 96
Virdag, A.
Design, Implementation and Analysis of DC Circuit-breaker for Low-Voltage DC Grids with Counter-current Injection Principle
1. Auflage 2021
ISBN 978-3-948234-10-2

E.ON ERC Band 97
Dähling, S.
Cloud-based Multi-Agent Systems for Flexibility Management in Future Distribution Grids
1. Auflage 2021
ISBN 978-3-948234-11-9

E.ON ERC Band 98
Qawasmi, A.
Fault Current Interruption Analysis and Development of a Power Semiconductor Switch for a Medium-Voltage DC Hybrid Circuit Breaker
1. Auflage 2021
ISBN 978-3-948234-12-6

E.ON ERC Band 99
Nolting, L.
Die Versorgungssicherheit mit Elektrizität im Kontext von Liberalisierung und Energiewende
1. Auflage 2021
ISBN 978-3-948234-13-3

E.ON ERC Band 100
Mathis, P.
Heat Transfer Enhancement in Natural Convective Channel Flows by Vortex Streets
1. Auflage 2022
ISBN 978-3-948234-14-0

E.ON ERC Band 101
Wolff, S.
Stated Preferences Concerning Private Passenger and Light-Duty Electric Vehicles in Germany
1. Auflage 2022
ISBN 978-3-948234-15-7

E.ON ERC Band 102
Hackbarth, A.
Private Households' Preferences for Alternative Fuel Vehicles in Germany – An Empirically Founded Analysis of Adoption Decisions, Willingness-to-Pay, and Policy Scenarios
1. Auflage 2022
ISBN 978-3-948234-16-4

E.ON ERC Band 103
Ge, L.
Performance Enhancement of Switched Reluctance Machines for High-speed Backup Generators: Design, Measurement and Control
1. Auflage 2022
ISBN 978-3-948234-17-1

E.ON ERC Band 104
Atasoy, T.
Strategic and Behavioral Responses of Consumers and Producers to Energy and Environmental Policies
1. Auflage 2022
ISBN 978-3-948234-18-8

E.ON ERC Band 105
Remmen, P.
Automated Calibration of Non-Residential Urban Building Energy Modeling
1. Auflage 2022
ISBN 978-3-948234-19-5

E.ON ERC Band 106
Schild, T.
Systematische Entwicklung strukturierter Steuerungs-algorithmen für die Gebäude- und Anlagentechnik
1. Auflage 2022
ISBN 978-3-948234-20-1

E.ON ERC Band 107
Sidik, Y.
Modeling, Control, and Dynamic Stability Analysis of Two-Stage DC Collector Grids in Offshore Wind Park Clusters
1. Auflage 2022
ISBN 978-3-948234-21-8

E.ON ERC Band 108
Sadu, A.
Towards resilient design of distribution grid automation system: An evaluation of its reliability against random failures and susceptibility to targeted attacks
1. Auflage 2022
ISBN 978-3-948234-22-5

E.ON ERC Band 109
Hinz, A.
Electrical Propulsion Systems for Civil Transportation Aircraft
1. Auflage 2022
ISBN 978-3-948234-23-2

E.ON ERC Band 110
Mehrfeld, P.
Evaluation of Heat Pump Systems Under Dynamic Operating Conditions
1. Auflage 2022
ISBN 978-3-948234-24-9

E.ON ERC Band 111
Teichrib, J.
A Hybrid Semiconductor Device for Medium-Voltage DC-DC Converters - The Combination of Thyris-tor and Transistor Technologies
1. Auflage 2022
ISBN 978-3-948234-25-6

E.ON ERC Band 112
Frehn, A.
Under voltage ride through tests on nacelle test benches equipped with a power hardware in the loop setup
1. Auflage 2023
ISBN 978-3-948234-26-3

E.ON ERC Band 113
Bode, G.
Generation of Training Data for Fault Detection and Diagnosis Algorithms Using Fault Simulation and Parameter Uncertainty
1. Auflage 2023
ISBN 978-3-948234-27-0

E.ON ERC Band 114
Vering, C.
Optimale Auslegung von Wärmepumpensystemen für Bestandsgebäude
1. Auflage 2023
ISBN 978-3-948234-28-7

E.ON ERC Band 115
Bogdanović, M.
Towards model partitioning automation of distributed real-time power systems simulations of distribution networks
1. Auflage 2023
ISBN 978-3-948234-29-4

E.ON ERC Band 116
Hering, D.
Optimization of district heating networks using mixed integer quadratically constrained programs
1. Auflage 2023
ISBN 978-3-948234-30-0

E.ON ERC Band 117
De Din, E.
Multi-Timescale Framework for the Voltage Control of Active Distribution Grids
1. Auflage 2023
ISBN 978-3-948234-31-7

E.ON ERC Band 118
Specht, J.
The Energy Supplier 2.0 – Activating Private Households' Flexibility Potential for Value Creation and Services Supply
1. Auflage 2023
ISBN 978-3-948234-32-4

E.ON ERC Band 119
Teichmann, J.
Auswirkungen der Hydraulik auf das Betriebsverhalten von raumlufttechnischen Anlagen
1. Auflage 2023
ISBN 978-3-948234-33-1

E.ON ERC Band 120
Haghgoo, M.
Semantic Interoperability as a Service for the Smart Energy System
1. Auflage 2023
ISBN 978-3-948234-34-8

E.ON ERC Band 121
Roy, G.
Automation Architectures for hybrid ac-dc grid
1. Auflage 2023
ISBN 978-3-948234-35-5

E.ON ERC Band 122
Mork, M.
Model Predictive Control of Building Energy Systems
1. Auflage 2023
ISBN 978-3-948234-36-2

E.ON ERC Band 123
Zargar, B.
Data-Driven Distribution System State Estimation Using Synchrophasor Measurements
1. Auflage 2023
ISBN 978-3-948234-37-9

E.ON ERC Band 124
Rohn, M.
Einseitiges Induktionsverhalten von multiplen Luftstrahlen unterschiedlicher Düsengeometrien
1. Auflage 2024
ISBN 978-3-948234-38-6

E.ON ERC Band 125
Sheykhha, S.
Four essays on the sustainable energy transition: Model-based analyses of regional energy market structures and regulations
1. Auflage 2024
ISBN 978-3-948234-39-3

E.ON ERC Band 126
Warmuz, J.
Current Interruption Capability and Feasibility Assessment for a Medium-Voltage Direct Current Hybrid Circuit Breaker Application
1. Auflage 2024
ISBN 978-3-948234-40-9

E.ON ERC Band 127
Gürses, G.
Machine learning techniques for time series forecasting in power systems operation
1. Auflage 2024
ISBN 978-3-948234-41-6

E.ON ERC Band 128
Baranski, M.
Design of Distributed Model-based Control Agents for Building Automation Systems
1. Auflage 2024
ISBN 978-3-948234-42-3

E.ON ERC Band 129
Karami, M.
Driving Sustainability Through Business Model Innovation in the Energy Industry and Related Sectors
1. Auflage 2024
ISBN 978-3-948234-43-0

E.ON ERC Band 130
Hoffmann, M.
Entwicklung eines Simulationsmodells zur Vorhersage und Optimierung eines Luftwäschers mittels 3-dimensionaler Mehrphasen-Strömungssimulation
1. Auflage 2024
ISBN 978-3-948234-44-7

E.ON ERC Band 131
Stoffel, P.
Learning Strategies for Data-Driven Model Predictive Control of Building Energy Systems
1. Auflage 2024
ISBN 978-3-948234-45-4

E.ON ERC Band 132
Dognini, A.
Multi-criteria service restoration methods for AC and AC/DC distribution grids
1. Auflage 2024
ISBN 978-3-948234-46-1

E.ON ERC Band 133
Schreiner, L.
International Public-Private Strategies in Sustainable Investment and Finance
1. Auflage 2024
ISBN 978-3-948234-47-8

E.ON ERC Band 134
Priesmann, J.
Verteilungseffekte im Kontext der Energiewende: Herausforderungen und regulatorische Lösungsansätze
1. Auflage 2024
ISBN 978-3-948234-48-5

E.ON ERC Band 135
Mortimer, B.
Horizontal Network Coupling for Charging Infrastructure Based on Three-Phase Solid-State Transformers
1. Auflage 2024
ISBN 978-3-948234-49-2

E.ON ERC Band 136
Gümrükcü, E.
A Versatile Strategy for Optimizing Electric Vehicles' Charging Spot Selections in Distribution Grids
1. Auflage 2024
ISBN 978-3-948234-50-8

E.ON ERC Band 137
Pan, Z.
Large Language Model Based Semantic Interoperability Enhancement for Energy Data Management
1. Auflage 2025
ISBN 978-3-948234-51-5

E.ON ERC Band 138
Korompili, A.
Two-Level Control for Multi-Terminal DC Distribution Grids
1. Auflage 2025
ISBN 978-3-948234-52-2

E.ON ERC Band 139
Dinkelbach, J.
Enabling the Real-Time Simulation of Low-Inertia Power Systems by Dynamic Phasor Modelling and Efficient Computing Methods
1. Auflage 2025
ISBN 978-3-948234-53-9

E.ON ERC Band 140
Kümpel, A.
Adaptive agentenbasierte
modellprädiktive Regelung für
Gebäudeenergiesysteme
1. Auflage 2025
ISBN 978-3-948234-54-6

This dissertation addresses the challenges posed by harmonic instability in PEDGs which arise from the increasing integration of RES. Harmonic instability occurs when interactions between power electronic converters generate sustained harmonics and inter-harmonics that distort grid voltage, potentially causing grid destabilization. Monitoring and mitigating harmonic stability is critical for maintaining power quality and stability. Non-parametric models of converters are required as parametric models are often intellectual property.

This work introduces a standalone WFZ device, validated through simulations and experiments, capable of rapid and accurate grid impedance extraction in a non-parametric manner. The capability of the device is further extended to measure the FCM of converters, capturing first order frequency coupling effects. Building on these measurement tools, a novel harmonic stability monitoring method is proposed for multi-bus power networks. This method aggregates locally measured converter impedances on a system-level using a bus admittance matrix approach to identify critical frequencies and corresponding stability margins. Finally, the dissertation develops an advanced VDC that adaptively emulates synthetic damping which mitigates harmonic instability. Experimental validations confirm the damping behaviour and enhancement of system stability margins.

This thesis makes significant contributions in the areas of impedance measurement devices, system-level monitoring of harmonic stability, and the development of an advanced VDC, resulting in advancements in these fields.

ISBN 978-3-948234-55-3

Thinking the Future
Zukunft denken